Binary systems for the determination of high-precision absolute stellar parameters

The Young Massive Detached Binaries catalog

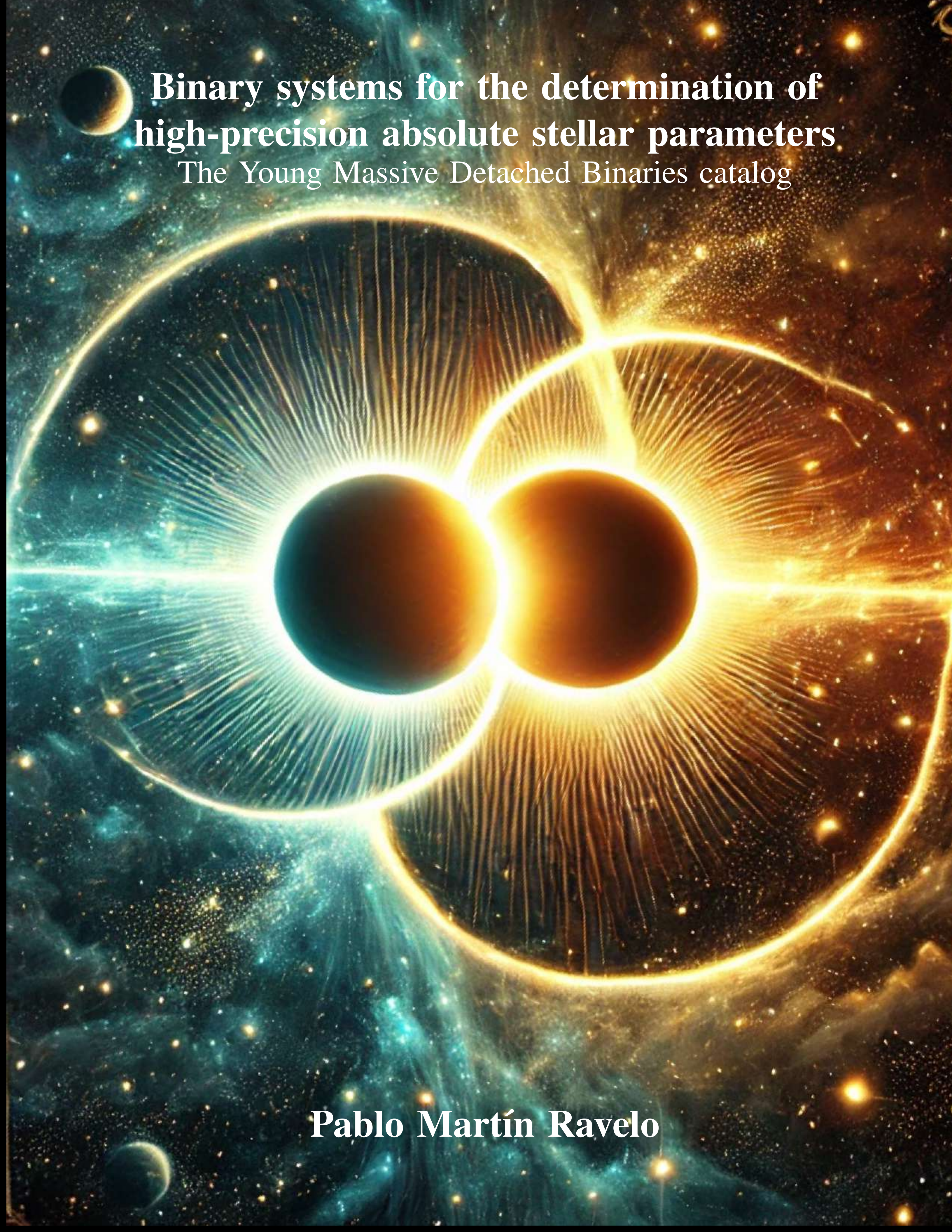

Pablo Martín Ravelo

Binary systems for the determination of high-precision absolute stellar parameters

The Young Massive Detached Binaries catalog

Pablo Martín Ravelo

March 14, 2025

Doctoral Thesis

To fulfill the requirements for the degree of Doctorate in Astronomy
at Universidad de La Serena by

Pablo Martín Ravelo

under the supervision of

Dr. Julia Inés Arias Stampalia, Universidad de La Serena, Chile
Dr. Roberto Gamen, Instituto de Astrofísica de La Plata, Argentina
Dr. Rodolfo Héctor Barbá Suárez, Universidad de La Serena, Chile

Defended on April 4th, 2025 before the committee composed of

Dr. Nidia Irene Morrell, Las Campanas Observatory, Chile
Dr. Jesús Maíz Apellániz, Centro de Astrobiología, CSIC-INTA, España
Dr. José Luis Nilo Castellón, Universidad de La Serena, Chile
Dr. Sebastián Ramírez Alegría, Chile

March 14, 2025

A los que faltan,
a quien estuvo y no está.
Al asiento vacío en la Bombonera,
que nadie podrá llenar.
A las madrugadas condenadas al silencio,
y los mates que quedaron sin tomar...

Abstract

Massive stars play a fundamental role in the chemical and dynamical evolution of galaxies. However, many uncertainties remain regarding their formation, internal structure, and evolutionary pathways. One of the major challenges in understanding massive star evolution is the discrepancy between masses derived from binary dynamics and those predicted by stellar evolution models. Addressing this issue requires highly precise absolute parameter determinations, which detached eclipsing binaries provide by allowing direct, model-independent measurements of stellar masses and radii. This PhD thesis aims to address the former and other key challenges in the field of massive star research by identifying and characterizing young massive eclipsing binaries suitable for precise absolute parameter determinations. A key result of this work is the Young Massive Detached Binary (YMDB) catalog, a resource designed to provide high-quality light curves and spectral classifications for detached systems with spectral types ranging from O9 to B1. By constructing this catalog, this thesis establishes a robust observational framework for confronting theoretical models with empirical data. To construct this catalog, we performed a photometric analysis of 87 young massive stars in detached eclipsing systems using TESS light curves processed through a custom pipeline. This analysis involved determining the amplitude of magnitude variations, orbital periods, times of minima, eccentricities, and the presence of apsidal motion and heartbeat phenomena. A thorough literature review was conducted to obtain MK spectral classifications, and our own spectral classification was performed for 19 systems where previous classifications were unavailable or inconclusive. The analysis identified 20 previously unreported binary systems, with 13 newly recognized as variable stars. Among the 87 stars examined, 30 are confirmed as YMDB members, and 25 are candidates pending spectral classification. The exclusion of the remaining 32 stars is attributed to unsuitable spectral types or their non-detached binary nature. Notable findings include the identification of new light curve classifications, eccentricities in 13 systems, and heartbeat phenomena in several targets. This thesis establishes the foundation for improving our understanding of massive stars by identifying and characterizing high-quality candidates for absolute parameter determination. Through photometric analysis, spectroscopic assessment, and a thorough literature review, the YMDB catalog refines a sample of 30 well-suited detached binary systems for future mass and radius determinations. This curated dataset provides a robust observational basis for testing stellar evolution models, ultimately enabling future studies to compare dynamical and evolutionary masses. These results represent a crucial first step toward refining evolutionary tracks and improving our knowledge of the internal structure and fate of massive stars.

Acknowledgments

The author acknowledges Universidad de La Serena, the Graduate and Postgraduate Department, the Department of Astronomy, and the Doctoral Program in Astronomy. Gratitude is extended to the faculty and staff for their support. The author also thanks the thesis progress committee, the evaluation committee, as well as the thesis advisors and co-advisors. Financial support from ULS and SOCHIAS is acknowledged. Additionally, the author appreciates the resources provided by Gemini Observatory during the research internship.

Agradecimientos

Hay personas cuya presencia deja una huella imborrable, cuya influencia trasciende el tiempo y se mantiene viva en el legado que nos dejan.

En primer lugar, quiero expresar mi profundo agradecimiento a Rodolfo Barbá, quien me recibió como su estudiante y confió en mí desde el primer día. Fue él quien me abrió las puertas a la Astronomía, quien apostó por mi futuro y me ofreció la oportunidad de continuar en este camino. Haber sido su estudiante ha sido un honor inmenso. No sólo me enseñó a aprender, sino a disfrutar del proceso, a encontrar en la ciencia no sólo un desafío intelectual, sino una fuente de entusiasmo y alegría. Siempre tenía una sonrisa, un gesto de ánimo, una convicción inquebrantable en sus estudiantes. Él es el gigante a cuyos hombros quiero subirme. Su dedicación y compromiso eran inagotables, y su ausencia se siente con la misma intensidad que su legado.

A Julia, por su confianza y apoyo incondicional. Desde el principio creyó en mí, y fue su respaldo el que, en más de una ocasión, me dio la fuerza para seguir adelante. Su generosidad y mentoría han sido fundamentales en mi camino, y le estaré siempre agradecido.

A Roberto, quien, cuando todo se tornó incierto, estuvo allí para extenderme la mano. En un momento de confusión y dudas, encontró la manera de guiarme y brindarme el apoyo que necesitaba. Desde entonces, ha sido mucho más que un supervisor; ha sido un pilar en esta etapa de mi vida. Espero que esta tesis no sea más que el inicio de todo lo que podremos construir juntos.

A mi familia, por haber estado siempre a mi lado, por apoyar cada una de mis decisiones y por brindarme las oportunidades que han hecho posible este camino. Sé que no todo el mundo tiene la fortuna de contar con un respaldo así, y cada paso que doy es también un reflejo de todo lo que han hecho por mí.

Y finalmente, a Clara, mi esposa y mi mejor amiga. Por estar siempre ahí, en los buenos y malos momentos, pero sobre todo en los malos. Por su paciencia infinita, por su apoyo inquebrantable, por haber creído en mí incluso cuando yo no lo hacía. Es gracias a ella que estoy donde estoy. Me impulsa a ser mejor, a no conformarme, a aspirar siempre a la mejor versión de mí mismo. No hay palabras suficientes para expresar cuánto le debo.

A todos ellos, gracias.

Contents

List of Figures

List of Tables

List of Acronyms

BLS Box Least Squares

BSG Blue SuperGiant

CASLEO Complejo Astronómico El Leoncito

DEB Detached Eclipsing Binary

EA Eclipsing binary of Algol type

EB Eclipsing binary of Beta Lyrae type

EBAI Eclipsing Binary Artificial Intelligence

EW Eclipsing binary of W Ursae Majoris type

FEROS Fiber-fed Extended Range Optical Spectrograph

FFI Full-Frame Image

GF Gaussian Fitting

IMF Initial Mass Function

ISM InterStellar Medium

LC Light Curve

MCMC Markov Chain Monte Carlo

MK Morgan Keenan

MS Main Sequence

PDC Presearch Data Conditioning

PDM Phase Dispersion Minimization

PHOEBE PHysics Of Eclipsing BinariEs

PSPF Phase-Synchronized Polynomial Fitting

QLP Quick Look Pipeline

RMSE Root-Mean-Square Error

RSG Red SuperGiant

RV Radial Velocity

SPOC Science Processing Operations Center

TEO Tidally Excited Oscillations

TESS Transiting Exoplanet Survey Satellite

TPF Target Pixel File

VMS Very Massive Star

WR Wolf-Rayet

YMDB Young Massive Detached Binary Catalog

ZAMS Zero-Age Main Sequence

Chapter 1

Introduction

Massive stars, defined by their cataclysmic end as core collapse supernovas, are typically those with an initial mass of eight or more solar masses and they fall into the OB spectral classification in the early and mid-stages of their lives. These stellar behemoths play a crucial role in cosmic dynamics and chemical evolution, with their supernova events significantly enriching the interstellar medium with heavy elements. Understanding massive stars is fundamental to comprehending stellar evolution, the evolutionary history of galaxies, and the Universe at large. Due to their immense luminosity, they are key observable objects in distant galaxies (Schaerer et al., 2025; Massey, 2013), making them essential for astronomical studies with both current and forthcoming space and ground-based large telescopes.

Our current understanding of massive star evolution remains limited, as evidenced by the persistent mass discrepancy between empirical measurements from orbital dynamics and theoretical model predictions. This discrepancy has been a longstanding issue in astrophysics (see e.g., Herrero et al., 1992; Weidner & Vink, 2010, and references therein). Factors inherent in binary systems, such as stellar rotation, synchronization, tidal effects, limb darkening, and radiative propagation, are crucial in this context. Evolutionary models that incorporate rotation exhibit marked differences compared to nonrotating ones, including extended main-sequence lifetimes, increased luminosities, altered post-main-sequence evolution, and notably, significant variations in how mass loss is treated in massive stars (Martins & Palacios, 2013).

The determination of reliable masses for massive stars is only achievable in binary systems, particularly through the study of light curves (LCs) and radial velocity (RV) curves of eclipsing binaries. The likelihood of encountering massive stars within binary systems is fairly high, especially during their main sequence phase, the most extended period of a star's lifecycle. Comprehensive spectroscopic surveys reveal that around 75% of main sequence O-type stars (Barbá et al., 2017; Sana, 2017), and a similar ratio of early B-type stars (Chini et al., 2012), are part of gravitationally bound systems.

The endemic multiplicity among massive stars offers unique research opportunities, although the method has its limitations. An inherent consequence of binarity is the interaction among its components, which make their evolution paths deviate from those of solitary stars of similar types. This interaction issue was emphasized by Sana et al. (2012), who found that at least 71% of O-type stars in binary systems interact with their companions during their lifetimes, with 29% eventually merging into a single entity. Detecting past interactions poses challenges, as evidenced by discrepancies between empirical mass measurements and predictions from atmospheric or stellar evolution models, which often overlook these interactions.

Detached Eclipsing Binaries (DEBs) stand as critical objects in this context. These systems, characterized by a negligible or minimal interaction between their stellar components, perfectly meet the criteria for accurate stellar analysis. Given that most massive stars are part of multiple systems, it is preferable to focus on those with well-documented multiplicity. The best single stars for study are often the components of widely separated binary systems, as proposed by de Mink et al. (2011) and further discussed by Ekström (2021). DEBs provide a unique opportunity to determine the physical properties of stars with a high accuracy, such as their masses, and radii. Moreover, they can be used to determine distances Pietrzyński et al. (2013). In this context, DEBs are key objects. Determinations from DEBs form the basis for calibrating crucial relationships among stellar parameters, such as the mass–luminosity relationship Taormina et al. (2025).

Among massive stars, those within the O8–B2 spectral-type range are predominant (just as a consequence of the stellar mass distribution)[1]. However, despite their prevalence, only 20 systems within this range have had their absolute parameters determined with a precision better than 2% (Southworth, 2015, DEBCAT catalog). It is important to note that this count does not take luminosity class into account. Our research aims to address this gap by examining a selection of DEBs within this spectral range.

1.1 Thesis and Research Goals

Addressing the mass discrepancy problem requires precise empirical determinations of absolute parameters—particularly mass and radius—for massive stars. The most reliable way to achieve this is through the simultaneous study of LCs and RV curves of binary systems, where LCs provide information on the orbital inclination and radii, while RV measurements yield the dynamical masses of the components. To ensure that these masses reflect the natural evolution of single massive stars without the complexities introduced by mass transfer or tidal distortions, we focus exclusively on DEBs, where the components evolve independently. These systems provide the best empirical constraints for calibrating stellar evolution models and resolving the mass discrepancy problem in massive stars.

The primary goal of this PhD thesis is to improve the precision and availability of absolute parameters for young massive stars, particularly in the early B-type range. By leveraging high-quality photometry from the Transiting Exoplanet Survey Satellite (TESS), alongside spectroscopic classifications, this research systematically identifies and characterizes DEBs, providing a reliable dataset for future calibrations of stellar evolution models.

Catalogs play an essential role in astronomy, providing structured datasets that support statistical analysis, reproducibility, and long-term data reuse (e.g., Chen et al., 2022). In this context, the astronomical

[1] The stellar Initial Mass Function (IMF), first quantified by Salpeter (1955), describes the relative number of stars formed at different masses. It follows a power-law distribution, where lower-mass stars are far more common than their massive counterparts. As a result, stars in the O8–B3 range are observed more frequently than the most massive O-type stars, simply due to their higher formation rates.

community has increasingly emphasized best practices for catalog publication and stewardship, including the FAIR principles (Findability, Accessibility, Interoperability, and Reusability), to ensure long-term scientific value (Wilkinson et al., 2016). A major outcome of this work is the Young Massive Detached Binary (YMDB) catalog, which compiles detailed photometric and spectroscopic information for a carefully selected sample of massive stars. This catalog serves as a tool to bridge the gap between theory and observations, allowing for robust constraints on stellar structure and evolution.

To achieve these objectives, we:

- Curated a well-defined sample of young massive binaries (Sect. 3.1).
- Generated and analyzed light curves (LCs) using TESS photometry, identifying detached binaries and extracting key orbital parameters such as periods, eccentricities, and ephemerides (Sect. 3.2).
- Examined additional phenomena, such as pulsations and heartbeat variations, which can impact the determination of fundamental parameters.
- Performed spectral classification for targets with ambiguous or conflicting classifications in the literature, ensuring a consistent dataset for our study (Sect. 3.3).
- Produced a catalog of high-quality empirical parameters to facilitate improvements in stellar evolution models (Sect. 4.1).

1.2 Structure of the Thesis

This thesis is structured as follows:

- **Chapter 2** provides the theoretical background necessary to understand the evolution and classification of massive stars. It begins by describing their evolutionary pathways, from their formation to their end stages as supernovae, neutron stars, or black holes. It also explores spectral classification, detailing the features of O- and B-type stars and their significance in determining fundamental stellar parameters. A major focus is given to the *mass discrepancy problem*, discussing how dynamical masses derived from binary systems often differ from theoretical predictions and exploring possible causes such as convective core overshooting, rotation, mass loss, and mixing processes. The chapter concludes with a discussion of how *detached eclipsing spectroscopic binaries* serve as fundamental tools for determining absolute stellar parameters, providing empirical constraints to improve evolutionary models.
- **Chapter 3** describes the methodology behind the creation of the *Young Massive Detached Binary (YMDB) catalog* and the process of absolute parameter determination. It details the *sample selection criteria*, including the identification of candidate detached eclipsing binaries from TESS light curves, spectroscopic surveys, and literature sources. The chapter also outlines the *data reduction techniques* applied to photometric and spectroscopic datasets, describing calibration steps,

radial velocity extraction, and spectral classification. Furthermore, the methodology for modelling eclipsing binaries using PHOEBE is described, discussing how different observational scenarios (e.g., single-lined vs. double-lined binaries, presence or absence of eclipses) impact parameter determination.

- **Chapter 4** presents the results of this work, detailing the construction of the YMDB catalog. It highlights the identification of 20 new eclipsing binaries, including 13 previously unrecognized variable systems, and provides new light curve classifications for 30 systems. The study also reports newly detected heartbeat features, eccentricities, and other variability phenomena. Additionally, spectral classifications were confirmed or newly determined for multiple systems. The YMDB catalog serves as a foundation for future studies, identifying 30 strong candidates for absolute parameter determination, which will enable comparisons with stellar evolutionary models.

- **Chapter 5** summarizes the key conclusions drawn from this study, emphasizing how the findings contribute to resolving uncertainties in massive star evolution. It also outlines both ongoing and future research directions, including the public release of the TESS light curve pipeline, the expansion of the YMDB catalog with additional spectroscopic observations, the spectroscopic follow-up of understudied YMDB systems, and the extension of the methodology to earlier spectral types (O7–O9). The importance of continued observational efforts to improve empirical constraints on massive star evolution is emphasized, as well as the role of detached binaries in refining theoretical stellar models.

Chapter 2

Theoretical Background

2.1 Massive Stars: Evolution, Spectral Classification, and Observational Significance

Massive stars are defined by their eventual fate as core-collapse supernovae, with theoretical models predicting that those with an initial mass greater than $\sim 8M_\odot$ at the Zero-Age Main Sequence (ZAMS) will reach this explosive end. These stars play a crucial role in the evolution of galaxies by injecting substantial amounts of energy, momentum, and newly synthesized heavy elements into the interstellar medium (ISM) throughout their lifetimes. Their immense luminosities ($\sim L > 10^3 - 10^6 L_\odot$), high effective temperatures ($\sim 22,000$ K – $45,000$ K), and strong stellar winds contribute significantly to shaping their surroundings and driving large-scale galactic evolution (Martins et al., 2005; Oswalt & Barstow, 2013; Salaris & Cassisi, 2005).

The life cycle of a massive star is markedly different from that of a lower-mass star, primarily due to the efficiency of nuclear reactions and the influence of mass loss throughout its evolution. From their formation within dense molecular clouds to their final fate as neutron stars or black holes, massive stars undergo a sequence of evolutionary stages characterized by distinctive physical processes and observational signatures. Their intense radiation drives powerful winds that shape their surroundings, while their eventual explosive deaths enrich the universe with heavy elements (Shaviv, 2009; Lamers & Cassinelli, 1999).

2.1.1 Formation and Early Evolution

Understanding the evolutionary pathways of massive stars provides insights into supernova mechanisms, gamma-ray bursts, and the origins of compact stellar remnants.

Massive stars form within giant molecular clouds, particularly in high-density environments where gravitational instabilities lead to fragmentation and subsequent star formation. Unlike low-mass stars, massive stars tend to form in clustered environments, often as part of binary or multiple systems (Livio & Villaver, 2009). The high accretion rates during their formation ($10^{-4} - 10^{-3} M_{\odot}/\text{yr}$) enable them to reach their final mass rapidly before stellar feedback from radiation pressure halts further accretion (Oswalt & Barstow, 2013).

Due to their large mass, contraction proceeds quickly via the Kelvin-Helmholtz mechanism, leading to core temperatures sufficient to initiate hydrogen fusion via the CNO cycle. This process dominates energy production in stars exceeding $\sim 1.5 M_{\odot}$, contrasting with the slower proton-proton chain in lower-mass stars (Salaris & Cassisi, 2005).

The Initial Mass Function (IMF) describes the distribution of stellar masses at the time of formation and plays a fundamental role in understanding the relative populations of massive stars. While the IMF is complex and best represented using multi-part power laws, particularly over the full stellar mass range (Kroupa & Jerabkova, 2021; Kroupa et al., 2024), at the high-mass end it is commonly approximated by a single power law of the form $\xi(m) \propto m^{-\alpha}$, with $\alpha \approx 2.3$ (Corbelli et al., 2005). This steep slope implies that low-mass stars are far more numerous than massive stars, yet the latter dominate the energetic and chemical evolution of galaxies due to their immense luminosities and short lifetimes. Multiplicity plays a significant role in this context, as it can affect both the determination of the total stellar mass in clusters and the inferred slope of the IMF (as shown in the case of 30 Doradus Schneider et al., 2018a; Farr & Mandel, 2018; Schneider et al., 2018b).

Massive stars are thought to originate preferentially in high-density regions within stellar clusters, often forming in binary or multiple systems (Livio & Villaver, 2009). The fragmentation of molecular clouds, competitive accretion, and dynamical interactions in young clusters influence the high-mass end of the IMF (Salaris & Cassisi, 2005). The observed upper mass limit of $\sim 150 M_{\odot}$ in the local universe suggests physical constraints imposed by radiation pressure and mass-loss processes (Oswalt & Barstow, 2013).

The IMF is crucial for predicting the population synthesis of galaxies, determining the frequency of supernovae, and influencing models of chemical enrichment. Understanding the IMF variations across different environments remains an ongoing challenge in astrophysics, with implications for galaxy evolution and cosmology (Corbelli et al., 2005).

Once core hydrogen burning begins, the star enters the Main Sequence (MS), characterized by stable hydrostatic equilibrium maintained by radiation pressure and energy generation from hydrogen fusion. The duration of this phase depends on the initial mass (Hansen & Kawaler, 1994), as illustrated by the following approximate values:

- $10 M_{\odot}$: 30 Myr
- $25 M_{\odot}$: 3 Myr
- $50 M_{\odot}$: 0.5 Myr
- $100 M_{\odot}$: 0.1 Myr

Massive stars on the MS exhibit strong stellar winds, losing mass at rates of $10^{-7} - 10^{-5} M_{\odot}/\text{yr}$, which influences their later evolutionary stages (Lamers & Cassinelli, 1999). Fast rotation (up to hundreds of km/s) induces mixing, affecting surface abundances and extending the duration of core hydrogen burning (Oswalt & Barstow, 2013).

2.1.2 Late Evolution and Final States

As core hydrogen is exhausted, the star undergoes core contraction, leading to the ignition of helium fusion in a convective core. The outer layers expand, and the star moves off the MS. During this post-main-sequence phase, the star's appearance and fate diverge depending on its initial mass, rotation, and the degree of mass loss. While traditional classifications refer to Red Supergiants (RSGs), Blue Supergiants (BSGs), and Wolf-Rayet (WR) stars as distinct types, these represent observable phases shaped by the structure of the hydrogen envelope and the resulting surface temperature:

- **Red Supergiants**: Stars with masses of ~ 8–$15 M_{\odot}$ typically develop extended, cool, hydrogen-rich envelopes during core helium burning. These stars usually retain their envelopes and remain in the RSG phase until core collapse, exploding as Type II-P supernovae (Ekström et al., 2012). The envelope's cool hydrogen leads to surface temperatures of ~ 3500–4500 K, producing a red spectrum that contrasts sharply with their earlier blue main-sequence appearance. More massive stars, up to $\sim 30 M_{\odot}$, can also become RSGs, but their extended envelopes are more fragile. Sustained mass loss—driven by radiation, convection, and sometimes pulsations, can cause the envelope to shrink, increasing the star's surface temperature and leading to a transition into the BSGs.
- **Blue Supergiants**: In more massive stars (~ 25–$40 M_{\odot}$), strong winds or rotational mixing reduce the envelope mass, leading to a compact structure and a hotter surface with temperatures of $\sim 10,000$–$30,000$ K. The higher surface temperatures shift the peak of the spectral energy distribution toward the blue, hence called Blue Supergiants. Some stars enter the BSG phase after losing part of their envelope during a preceding RSG phase; others reach it directly from the MS if envelope loss began early. These stars may oscillate between RSG and BSG phases as their core and envelope structures evolve; a behavior known as blueward evolution. One or more transitions may occur before the star ends its life.
- **Wolf-Rayet (WR) stars**: When mass loss is sufficient to strip the entire hydrogen envelope—either in very massive stars ($\gtrsim 30 M_{\odot}$) or through binary interaction—the hot helium core becomes exposed, and the star's spectrum changes dramatically. These stars are classified as Wolf-Rayet stars and show broad emission lines dominated by He, N, C, or O (Ekström et al., 2012; Livio & Villaver, 2009). The WR types are divided into subtypes based on these surface dominant abundances: WN (nitrogen-rich), WC (carbon-rich), and WO (oxygen-rich). The progression from WN to WC and finally WO corresponds to successive unveiling of the products of H- and He-burning, respectively, and reflects increasing depth into the core. The sequence typically follows significant wind-driven mass loss, either post-BSG or while still near the MS, and is known as the Conti scenario (Crowther, 2007). WR stars often represent the final evolutionary stage before core collapse, leading to stripped-envelope supernovae of Types Ib or Ic.

During this phase, additional nuclear burning occurs, progressing from helium to carbon, oxygen, and eventually silicon, leading to the formation of an iron core (Shaviv, 2009). Once the core accumulates iron, nuclear fusion ceases, leading to core collapse due to degeneracy pressure failure. The outcome of the collapse depends on the initial mass:

- **Neutron Stars**: Stars in the range of ~ 8–$25M_\odot$ typically undergo core-collapse supernovae (SNe; Types II-P, II-L, Ib/c), leaving behind neutron stars (NS) (Oswalt & Barstow, 2013). In compact binary systems, mergers between neutron stars can produce kilonovae (KNe), enriched with heavy r-process elements (Salaris & Cassisi, 2005).

- **Black Holes**: More massive stars ($> 25M_\odot$) may form black holes (BH) either via fallback after a weak supernova or through direct collapse with little or no visible SN signature. Some may also produce long-duration gamma-ray bursts (Livio & Villaver, 2009).

Explosions from SNe and KNe inject substantial energy into the ISM, triggering star formation and distributing newly synthesized elements (Shaviv, 2009). Massive stars are pivotal in shaping galactic evolution through their extreme luminosities, stellar winds, and explosive endpoints. Their ability to synthesize and disperse heavy elements is fundamental to the chemical evolution of galaxies. Furthermore, the interplay of mass loss, rotation, and binary interactions continues to challenge theoretical models, necessitating further observations and simulations. Understanding these stars is essential for deciphering the broader cosmic landscape, including the formation of compact objects, the interstellar medium's enrichment, and the origins of cosmic explosions (Lamers & Cassinelli, 1999; Oswalt & Barstow, 2013)

2.1.3 Spectral Classification and Features

Massive stars are primarily classified as O and B spectral types, which are characterized by their high temperatures, strong ionization features, and unique line profiles. Spectral classification plays a crucial role in understanding stellar structure and evolution, as it provides insight into a star's effective temperature, ionization state, mass loss, and rotation rates. The classification of these stars is based on a systematic analysis of their spectral features, particularly the presence and strength of hydrogen, helium, and metal lines, which evolve as the stars progress through their lifetimes. This classification is essential for determining fundamental stellar parameters such as luminosity, temperature, and mass, and provides a basis for understanding their physical processes, interactions with their environments, and overall contribution to galactic evolution (Gray & Corbally, 2009; Maíz Apellániz et al., 2024).

2.1.3.1 O-type Stars

O-type stars are the hottest and most massive stars, typically exhibiting:

- **Effective Temperatures:** O-type stars have surface temperatures ranging from approximately $30,000$–$50,000$ K, making them some of the hottest main-sequence stars in the universe. Their high temperatures lead to strong ionization effects in their atmospheres, profoundly influencing their spectral characteristics.

- **Ionization State:** The spectra of O-type stars are dominated by ionized helium (He II) lines, as well as weak neutral helium (He I) lines. Hydrogen Balmer lines are also present but can appear weaker than in cooler stars due to strong ionization effects. In addition, metal lines such as those of CIII, OIII, and SiIV are present depending on metallicity and atmospheric conditions.

- **Winds and Mass Loss:** O-type stars exhibit significant mass loss through stellar winds, which are driven by intense radiation pressure. These winds lead to characteristic P-Cygni profiles in ultraviolet (UV) spectra, particularly in resonance lines of NV, CIV, and SiIV. These features indicate strong outflows of material, which significantly impact both the star's evolution and the surrounding ISM (Walborn et al., 1985).

- **Rotation Effects:** Many O-type stars rotate at high velocities, often exceeding several hundred km/s. This rapid rotation can lead to significant line broadening, impacting the spectral classification. Rotation also affects the shape of stellar winds and may influence the star's evolution by inducing mixing of chemical elements within the stellar interior.

- **Metallicity Influence:** Metal lines in O-type stars provide insight into the composition of their atmospheres and evolutionary history. In low-metallicity environments, such as those found in the early universe or in metal-poor galaxies, O-type stars exhibit weaker metal lines due to reduced initial chemical abundances. These differences are critical for understanding star formation and feedback processes in different galactic environments.

The presence of strong winds and ionized lines in O-type stars makes them key players in shaping their cosmic surroundings. Their extreme temperatures and radiation output can trigger star formation, ionize nearby gas clouds, and influence galactic dynamics. Additionally, their winds contribute to the chemical enrichment of galaxies by distributing heavy elements synthesized in their interiors.

2.1.3.2 B-type Stars

B-type stars, while cooler than O-type stars, still exhibit high temperatures and strong ionization features. Their spectra are rich with hydrogen Balmer lines and neutral helium transitions, making them distinct from both the hotter O-type and cooler A-type stars.

- **Effective Temperatures:** B-type stars have temperatures ranging from approximately $10,000$–$30,000$ K. This range leads to a complex interplay of spectral lines, including strong hydrogen lines and neutral helium features that gradually weaken toward later B spectral subclasses.

- **Spectral Lines:** Unlike O-type stars, B-type stars show dominant hydrogen Balmer lines alongside strong neutral helium (He I) transitions. These features allow for detailed temperature classification and provide insight into the star's atmospheric structure. Some early-type B stars may also exhibit weak He II lines, bridging the transition between O and B stars (Gray & Corbally, 2009).

- **Winds and Outflows:** Although B-type stars exhibit mass loss through stellar winds, their winds are generally weaker than those observed in O-type stars. Some early B-type stars may still show weak P-Cygni features in UV spectra, indicating ongoing outflows. In contrast, late B-type stars exhibit lower mass-loss rates, reducing the prominence of wind-related spectral features.

- **Variability and Circumstellar Features:** Some B-type stars, particularly Be stars, exhibit significant emission features due to the presence of circumstellar disks. These disks arise from rapid rotation, leading to the ejection of material from the star's equator. The emission features observed in these stars are typically seen in the Balmer series and can vary over time, providing valuable insight into stellar rotation and mass loss mechanisms.

- **Magnetic Fields:** Some B-type stars possess detectable magnetic fields, which influence their spectral profiles and the dynamics of their stellar winds. These fields can lead to structured mass loss patterns and influence the long-term evolution of the star. In addition, magnetic B stars may exhibit peculiar chemical compositions due to diffusion processes, altering their observed spectra (Kogure & Leung, 2007).

B-type stars provide crucial information about the transition between massive and intermediate-mass stellar populations. Their spectral features enable precise temperature and luminosity determinations, while variability in some B-type stars offers insight into stellar rotation and circumstellar environments.

2.2 The Mass Discrepancy Problem in Stellar Astrophysics

The mass discrepancy problem refers to the inconsistency between masses derived from observational techniques, such as binary star dynamics, and those predicted by theoretical stellar evolution models. This discrepancy is particularly prominent in massive stars, where observed dynamical masses can be up to 30% higher for evolved stars (Tkachenko et al., 2020) and can exceed 50% in some cases for lower-mass O-type stars (Markova et al., 2018).

While the mass discrepancy has long been recognized in O-type stars, recent studies suggest that it may be even more pronounced in B-type stars. In particular, Weidner & Vink (2010) noted that Cantiello et al. (2009), based on data from Trundle et al. (2007) and Hunter et al. (2008), reported a highly significant mass discrepancy for B-type stars, with evolutionary masses up to a factor of three larger than spectroscopic ones. This underscores the need to refine stellar models, especially for lower-mass massive stars in the B spectral range, and suggests that the mass discrepancy problem may depend on spectral type, potentially indicating missing physics in stellar models at different mass regimes.

Observations of detached eclipsing binary stars provide precise dynamical masses, independent of stellar evolution assumptions. However, these empirically derived masses often do not match predictions from stellar evolutionary models, particularly in the case of high-mass stars (Tkachenko et al., 2020). This discrepancy arises because evolutionary models rely on assumptions about internal stellar processes—such as convective mixing, rotation, and mass loss—that remain poorly constrained (Markova et al., 2018). Studies focusing on massive stars suggest that this issue is particularly significant in O and early B-type stars, where evolutionary models tend to overestimate stellar masses (Weidner & Vink, 2010; Markova et al., 2018). These inconsistencies highlight the need for continued improvements in stellar models, as incorrect mass estimates can propagate into errors in evolutionary tracks, main-sequence lifetimes, and stellar population synthesis (Tkachenko et al., 2020).

Despite extensive theoretical efforts, no single mechanism fully accounts for the mass discrepancy, highlighting the need for more empirical constraints, particularly for massive B-type stars where the issue appears to be more severe. Expanding the dataset of well-characterized detached eclipsing binaries in this mass regime is essential for testing model predictions and refining mass-luminosity and mass-radius relations. Several mechanisms have been proposed to explain the discrepancy, including uncertainties in near-core mixing, mass-loss rates, rotational mixing, and magnetic fields (Tkachenko et al., 2020; Markova et al., 2018). However, the issue remains far from settled due to the lack of sufficient high-precision empirical data, underscoring the importance of observational efforts to bridge the gap between models and reality.

2.2.1 The Role of Empirical Data in Resolving the Discrepancy

One of the most effective ways to address this problem is through detached DEB systems, which provide precise dynamical masses independent of stellar evolution models. These empirical constraints are essential for testing and improving theoretical predictions. However, despite their importance, massive DEBs remain scarce. Meanwhile, the mass discrepancy appears to be more severe in B-type stars than in O-type stars, as reported by Weidner & Vink (2010). Expanding the sample of well-characterized DEBs in this mass regime is therefore a critical step toward resolving this issue.

This thesis contributes to that effort by identifying and characterizing a set of promising DEB candidates within the O8–B3 spectral range. By systematically analyzing TESS light curves and complementing them with spectroscopic information, this work lays the foundation for future studies that will determine absolute stellar parameters for these systems. These measurements, in turn, will enable direct comparisons with theoretical masses predicted by stellar evolution models and contribute to refining stellar models in this mass regime.

Although the mass discrepancy problem remains unsolved, this work represents a step toward addressing it by providing a well-defined sample of systems suitable for empirical mass determinations. The YMDB catalog is designed to serve as a benchmark dataset, helping to bridge the gap between observational constraints and theoretical models. Future spectroscopic follow-ups of these systems will be crucial for directly quantifying discrepancies and refining our understanding of massive star evolution.

2.3 Determining Absolute Parameters with Eclipsing Spectroscopic Binaries

Binary star systems, particularly eclipsing spectroscopic binaries, serve as the most reliable method for determining the absolute fundamental parameters of stars, such as mass, radius, luminosity, and temperature. Unlike single stars, where mass can only be inferred indirectly from evolutionary models and theoretical mass-luminosity relations, binary systems provide direct empirical measurements through Kepler's laws when radial velocity curves and light curves are available.

Additionally, spectral classification plays a crucial role in constraining stellar parameters. By analyzing spectral features, astronomers can estimate effective temperature, surface gravity, and luminosity class, providing key priors for modelling binary systems. This classification also informs the choice of stellar atmosphere models used in light curve and radial velocity fitting.

Other methods, such as asteroseismology and gravitational microlensing, also offer insights into stellar parameters. However, eclipsing detached binaries provide the most direct and precise method for determining absolute masses and radii, as emphasized in studies on binary modelling and analysis (Kallrath & Milone, 2009; Prša et al., 2016).

2.3.1 Spectral Classification in the Context of Binary Parameter Determination

Spectral classification is a fundamental tool in stellar astrophysics, providing essential constraints on stellar properties and evolution. One of its key applications is estimating stellar masses and radii, as empirical relations derived from classification allow for mass and radius determinations, aiding in the refinement of stellar evolution models. Additionally, spectral classification enables precise temperature measurements by analyzing ionization balances, such as the He II/He I ratio in O and early B-type stars, which serve as direct indicators of surface temperature and are crucial for understanding stellar atmospheres and interiors.

Beyond individual stellar properties, classification also provides insight into a star's evolutionary status. By determining luminosity classes—such as dwarfs, giants, or supergiants—it is possible to establish a snapshot of a star's evolutionary phase, which in turn helps refine models of stellar lifetimes. Spectral data also reveal information about mass loss and stellar winds. The presence of P-Cygni profiles, UV resonance lines, and emission features in hot stars provides direct evidence of wind-driven mass loss, a critical process influencing stellar feedback in galaxies.

High-resolution spectroscopy further allows for the modelling of stellar atmospheres. By generating synthetic spectra that replicate observed line strengths, classification contributes to improving atmospheric models and refining our understanding of radiative transfer in hot, massive stars (Böhm-Vitense, 1997). The combination of UV, optical, and infrared spectroscopy is therefore essential for fully characterizing massive star atmospheres and their role in galactic evolution. As one of the most powerful tools in modern astrophysics, spectral classification continues to provide fundamental insights into stellar physics, chemical enrichment, and the broader context of cosmic structure formation.

2.3.2 Constraints for Light Curve and Radial Velocity Observability

The ability to measure LCs and RV curves depends on system geometry and observational limitations. Figure 2.3.1 illustrates the geometry of a binary system, showing the true orbit and its projection along the line of sight. The inclination angle i, along with other orbital parameters such as the longitude of the ascending node Ω and the argument of periastron ω, determines whether eclipses are observable and influences the radial velocity curve. Consequently, the ability to extract fundamental stellar parameters

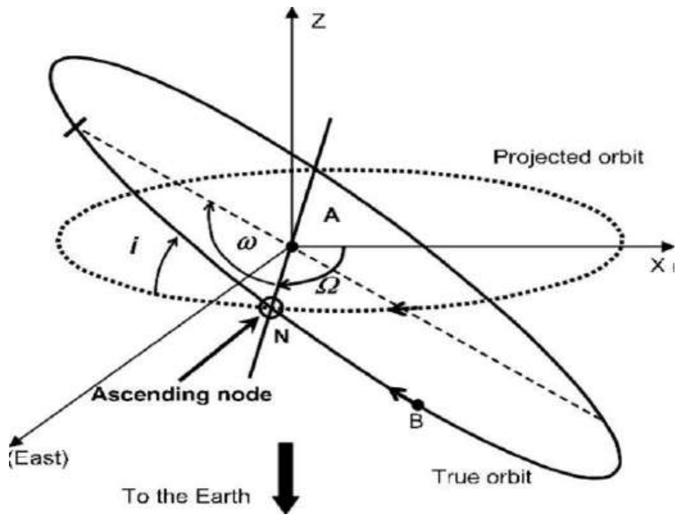

Figure 2.3.1: Schematic representation of the orbital geometry of a binary system. The true orbit (solid line) and its projection onto the plane of the sky (dashed line) are shown. The inclination angle i, ascending node N, and argument of periastron ω play crucial roles in determining the observability of eclipses and radial velocity variations.

varies depending on the available observational constraints, as summarized in Table 2.3.1.

- **Eclipses in Light Curves**: The presence of eclipses is determined by the inclination angle i of the system and the relative radii of the stars:

$$\cos i \leq \frac{R_1 + R_2}{a} \tag{2.3.1}$$

  where R_1, R_2 are the radii of the stars, and a is the semi-major axis. If this criterion is not met, no eclipses occur, while partial or full eclipses are seen for higher inclinations.

- **Radial Velocity Detection**: The detectability of radial velocity variations depends on the orbital inclination and brightness contrast. A significant velocity shift is only observable if:

$$v_r = K \sin i \tag{2.3.2}$$

  where K is the semi-amplitude of the radial velocity curve, and it must be sufficiently large to be detected against observational noise. If only one star exhibits detectable shifts, the system falls into the SB1 category, whereas systems where both stars are observable fall into SB2.

- **Magnitude Differences and Blending**: Even if an eclipse or velocity shift is theoretically present, a large magnitude difference (ΔM) between the two components may prevent detection, as the fainter component contributes negligibly to the total flux.

Table 2.3.1: Extractable Parameters in Observational Scenarios

Parameter		No Eclipses		Eclipsing		
		SB1	SB2	SB0	SB1	SB2
Orbital parameters						
Orbital period	P	✓	✓	✓	✓	✓
Orbital eccentricity	e	✓	✓	✓	✓	✓
Argument of periastron	ω	✓	✓	✓	✓	✓
Longitude of ascending node	Ω					
Projected semimajor axis	a sin(i)		✓			✓
True semimajor axis	a					✓
Orbital inclination	i			✓	✓	✓
Distance	d					✓
Spectroscopic parameters						
Velocity amplitude of star 1	K_1	✓	✓		✓	✓
Velocity amplitude of star 2	K_2		✓			✓
Systemic velocity	V_γ	✓	✓		✓	✓
Mass function	f(M)	✓	✓		✓	✓
Mass ratio	q		✓			✓
Mass sum	M		✓			✓
Individual minimum masses	$M_j \sin^3(i)$		✓			✓
Individual masses	M_1,M_2					✓
Size parameters						
Individual fractional radii	r_1,r_2			✓	✓	✓
Individual Radii	R_1,R_2					✓
Surface gravity of primary	log g1					✓
Surface gravity of secondary	log g2				✓	✓
Individual densities	ρ1,ρ					✓
Radiative parameters						
Temperature of primary star	$Teff_1$	✓	✓		✓	✓
Temperature of secondary star	$Teff_2$		✓			✓
Individual Luminosities	L_1,L_2					✓
Luminosity of secondary star	L2					✓

Note: Summary of measurable parameters under various observational scenarios for binary star systems. The scenarios include combinations of systems with or without eclipses, along with observable from one (SB1), both components (SB2), or none (SB0). Table adapted from Southworth (2020).

2.3.3 Mathematical Derivations for Parameter Estimation

RV measurements provide critical constraints on stellar masses and orbital parameters. The RV of a star in a binary system varies due to the Doppler effect as the star moves along its orbit. The observed RV as a function of orbital phase is given by:

$$V = V_0 + K\left[\cos(\theta+\omega) + e\cos\omega\right] \tag{2.3.3}$$

where V is the observed RV, V_0 is the systemic velocity, K is the velocity semi-amplitude, θ is the true anomaly, ω is the argument of periastron, and e is the eccentricity.

The RV semi-amplitude K of each component is given by:

$$K_1 = \frac{2\pi a_1 \sin i}{P\sqrt{1-e^2}} \tag{2.3.4}$$

$$K_2 = \frac{2\pi a_2 \sin i}{P\sqrt{1-e^2}} \tag{2.3.5}$$

where a_1, a_2 are the semi-major axes of the components, P is the orbital period, e is the eccentricity, and i is the inclination of the orbit.

In a system where only one component's RV is measured (SB1), the mass function $f(m)$ is given by:

$$f(m) = \frac{K_1^3 P}{2\pi G} = \frac{(M_2 \sin i)^3}{(M_1+M_2)^2} \tag{2.3.6}$$

This equation provides a lower limit on the companion mass M_2, given that i is unknown.

If both components' RVs are measurable (SB2 system), the mass ratio can be determined directly from their velocity amplitudes:

$$\frac{M_1}{M_2} = \frac{K_2}{K_1} = q \tag{2.3.7}$$

The absolute stellar masses are derived using Kepler's third law when both RV components are available:

$$M_1 + M_2 = \frac{4\pi^2 a^3}{GP^2} = \frac{(K_1+K_2)^3 P}{G\sin^3 i} \tag{2.3.8}$$

For individual masses:

$$M_1 = \frac{K_1 P}{2\pi G}\frac{(1+q)^2}{q^3 \sin^3 i}, \quad M_2 = qM_1 \tag{2.3.9}$$

This equation allows for mass determination if the inclination i is known (e.g., from eclipsing binary light curves). The radii of the stars can be estimated from light curves via:

$$\frac{R_1 + R_2}{a} = \Delta\phi \tag{2.3.10}$$

where $\Delta\phi$ represents the observable eclipse width in phase units. The exact determination of stellar radii requires an eclipse and the presence of a secondary component.

The combination of photometric and spectroscopic data enables the determination of stellar parameters:

- Orbital inclination i from eclipsing systems.
- Masses from radial velocity amplitudes and orbital inclination.
- Radii from light curve fitting (eclipses constrain R_1, R_2).
- Temperatures from spectral type and multi-band photometry.
- Surface gravity ($\log g$) from mass and radius relations.

These equations form the foundation of binary star parameter determination, particularly in detached systems where tidal interactions and mass transfer do not complicate the interpretation.

2.3.4 The PHOEBE Code and Wilson-Devinney Method

PHOEBE (PHysics Of Eclipsing BinariEs) (Prša & Zwitter, 2005; Prša et al., 2016) is a powerful computational tool designed for modelling eclipsing and spectroscopic binary stars. Originally developed as an extension of the Wilson-Devinney code (Wilson & Devinney, 1971), PHOEBE has introduced significant improvements in solving the inverse problem (see Conroy et al., 2020, and references therein), where observed LCs and RVs are used to determine stellar parameters. The code provides a robust framework to model binary systems by incorporating a wide range of physical effects.

One of the major advancements in PHOEBE is its ability to handle complex systems by including third-light contamination, spots, and reflection effects. These factors are crucial when analyzing real observations, where contaminating sources or surface inhomogeneities can significantly alter the light curves. Furthermore, PHOEBE has expanded its capabilities by integrating atmosphere models to account for realistic stellar surface brightness distributions.

PHOEBE also includes multiple solvers that improve parameter estimation. These solvers use techniques such as Markov Chain Monte Carlo (MCMC) and genetic algorithms to efficiently explore parameter space and determine the most likely values. This enhances the accuracy of binary system modelling and helps address degeneracies that arise when multiple parameter combinations fit the data equally well.

Another key feature of PHOEBE is its improved treatment of limb darkening, gravity darkening, and reflection effects, all of which are necessary for accurately reproducing light curves. By incorporating Roche geometry constraints, the software ensures that mass transfer effects and tidal distortions are properly accounted for in close binaries.

With perfect observational data, PHOEBE can achieve parameter uncertainties as low as a few percent. However, realistic constraints depend on observational limitations such as signal-to-noise ratio, time sampling, and systematic errors. The expected accuracy of derived masses and radii typically ranges between 1-5%, which is sufficient for calibrating stellar evolution models and resolving discrepancies such as the mass discrepancy problem in massive stars.

These accuracy levels are crucial for resolving the mass discrepancy problem in stellar astrophysics. DEBs serve as empirical benchmarks for calibrating evolutionary models, as their components are not significantly interacting, allowing for independent determination of fundamental parameters without reliance on evolutionary assumptions.

Advancements in space-based photometric missions, such as TESS and Kepler, have enabled the determination of stellar masses and radii with uncertainties as low as 1–2%. Works compiled by Southworth (2015) demonstrate the level of accuracy that has been achieved, leading us to expect and aim for mass and radius measurements with uncertainties below 2%, although they can reach as low as 0.5%, as demonstrated by Miller et al. (2022) for the detached F-type eclipsing binary CPD-54 810 using TESS photometry. Similarly, comparable precision has been achieved for detached eclipsing binaries from Kepler data, as shown by Cruz et al. (2022).

2.4 Classification of light Curves

Stars emit light that can be measured over time, and in many cases, their brightness appears constant. However, some stars exhibit variations in brightness due to intrinsic or extrinsic factors. When we plot the measured brightness of a star as a function of time, we obtain a light curve. These curves are a fundamental tool for studying variable stars, as they encode information about the underlying physical processes causing the observed variations.

One important class of variable stars is eclipsing binaries. These are binary star systems in which the relative orientation of the orbit and the sizes of the stars allow one star to partially or completely block the light of the other as seen from Earth. In these cases, the light curve displays characteristic brightness dips at regular intervals, corresponding to the primary and, in some cases, secondary eclipses. The shape of the light curve depends on several factors, including the orbital inclination, stellar radii, and orbital configuration of the system

2.4.1 Types of Eclipsing Binary Light Curves

Eclipsing binaries are classified according to their light curve morphology[1] (see Fig. 2.4.1):

- **Algol-type (EA)**: These are systems where the components are nearly spherical or only slightly ellipsoidal. The light curve exhibits well-defined eclipses with sharp ingress and egress phases, and the brightness remains nearly constant between eclipses. Secondary minima may be absent. These systems typically have detached components, meaning they do not significantly distort each other. Detached eclipsing binaries, such as those in the YMDB, generally fall into this category.

- **β Lyrae-type (EB)**: These systems have ellipsoidal components, meaning that tidal forces distort the stars into elongated shapes. The light curve shows continuous brightness variations, making it impossible to define precise ingress and egress times for the eclipses. A secondary minimum is always present but is usually shallower than the primary. The components of EB-type binaries are typically early-type (B-A) stars.

- **W Ursae Majoris-type (EW)**: These are short-period systems, usually with orbital periods of less than a day, where the components are nearly in contact. The light curve shows a nearly sinusoidal variation, with the primary and secondary eclipses having nearly equal depths or differing only slightly. The components generally belong to later spectral types (F-G).

In addition to the classical EA, EB, and EW types, some close binaries exhibit photometric variability caused by tidal distortions rather than eclipses. These **ellipsoidal variables** have components deformed by mutual gravity, producing quasi-sinusoidal light curves due to changes in the projected stellar area as they orbit. At low or moderate inclinations, no eclipses occur, but the variability may closely resemble that of EB or EW systems. This can lead to misclassification, especially in large photometric surveys where orbital inclination is unknown. Differentiating eclipses from ellipsoidal modulation is therefore important when interpreting binary light curves (Morris, 1985).

2.4.2 Eccentricity and its effects

In most eclipsing binaries, the two stars orbit their common center of mass, and the timing of eclipses depends on the system's orbital eccentricity (e) and argument of periastron (ω). In a circular orbit ($e = 0$), the primary eclipse occurs at phase 0.0 and the secondary at phase 0.5. In an eccentric orbit ($e > 0$), the secondary eclipse can occur at any phase other than 0.5, depending on the value of ω. If the secondary eclipse is offset from phase 0.5, the system is definitively eccentric. However, if it appears at 0.5, the orbit may or may not be eccentric.

Apsidal Motion: Over time, the argument of periastron (ω) can shift due to gravitational interactions between the stars and tidal effects, causing a gradual rotation of the elliptical orbit within the orbital

[1] Following the definitions provided by the General Catalogue of Variable Stars (GCVS; Samus' et al., 2017)

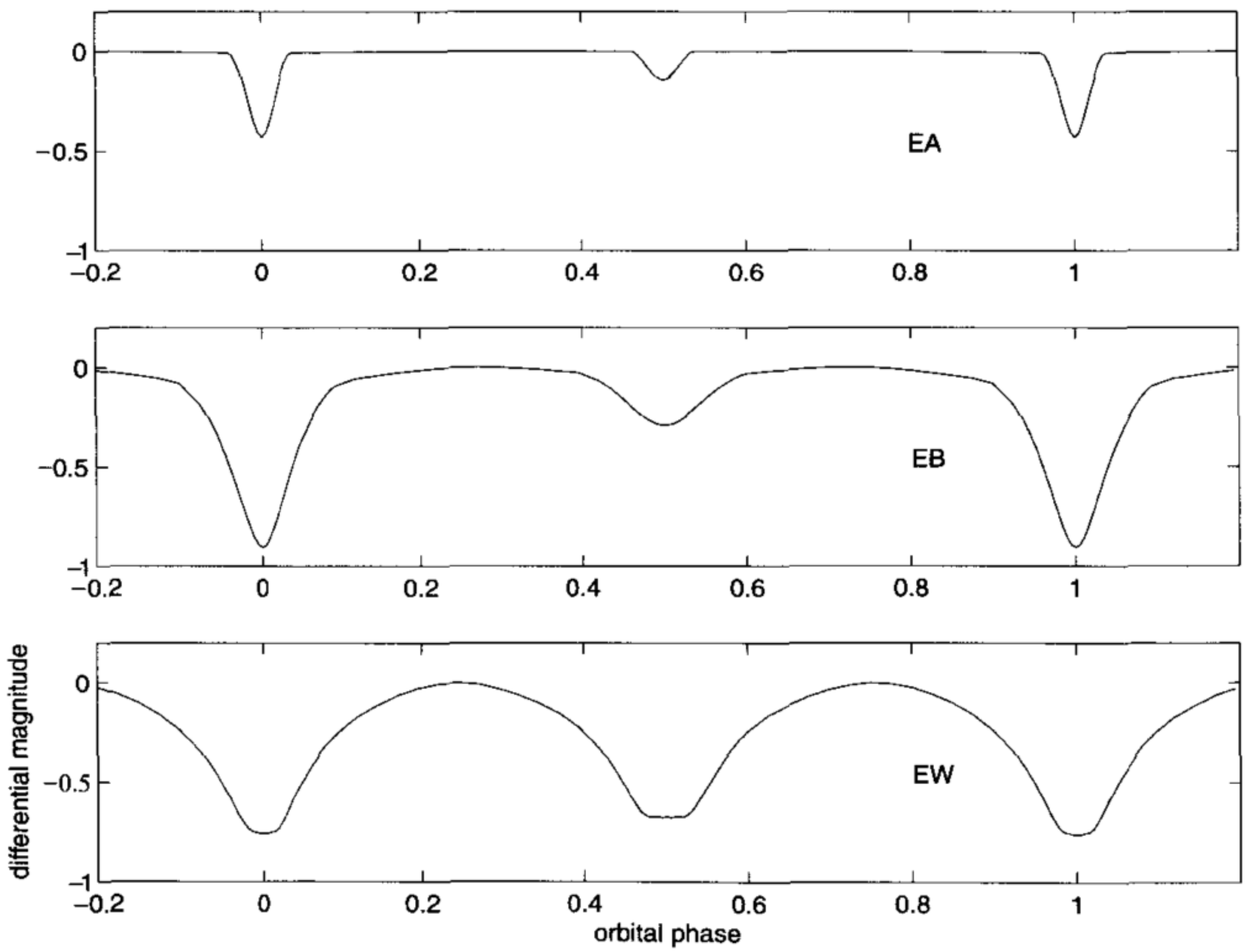

Figure 2.4.1: Extracted from Hilditch (2001): Illustrative examples of the three types (EA, EB, EW) of light curves of eclipsing binaries used for classification in the General Catalogue of Variable Stars. The range of amplitudes for light curves in each class is considerable, dependent principally upon the orbital inclination, the relative sizes of the two stars, and their ratio of surface brightnesses.

plane. This phenomenon is known as apsidal motion. One observable consequence of apsidal motion is that the position of the secondary eclipse shifts over time (see Fig. 4.1.4).

Heartbeat: In eccentric binary systems, the gravitational interaction between the two stars varies significantly throughout their orbit, particularly when they reach periastron (the point of closest approach). At this stage, strong tidal forces can induce dynamic distortions in the stars, causing them to briefly deviate from their equilibrium shapes. These distortions lead to periodic variations in brightness that are observable in the light curve as smooth, small increases in luminosity occurring just before or after the primary eclipse. This distinctive feature is known as a heartbeat variation, named for its resemblance to an electrocardiogram signal (see Fig. C.1.1). The presence of a heartbeat signal in the light curve serves as a strong indicator of orbital eccentricity, particularly in cases where a secondary eclipse is absent or difficult to detect.

Heartbeat stars were first identified in Kepler data (Thompson et al., 2012) and have since been recognized as a valuable class of variable stars for studying tidal interactions in binary systems. Their variations arise from a combination of tidal distortions, dynamical oscillations, and, in some cases, relativistic effects. A comprehensive review of their properties and classification is provided by Kumar et al. (1995) and Fuller (2017).

Chapter 3

Methodology

Our study's approach integrates a thorough search and analysis methodology to identify and evaluate candidates for detailed investigation. The candidate selection process began with an extensive literature review and database search, identifying an initial pool of 339 systems. These were compiled from various catalogs that cover spectroscopic binaries, eclipsing binaries, or massive stars, such as the Spectroscopic Binary Orbits Ninth Catalog, the OWN survey, the IACOB project, and MONOS. Given the critical role of precise photometric observations in binary modelling, we filtered this sample by identifying systems with available TESS or Kepler data, reducing the number to 186. A rapid visual inspection of their light curves allowed us to exclude clear EB/EW-type binaries, resulting in a final subset of 87 candidates suitable for detailed analysis.

To ensure high-quality light curves, we developed a custom extraction pipeline using Lightkurve, a flexible Python-based tool for TESS data processing. The pipeline incorporated adaptive aperture selection, optimized background subtraction using Gaia DR3-based stellar masking, and Phase-Synchronized Polynomial Fitting (PSPF) to correct for systematic flux variations caused by instrumental trends. Special attention was given to data validation, comparing our extracted light curves with standard TESS pipeline products (SPOC and QLP) to ensure accuracy.

For determining orbital parameters, we employed a multi-step approach. The first stage involved estimating orbital periods using Gaussian Fitting (GF) and Box Least Squares (BLS), which provided initial period determinations. These were further refined using Phase Dispersion Minimization (PDM) to enhance the precision of the orbital solutions. Further analysis of the LCs involved meticulous visual inspection to confirm the detached nature of systems exhibiting complex behavior, such as apsidal motion or heartbeat variations.

To refine and validate spectral classifications, we conducted new spectroscopic observations using the Jorge Sahade telescope at CASLEO. These low-resolution spectra, obtained with the REOSC spectrograph, provided independent verification of spectral types and luminosity classes for selected candidates to provide new spectral classification or clarify any existing uncertainties. The classification process followed established MK spectral classification criteria, comparing key diagnostic line ratios for O- and B-type stars. This ensured that the final YMDB catalog consisted of well-characterized detached binaries with accurately determined spectral properties

Finally, this chapter provides insight into the modelling of light curves using PHOEBE2. It's the YMDB catalog primary objective is to serve as a reference framework for future parameter absolute parameter determination studies. A key component of such work is the application of light curve modelling techniques, which, when combined with radial velocity solutions, enable precise derivations of stellar masses, radii, and other fundamental parameters. In this chapter, PHOEBE has been discussed in the context of specific case studies, such as WR21a (Barbá et al., 2022, detailed in Appendix B.1) and KU Car (Martín-Ravelo et al., 2021), demonstrating both the capabilities and limitations of different modelling approaches.

3.1 Sample Selection

Candidates for the study were identified through extensive searches in various databases and literature. These sources included the Spectroscopic Binary Orbits Ninth Catalog (Pourbaix et al., 2004), OWN Survey (Gamen et al., 2007, 2008; Barbá et al., 2017), IACOB (Simón-Díaz et al., 2011), Eclipsing Variables Catalog (Avvakumova et al., 2013), and the multiplicity of northern O-type spectroscopic systems project (MONOS; Maíz Apellániz et al., 2019b; Trigueros Páez et al., 2021), among others. Additionally, potential targets suggested by collaborative efforts within the astronomical community were also considered.

The search criteria encompassed a wide range, including systems with components in the O7–B3 III–V spectral class, to account for potential misclassifications. This cautious approach was used to ensure all potentially relevant systems were considered, particularly those that might align with the desired O9-B1 IV-V classification upon closer scrutiny. A thorough review of the bibliography was conducted to assess the reliability of the spectral classifications, the availability of LCs, and the reported detachment status in the literature, narrowing down the original list of 339 targets to 186 candidates.

The process continued with an analysis of TESS data to eliminate any candidates showing clear non-Algol type variability (i.e, Beta Lyræ and W Ursæ Majoris) reducing the number to 87 candidates. A custom pipeline was then developed for extracting high quality TESS LCs, allowing for the estimation of orbital periods (P) and minima (T0), as well as the identification of eccentric orbits, heartbeats and apsidal motion throughout the TESS sectors. This was achieved using both GF and BLS methods. The candidates were meticulously scrutinized, focusing on the identification of Algol-type variables. Systems not fitting the Algol type criteria were excluded, resulting in 87 stars qualifying as potential candidates which we present in this work. Details of this task are given in the following.

3.2 TESS Light Curve Analysis

The Transiting Exoplanet Survey Satellite (TESS) is a space-based mission designed primarily for exoplanet detection through high-precision photometry. However, its wide-field coverage and continuous monitoring capabilities make it an invaluable resource for stellar variability studies, including eclipsing binaries, pulsating stars, and other transient phenomena. TESS observes the sky in 27-day sectors, providing high-cadence (2-minute and 20-second for selected targets, 30-minute full-frame images for all stars) photometry over multiple years. This large-scale, nearly all-sky survey enables the discovery and characterization of a wide range of stellar variability, including eclipsing binary systems suitable for the precise determination of absolute stellar parameters.

TESS uses a broad-band red-optical filter (600–1000 nm; Fig 3.2.1), with a peak sensitivity in the near-infrared, optimized for detecting exoplanets around cool, nearby stars. The instrument delivers a typical photometric precision of a few hundred parts per million (ppm) for bright sources, with a saturation limit around 6th–7th magnitude and detection capabilities extending down to $\sim$16th magnitude depending on crowding and exposure time. However, TESS was not specifically designed to target high-mass stars; as such, many early-type systems of interest fall near the galactic plane or in crowded fields, introducing additional challenges. One key issue is the instrument's large pixel scale of approximately 21 arcseconds, which can lead to significant blending in dense regions and complicates the estimation of third light contributions. This, in turn, affects the observed eclipse depth and the accuracy of light curve modeling. To address this, we employed a combination of visual inspections, Gaia-based contamination checks, and custom aperture masks to mitigate background contributions and isolate the target system. Despite these limitations, TESS remains a powerful tool for identifying and characterizing massive detached binaries, thanks to its continuous and homogeneous photometric coverage.

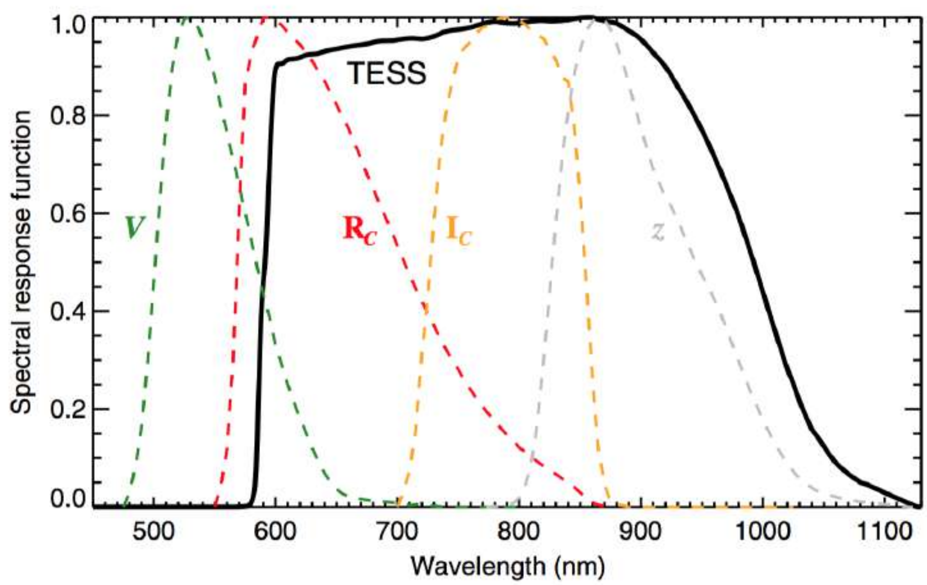

Figure 3.2.1: Spectral response of TESS (black curve), computed as the product of the long-pass filter transmission and the detector's quantum efficiency. For reference, the response functions of the Johnson-Cousins V, R_C, and I_C filters, along with the SDSS z-band filter, are also shown. All curves are normalized to a peak value of one. Image from Ricker et al. (2015).

While TESS provides reduced LCs for some targets, a significant portion of the dataset consists of raw

Full-Frame Images (FFIs), requiring independent extraction of LCs for sources of interest. The official Science Processing Operations Center (SPOC) pipeline (Jenkins et al., 2016) produces Presearch Data Conditioning (PDC) LCs for pre-selected targets, removing known systematics such as scattered light contamination and instrumental drifts. Additionally, the Quick Look Pipeline (QLP; Huang et al., 2020) provides extracted light curves for bright stars (Tmag < 13.5), but both pipelines operate as "black boxes," where the details of their applied corrections and aperture selections are not always fully transparent. While these pipelines offer high-quality light curves for many objects, they are limited to a subset of well-behaved stars, and their default aperture masks may not always be optimal for the targets of interest, particularly for crowded or complex stellar environments.

To ensure the most precise and reliable light curves possible for our selected sample, we developed a custom pipeline using LIGHTKURVE (Lightkurve Collaboration et al., 2018), a Python package that provides flexible tools for extracting and analyzing TESS light curves. This pipeline allows for fine control over aperture selection, background subtraction, and detrending techniques, optimizing light curve extraction for the needs of our study. By implementing this approach, we mitigate the risk of systematic effects that may be present in the standard pipeline products while maximizing the quality of extracted stellar photometry.

To validate our pipeline, we compare its output to both the SPOC/QLP processed light curves and raw extractions from FFIs using Lightkurve's built-in tools. For well-behaved stars with minimal contamination and stable flux variations, our pipeline produces results that are consistent with the official reductions. Figure 3.2.2 shows an example of such stars, where our extracted light curve closely matches the SPOC PDC light curve, demonstrating that our method is robust and reliable when compared to established pipelines and can be safely used for stars where no other pipeline lightcurve is available.

However, in some cases, official pipelines show artifacts in the extracted light curves due to factors such as contamination from nearby sources, suboptimal background subtraction, or aperture selection that does not fully capture the target's flux. Figure 3.2.3 illustrates an example where the SPOC/QLP pipeline's aperture choice and background subtraction introduce systematic variations in the light curve, which may require additional polynomial normalization to correct. Given the intrinsic variability of the system, such corrections can be complex and may risk altering astrophysical signals. In contrast, our custom approach effectively minimizes these artifacts, preserving the integrity of the light curve and reducing the potential loss of information. This highlights the importance of tailored reduction methods for systems where standard pipelines may not be optimized for complex stellar fields or highly variable targets.

By implementing a customized extraction process, we ensure that our light curves maintain the highest level of precision, allowing for accurate variability analysis and robust determination of stellar parameters. The next sections detail the specific steps involved in constructing these light curves, including background subtraction, target aperture selection, ephemeris determination, and systematic correction techniques.

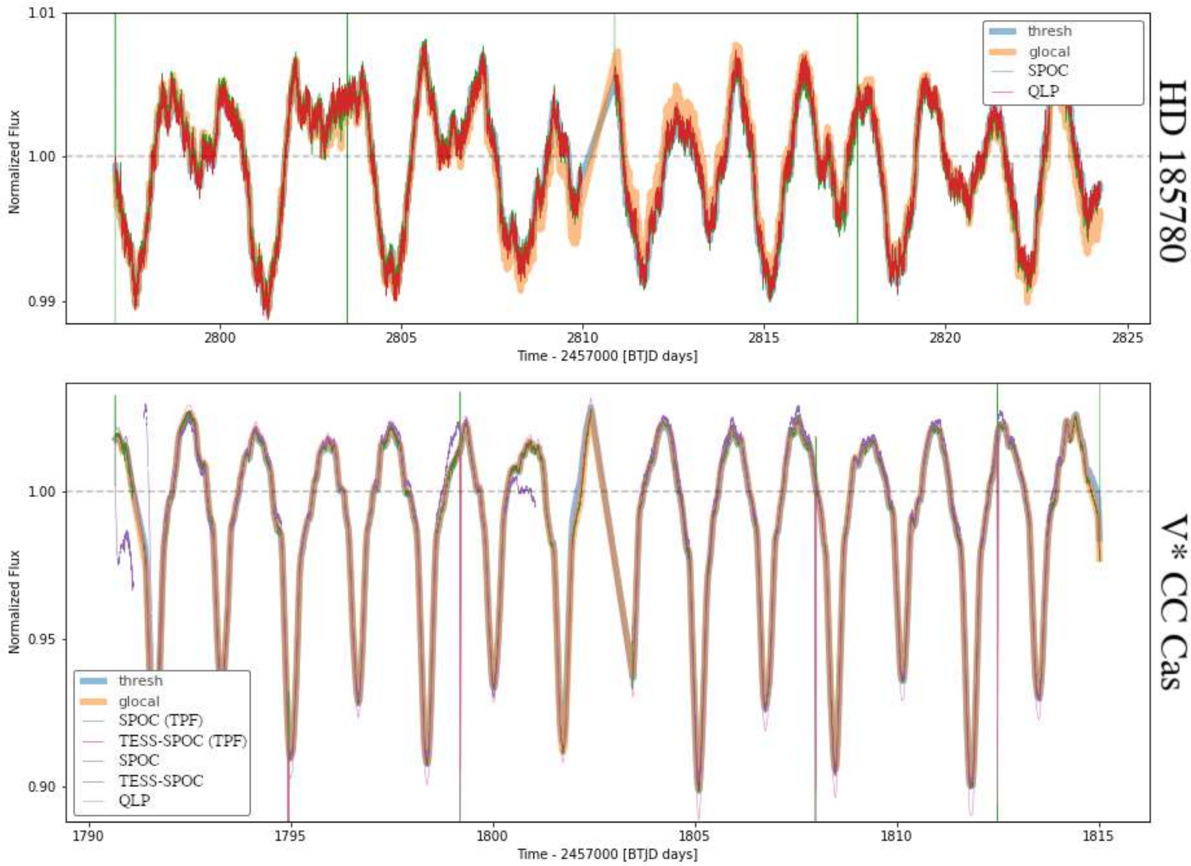

Figure 3.2.2: Comparison of light curves extracted using our custom pipeline (blue: automatic mask selection; orange: supervised mask selection) and the standard TESS pipelines (SPOC and QLP). The top panel corresponds to HD 185780, while the bottom panel shows V* CC Cas. Our extracted light curves closely match those from the official pipelines, demonstrating the reliability of our method, particularly for stars without available TESS pipeline light curves. A slight difference in magnitude depth is observed across different pipelines, which arises due to variations in pixel mask selection. Different pipelines include different pixels in their aperture masks, leading to varying levels of third-light contamination, as these additional sources are not always corrected for in the extracted light curves

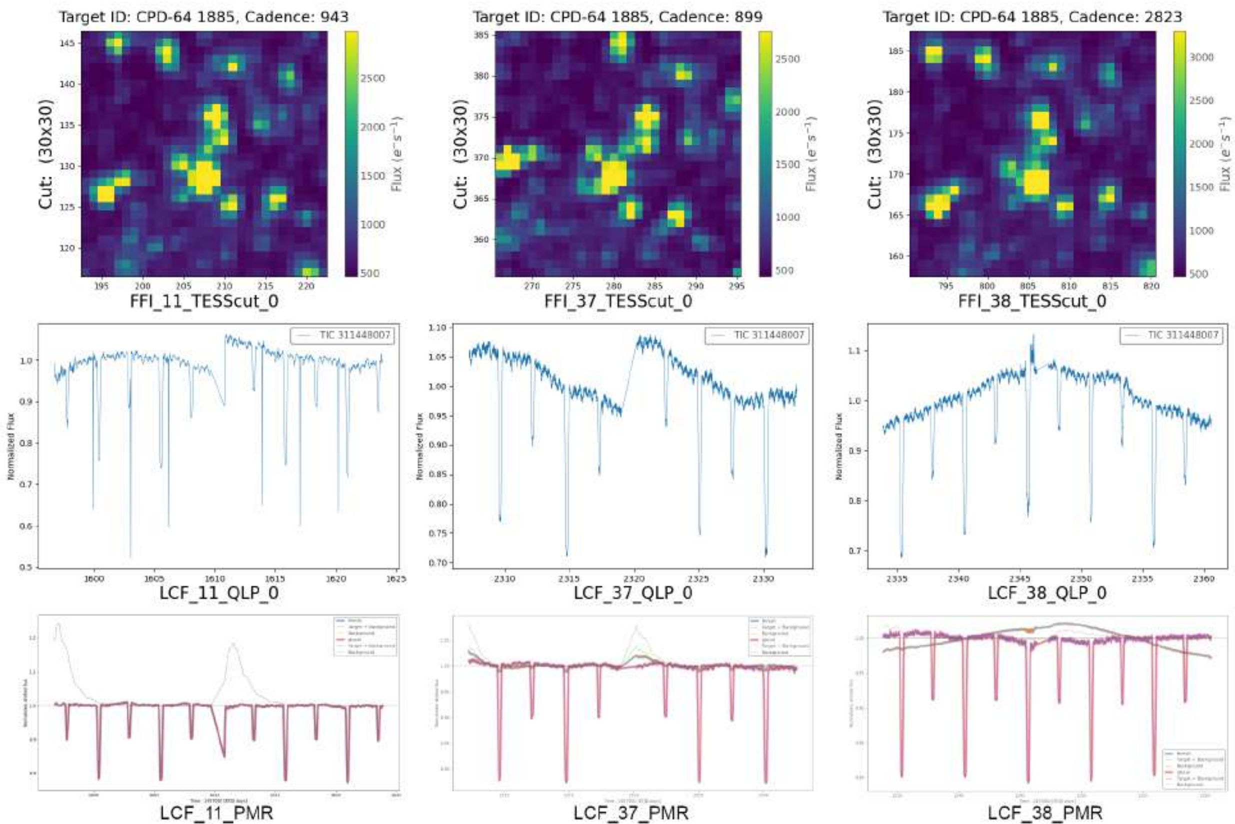

Figure 3.2.3: Light curve extraction comparison for CPD-64 1885, a system located in a crowded field with bright nearby stars. The figure consists of nine panels arranged in three columns and three rows. Each column corresponds to a different TESS sector (11, 37, and 38). The first row presents a 30×30 pixel cutout of the FFI, illustrating the stellar environment and potential contamination from nearby sources. The second row shows the light curves extracted by the QLP, where systematic trends and spurious variations are visible, likely due to suboptimal aperture and background selection. The third row displays the light curves extracted using our custom pipeline, demonstrating a significant reduction in systematic variations by employing optimized target and background masks. This comparison highlights the importance of proper mask selection in minimizing contamination and preserving the astrophysical signal, particularly in dense stellar fields.

3.2.1 Construction of Light Curves

3.2.1.1 Quality mask

In constructing the light curve, the first step involved evaluating the TESS quality masks for each sector to determine whether the default rejection criteria were appropriate for the target star. The TESS pipeline automatically flags potentially problematic cadences due to factors such as scattered light, cosmic rays, momentum dumps, and data downlinks. These flagged data points are often excluded by default to improve data reliability. TESS provides several levels of quality masking through a parameter called `quality_bitmask`. The available levels are: **default**, which excludes only cadences with severe quality issues; **hard**, which applies a more conservative filter and may remove valid data; and **hardest**, which excludes all flagged cadences and is generally not recommended (TESS Science Processing Operations Center (SPOC), 2020).

For the majority of light curves, the standard quality mask provided by TESS was found to be effective in removing spurious signals while preserving astrophysical variability. However, in some cases, the automatic rejection criteria filtered out scientifically relevant features, such as eclipses or transit events, which are crucial for identifying and characterizing detached eclipsing binaries. This issue was particularly evident in long-period systems, where eclipses occur less frequently, and rejecting flagged cadences without further review could lead to missed detections or incomplete phase coverage. Additionally, in some systems exhibiting apsidal motion, retaining flagged data proved useful for tracking subtle shifts in eclipse timing.

To ensure that no astrophysical signals were inadvertently discarded, the quality mask for each system was visually inspected and, when necessary, adjusted manually. This allowed for the recovery of valuable data points while maintaining the integrity of the extracted light curves. As shown in 3.2.4 the eclipses may occur around the sector readout, causing the default quality mask to flag these data points for removal. Such cases emphasize the importance of assessing the impact of automatic flagging before discarding data, especially in systems exhibiting apsidal motion or for long-period systems where flagged events may contain crucial, unrecoverable information.

It is important to note that while the lightkurve quality mask review provided an initial safeguard against excessive data loss, a more detailed evaluation of data reliability was conducted (Section 3.2.1.3) to ensure that instrumental artifacts or systematic errors did not compromise the quality of the final LCs.

3.2.1.2 Background and target masks

To accurately extract light curves from TESS FFIs, it is essential to carefully define the pixels included in the photometric aperture while mitigating contamination from nearby sources. This is achieved through a two-step masking process: (i) constructing a background mask to exclude contaminating sources and (ii) defining a target mask to optimally capture the flux from the star of interest.

- **Background mask:** To construct a sky background mask for each sector, a 30×30 pixel area

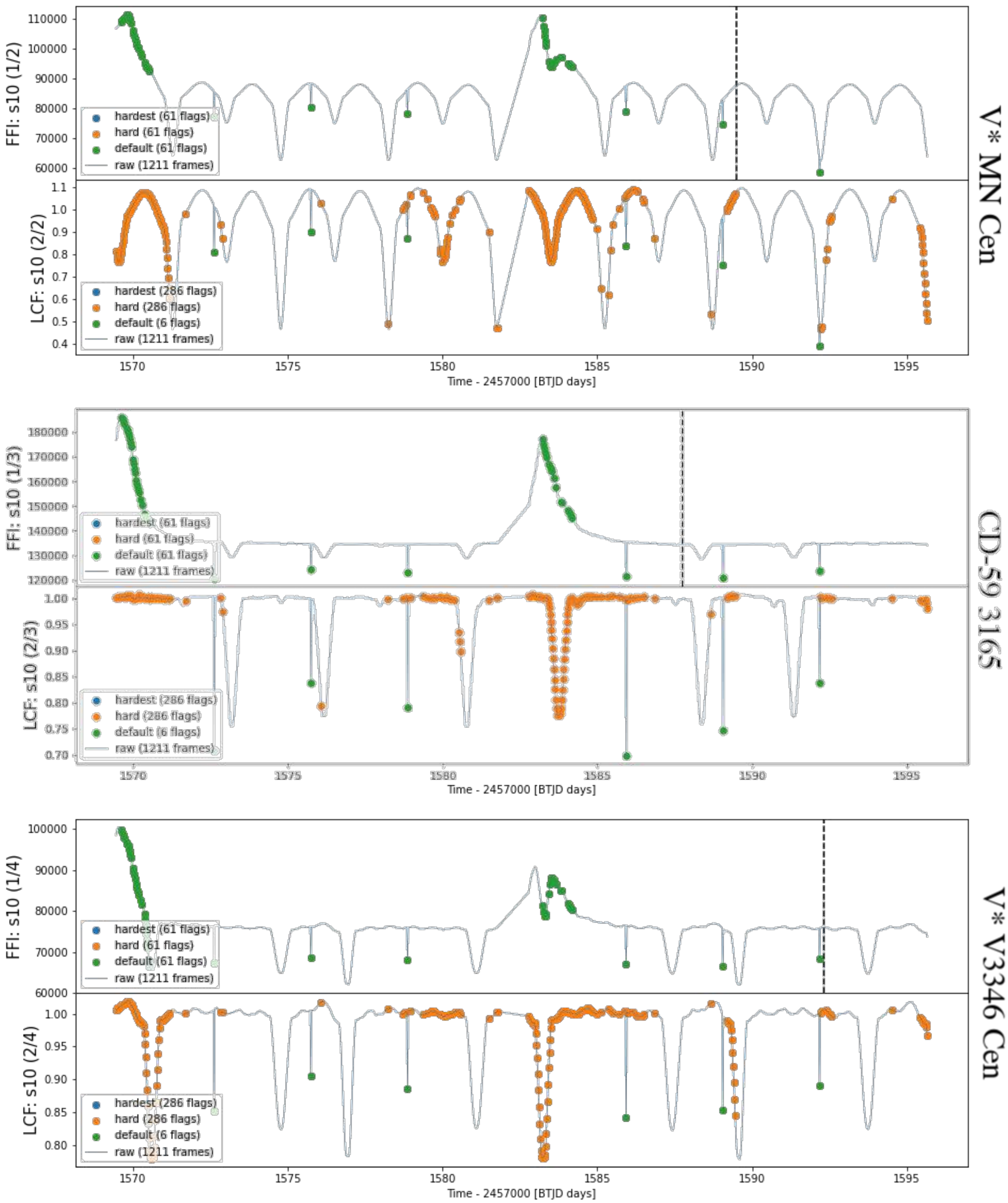

Figure 3.2.4: Example of three systems (V* MN Cen, CD-59 3165, and V* V3346 Cen) where the default TESS quality mask flagged an eclipse event, leading to its exclusion from the processed LC. Each system is presented in two subpanels: the top subpanel shows the raw flux extracted from FFIs, while the bottom subpanel shows the corresponding TESS pipeline LC. In all cases, the eclipses occur immediately after the sector readout, causing the default quality mask to flag these data points for removal. Green, orange, and blue points indicate the TESS-defined quality mask levels: default, hard, and hardest, respectively.

centered on the target system is analyzed. Stars within this area, along with their magnitudes, are identified using Gaia DR3 data. The LIGHTKURVE tool is then employed to generate a mask with threshold zero, specifically excluding pixels affected by stars brighter than a determined magnitude limit. This upper limit is set at 5 magnitudes fainter than the brightest star within a custom radius of the target system. The exclusion zone for each contaminating source is not fixed but scales with magnitude, following:

$$r_{\mathrm{excl}} = (m_0 - m) \times C \tag{3.2.1}$$

where m is the apparent magnitude of the contaminating star, m_0 is the reference magnitude, and C is the scaling factor that defines how the mask grows for brighter stars. The function of the pipeline is adjustable but it was found that $m_0 = 12$ and $C = 1$ gives a very reliable approach, although others may find different values more suitable for their targets. To ensure proper contamination control, a minimum exclusion radius of 0.25 pixels is enforced even for faint stars. This dynamic approach allows us to efficiently minimizes contamination from nearby stars while preserving as much target flux as possible, optimizing the extracted light curve.

- **Target mask:** Following the construction of the sky background mask, a target mask is developed using a similar methodology. The function that delineates boxes around mapped stars based on their brightness is also applied to isolate the Target Pixel File (TPF) surrounding the star of interest. Adjustments to the size and position of this cut, alongside a specified threshold value, are made using the LIGHTKURVE tool to craft the target mask. This stage might require iteration, involving comparisons of the resulting LC with published ones and the LCs of individual pixels, to verify the accuracy of the selected parameters and the suitability of the target mask.

A final visualization of the mask selection process is shown in Figure 3.2.5, where background pixels are marked in white, nearby field stars are highlighted in red, and the selected target mask pixels are shown in blue.

3.2.1.3 Data Selection

The analysis of the unfolded extracted LC involves identifying and flagging problematic data that could compromise the construction of the LC. A visual inspection of the cadence for each TESS sector is essential as it can reveal areas potentially affected by gaps in data—either due to TESS CCD readouts or data omitted by the quality mask. Data adjacent to these gaps might exhibit a different background profile, making parts of the LC unreliable if the background extraction fails to account for this variance. Additionally, these segments may experience slight magnitude shifts (Δmag) and may require independent normalization, posing challenges for systems with long periods. In some cases, these systematic errors can be misleading and resemble astrophysical variability. Figure 3.2.6 illustrates an example where a cadence-related anomaly appears as a deep eclipse-like event. Without proper verification, such artifacts could be misinterpreted as genuine astrophysical signals, emphasizing the importance of thorough data selection.

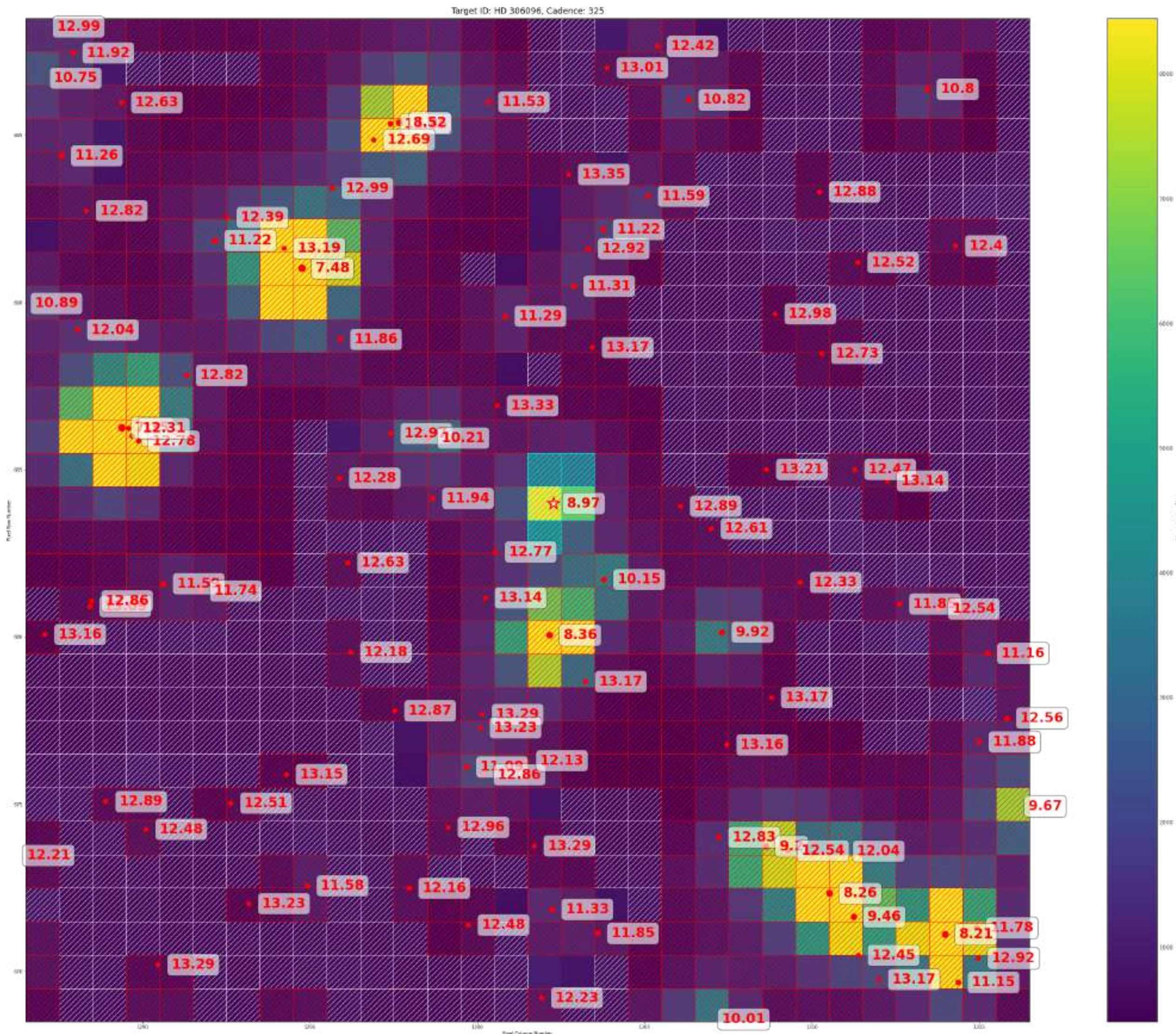

Figure 3.2.5: Illustration of the mask selection process for a TESS FFI. The background mask (white) excludes sky pixels, while the target mask (blue) selects the pixels used for photometry. Field stars detected using Gaia DR3 with the brightness threshold applied are marked in red and excluded from the background mask to minimize contamination. The inset panel highlights the final Target Pixel File (TPF) aperture around the star.

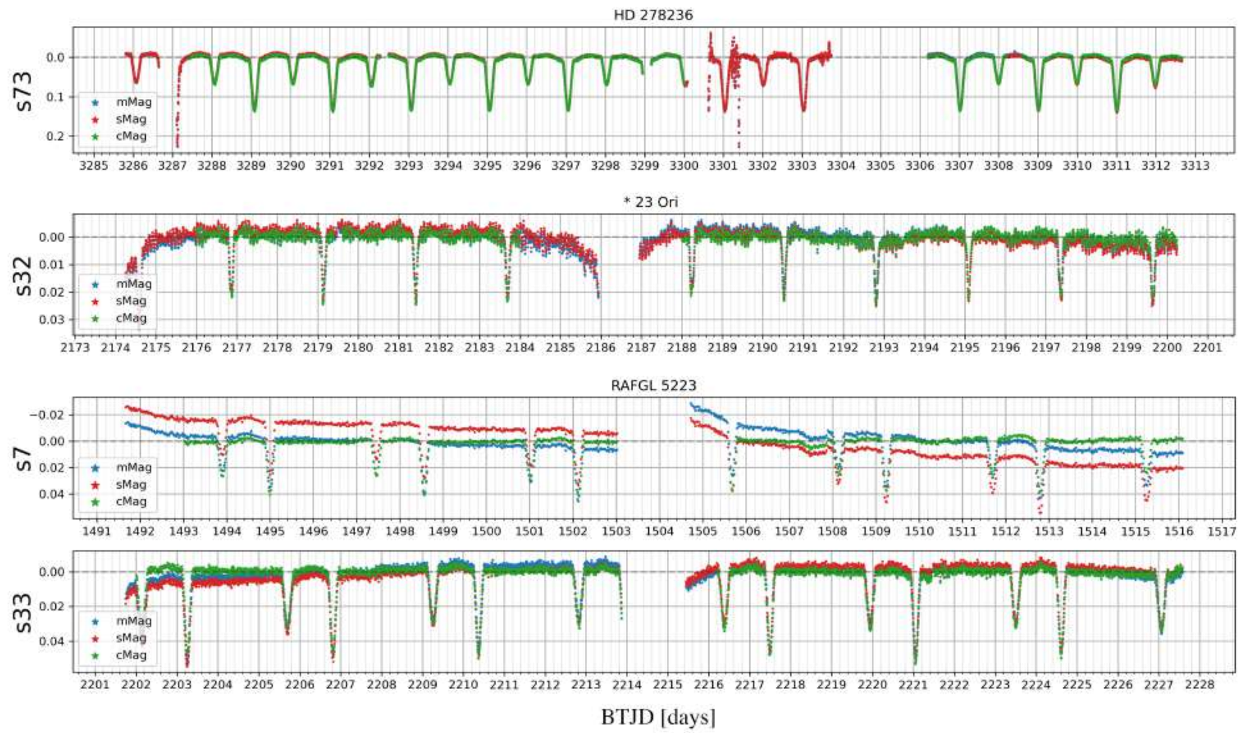

Figure 3.2.6: Light curves for HD 278236, *23 Ori, and RAFGL 5223 across different problematic sectors, where only the affected sectors are displayed. Each subplot represents a different sector (s73, s32, s7, s33) for the corresponding star. Systematic artifacts are evident at the beginning and middle of each sector, particularly near readout gaps, where discontinuities introduce spurious trends that differ from the expected astrophysical variability. These trends are difficult to model and, in some cases, are best excluded from analysis. The red points (sMag) show the light curve normalized to the entire sector, while the blue points (mMag) represent the same data normalized within individual data segments separated by significant gaps. The green points (cMag) indicate the data selected for phase-folded analysis after correction for systematic artifacts using the Phase-Synchronized Polynomial Fitting method (see Section 3.2.1.5). This approach mitigates contamination effects and preserves the integrity of astrophysical signals

While we strive to preserve as much observational data as possible, maintaining the accuracy of the light curve is the highest priority. Problematic segments that introduce unrecoverable systematics are flagged and removed, ensuring that only reliable photometric data contribute to the final analysis.

3.2.1.4 Ephemeris determination

In determining the ephemeris of our studied systems, we incorporate two principal methods: GF and BLS. GF is primarily utilized for its simplicity and effectiveness in identifying eclipse minima by fitting Gaussian profiles. First, eclipses are visually identified in the light curve (Figure 3.2.7), and Gaussian functions are fitted to these minima to estimate their exact timings (Figure 3.2.7). From these fits, we derive an initial estimate of the period by measuring the separation between successive eclipses. The distribution of period values obtained through this method is shown in Figure 3.2.7.

To verify and complement these estimates, we apply the BLS method, which is particularly useful for detecting periodic signals in unevenly spaced or noisy datasets. The BLS-derived frequency spectrum highlights the most significant periodicities in the data (Figure 3.2.8), providing an independent check on the GF results. When possible, we cross-reference these period estimates with values from the literature to ensure consistency.

Once a robust initial period estimate is obtained, we refine the measurement using PDM. This method minimizes scatter across phased data to detect stable periodic signals, making it particularly well-suited for TESS data, which may contain observational gaps or non-sinusoidal variations. PDM is applied by analyzing the period space around the estimates provided by GF/BLS, ultimately selecting the most likely period. The effectiveness of this refinement is demonstrated in Figure 3.2.9, where a comparison of the folded light curves using the preliminary estimate and the final PDM-refined period shows improved coherence and phase alignment.

3.2.1.5 Phase-synchronized polynomial fitting

Photometric observations from the TESS mission, similar to those from its predecessor Kepler, are susceptible to instrumental systematic trends that can obscure or distort the intrinsic stellar signals. These systematics arise primarily from spacecraft jitter and other operational imperfections, which introduce noise and trends across different timescales into the captured LCs.

To mitigate these effects, we employed a polynomial fitting method, analogous to the Pixel Level Decorrelation (PLD) method utilized in the EVEREST pipeline for K2 data. This method has been demonstrated to effectively remove correlated noise due to spacecraft motion by fitting and subtracting systematics directly from the pixel-level data (Luger et al., 2016).

While our approach uses a simpler polynomial fitting of lower orders, it shares the core principle of modelling the observed data to isolate and remove instrumental signatures. The primary distinction of our method, which we designate as "Phase-Synchronized Polynomial Fitting" (PSPF), lies in its utilization of the previously known orbital periods to synchronize (fold) phase points within a TESS sector. This

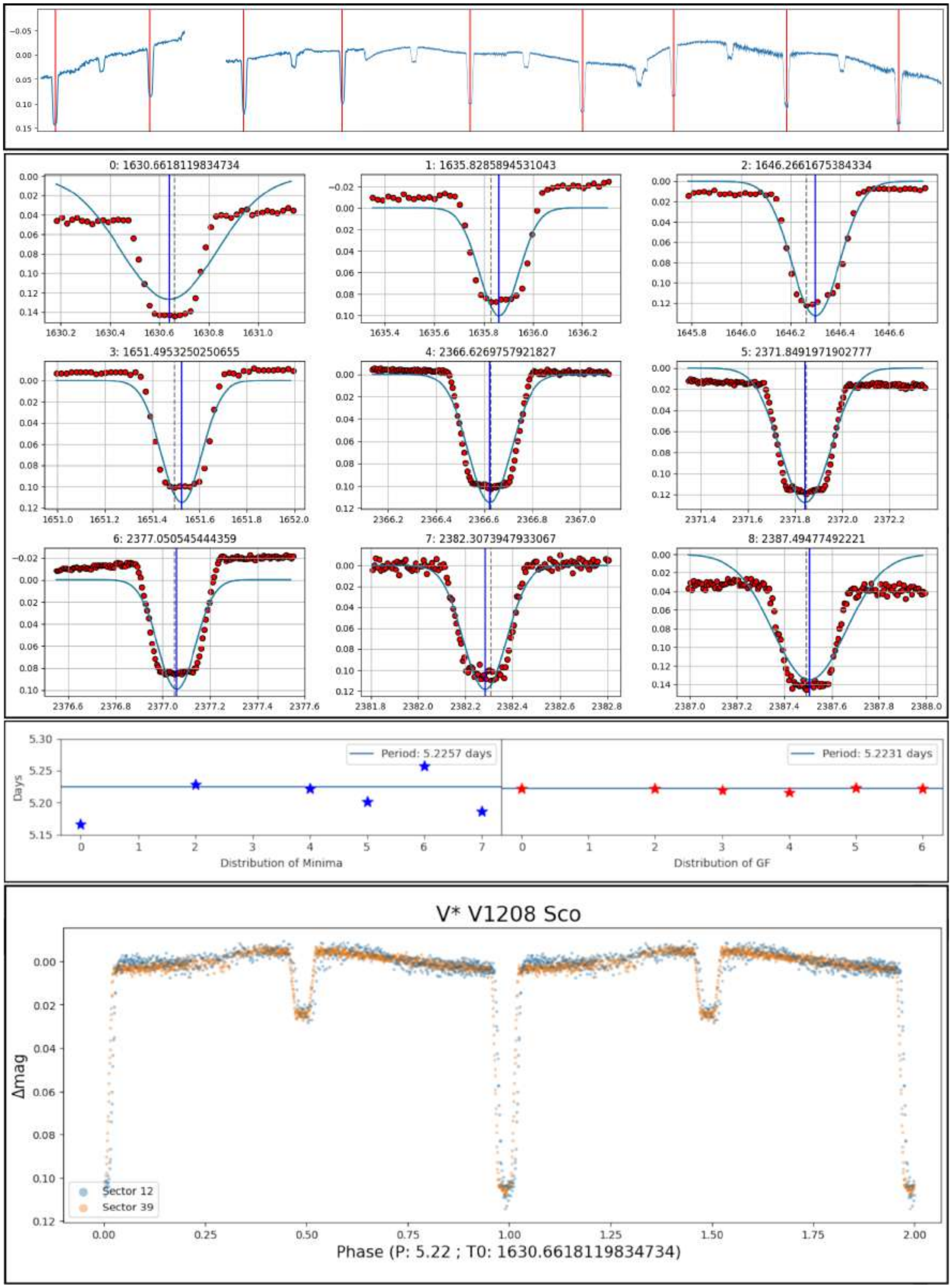

Figure 3.2.7: Identification and period estimation using GF for the eclipsing binary V* V1208 Sco. From top to bottom: (1) Identification of eclipses in the LC, with marked red vertical lines indicating detected minima. (2) GF applied to individual minima, refining a preliminary period determination. (3) Distribution of eclipse separation obtained from minima (blue) and GF centroids (red). (4) Phase-folded LC using the determined period.

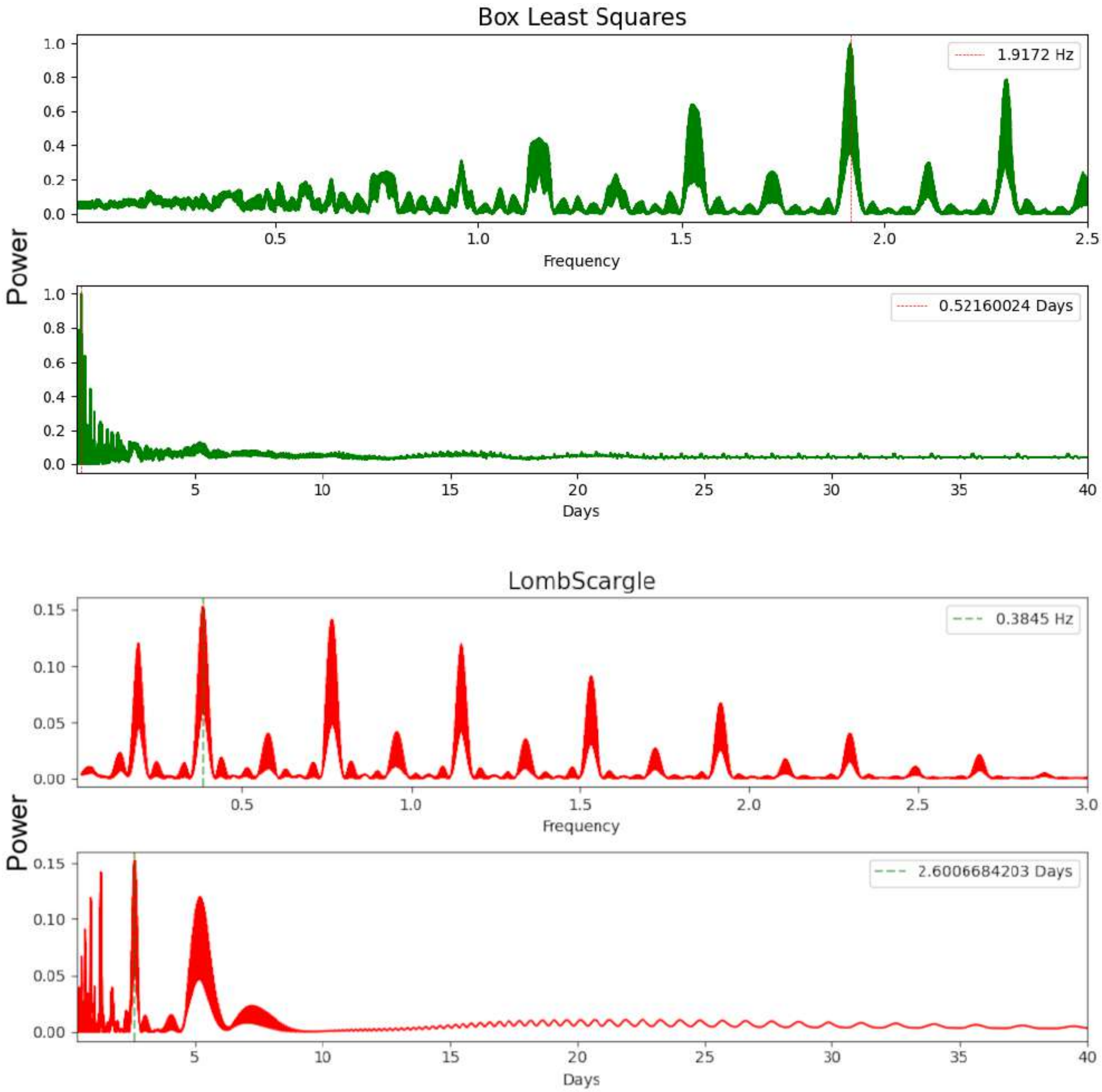

Figure 3.2.8: Frequency analysis of V* V1208 Sco using the BLS and Lomb-Scargle methods. The top two rows correspond to the BLS method, while the bottom two rows correspond to the Lomb-Scargle periodogram. For each method, the top panel shows the power spectrum as a function of frequency, while the bottom panel presents power as a function of period (in days). The BLS method identifies a dominant periodicity at approximately 1/10 of the expected period, while the Lomb-Scargle method peaks at half the actual period.

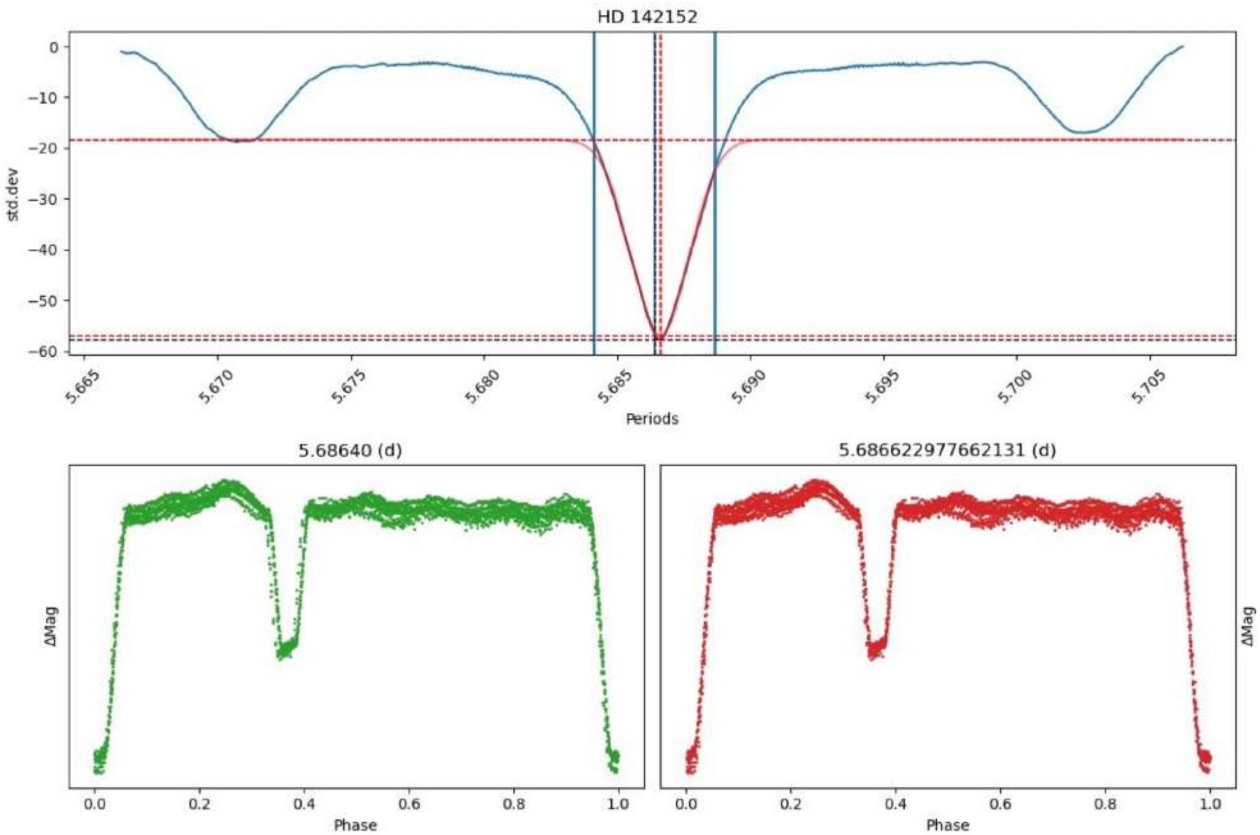

Figure 3.2.9: Period refinement using PDM for HD 142152. The top panel shows the PDM spectrum, where the initial period obtained from GF is marked by the black vertical line at 5.68640 d, while the refined period from PDM is indicated by the dashed red vertical line at 5.68663 d. This small period adjustment ensures better alignment of the secondary eclipse, avoiding the misclassification of the system as one exhibiting apsidal motion. The bottom panels display the phase-folded LCs: the left panel (green) corresponds to the GF period, while the right panel (red) uses the PDM-refined period, illustrating the improved phase alignment.

synchronization enables the calculation of fits for data points that share the same phase, thus forming a more complex function that better adapts to the unique signal trends of TESS data. Therefore, PSPF is suited for systems with orbital periods shorter than the duration of a TESS sector. The method cannot be applied if the period exceeds the sector length (PLD should be used in those cases), unless the signal is expected to remain constant in different phases of the LC, such as outside the eclipses in highly detached binaries. It becomes particularly reliable when the orbital period is substantially shorter than the sector length, allowing for enhanced signal integrity post-correction through multiple phase folds.

The correction process begins with the identification of phase points across the LC that are consistent over multiple orbits, meaning without flux variations other than those related to the eclipsing nature of the system or other synchronized pulsations (whose periods are multiple of the orbital period). This leverages the comparative stability of shorter-period systems which may ignore not-synchronized variations if enough points per phase are provided. Each phase point will provide then a value not only for that phase, but for every other phase point in the LC. A weighted mean is calculated for these values in each phase point to construct a robust fit model. This model is then used to adjust the LC, with the median of all polynomial corrections applied to derive the final corrected LC. This procedure was only implemented when a consistent pattern of systematic error was evident across the entire sector, ensuring that the corrections made were both meaningful and substantiated by the data. Figure 3.2.10 shows the correction process applied to a representative system, illustrating the effectiveness of our PSPF approach.

For about 20% of the candidates in our study that exhibited clear systematic trends, the PSPF was crucial for assembling a clean LC. A polynomial fit of order 1 was mainly used, but the selection of polynomial order was tailored to each target's specific noise characteristics, with higher orders only used seldom and for more complex systematic patterns.

Our PSPF corrections were validated against already corrected LCs, showing a significant reduction in noise and the preservation of intrinsic astrophysical signals and effectively detrending the TESS LCs, akin to the results reported by the EVEREST pipeline when applying PLD to K2 data (Luger et al., 2018).

3.2.2 Disentangling Light Curves in Multiple Systems

In some cases, the photometric data obtained from TESS contained contributions from multiple stellar components, making it difficult to analyze individual system behaviors directly. This was particularly challenging in systems such as CD-59 3165 (detailed in Sec. 4.1.2, Fig. 4.1.8) and BD+66 1674 and η Ori (both in Sec. 4.1.1, Figs. 4.1.2 and 4.1.3), where additional oscillatory variations were superimposed onto the primary binary signal.

To disentangle these signals without relying on full light curve modelling, we employed a phase-binned averaging approach. Since the primary binary system's orbital period was well determined, we used the ample data per phase bin to construct an average profile of the eclipsing variations, effectively producing an empirical model of the main binary signal. This model was then subtracted from the observed light curve, leaving behind the residual variations corresponding to additional system components. This technique is valid under the assumption that the additional variations are not synchronized with the primary

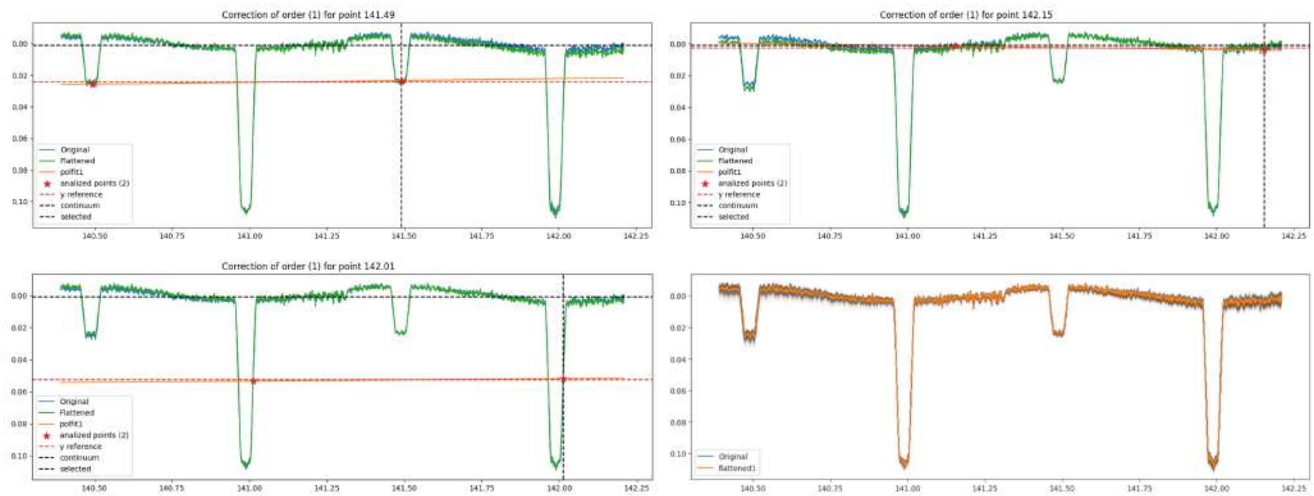

Figure 3.2.10: Illustration of the PSPF process for correcting systematic trends in V* V1208 Sco LC. PSPF operates by analyzing each data point within a margin (a continuous segment of a sector between data gaps), computing its phase, and fitting a polynomial across all points with the same phase within the margin. The top-left, top-right, and bottom-left panels demonstrate individual polynomial fits (orange lines) applied to specific phase points. The original light curve (blue) exhibits systematic trends, while the polynomial-normalized version (green) effectively removes these artifacts. Each point in the light curve accumulates multiple correction values from various polynomial fits across the dataset, and the final correction function is derived as the median correction over all fits. The bottom-right panel presents the fully corrected light curve, showcasing significantly reduced dispersion while preserving astrophysical signals. This approach ensures that corrections are only applied when systematic trends persist consistently across the entire dataset, preventing overfitting to individual points.

orbital period, allowing for a clear separation of signals.

For systems where the additional variability was phase-locked with the primary binary period or not enough coverage was available, alternative approaches were required. In the case of η Ori, for example, we applied sinusoidal fitting to account for the additional periodicity, as seen in Fig. 4.1.3. In other cases, we isolated the perturbations by removing the eclipsing variations and analyzing the residual light curve separately. This method allowed us to identify and confirm oscillations signals in 37 systems, 11 of which are unprecedented.

3.2.3 Analysis of the Light Curves

All generated LCs underwent meticulous inspection to confirm their detached nature, identify any pulsations or heartbeats, and determine eccentricity and apsidal motion. Visual inspection was used to confirm the detached nature of the system, which was unequivocally determined by the distinct transitions marking the beginning and end of eclipses in the LC. Pulsational features, indicative of either intrinsic variability of the components or the presence of a complex multiple system, were also identified through visual inspection of the LCs. In cases of multiple systems, efforts were made to disentangle the LCs using templates crafted from median data selected, when possible, from segments of the LC minimally affected by eclipses or intrinsic pulsations of the main system. The heartbeat phenomenon was identified as a distinct photometric variation occurring during orbital phases with closer eclipses, indicative of the expected periastron. We compared those variations against all forms of heartbeat reported in Thompson et al. (2012). The systems exhibiting heartbeat-like features are discussed individually in Section 4.1.

For systems where eccentricity was not immediately obvious, we employed GF to precisely measure the centers of the primary and secondary eclipses, using a threshold of $\Delta\phi$=0.0002, to determine whether their phase separation differed from 0.5. It is important to note that an exact half-period interval between eclipses does not necessarily imply a circular orbit; the system could be eccentric with a periastron longitude of either 90° or 270°. Therefore, values listed in Tables 2, 3, and 4 may imply eccentricity but never circularity. Variations in the fit to the secondary eclipse across different sectors were analyzed, and systems exhibiting changes beyond a certain threshold ($\Delta\phi$=0.0002) were flagged for potential apsidal motion. Additionally, since heartbeat phenomena occur exclusively in eccentric binaries, the detection of heartbeat signals in cases where only one eclipse was observed allowed us to identify the system as eccentric.

3.3 Spectral Analysis

To address the inconsistencies in spectral classifications found in the existing literature, we undertook the task of obtaining new spectra. Low-resolution spectra were obtained using the Jorge Sahade telescope at Complejo Astronómico El Leoncito (CASLEO) in San Juan, Argentina, utilizing the REOSC spectrograph in single mode alongside the new Sophia CCD. This equipment yielded spectra with a resolution of $R \sim 1000$, covering the wavelength range of 3760–5845 Å, suitable for spectral classification in the

MKK system. Spectral data processing was conducted in the standard way using IRAF[1] routines.

The spectroscopic classification of stars within the YMDB catalog follows the Morgan-Keenan (MK) system, as outlined in Stellar Spectral Classification by Gray & Corbally (2009). This system categorizes stars based on spectral type (which reflects temperature) and luminosity class (which correlates with surface gravity and evolutionary stage). OB stars, among the hottest and most massive, are classified primarily through helium and silicon line ratios that vary with temperature and ionization state.

For late O-type stars, the He II λ4541 to He I λ4387 ratio serves as a key temperature indicator, helping to distinguish early O from later O subtypes (Walborn & Fitzpatrick, 1990; Sota et al., 2011, 2014). For early B-type stars, the transition from O9 to B1 is primarily traced through the Si III λ4552 to Si IV λ4089 ratio, as discussed in the spectral classification updates by Sota et al. (2014).

Luminosity classification further refines this categorization, distinguishing between supergiants (I), giants (III), and main-sequence stars (V). Since the YMDB catalog focuses on young, massive detached binaries, most classified stars belong to luminosity class V (main sequence), where hydrogen burning is stable. Luminosity classes are inferred from the width and shape of helium and silicon lines, which change with surface gravity.

Figure 3.3.1 displays sample spectra from CASLEO, annotated with the most significant spectral lines used in our classification. The results of our spectral classifications are presented in section 4.1, under the ST1 column in Tables 4.1.2, 4.1.3, and 4.1.4. Spectral classifications determined in this work are marked with the “tw” label.

3.4 Modelling of Light Curves using PHOEBE2

PHOEBE (detailed in Sec. 2.3.4) is a Python-based software package designed for modelling light curves and radial velocity data of eclipsing binary systems. Originally developed as an extension of the Wilson-Devinney code, PHOEBE has evolved into a powerful framework that incorporates modern numerical techniques and detailed physical modelling of binary stars. The latest versions, particularly PHOEBE 2.x, emphasize high precision in computing observables, enabling the determination of fundamental stellar parameters with increased accuracy.

A key advantage of PHOEBE2 is its ability to incorporate a wide range of physical effects, including reflection, gravity darkening, limb darkening, and interstellar extinction, while providing a flexible framework for implementing customized solvers. Additionally, it supports multiple optimization and sampling techniques, allowing for efficient parameter refinement while ensuring consistency with observational constraints.

Although the YMDB catalog does not provide absolute parameters, one of its primary objectives is to serve as a reference for the scientific community in deriving these values (see Section 5.1.2). Throughout

[1]NOIRLab IRAF is distributed by the Community Science and Data Center at NSF NOIRLab, which is managed by the Association of Universities for Research in Astronomy (AURA) under a cooperative agreement with the U.S. National Science Foundation.

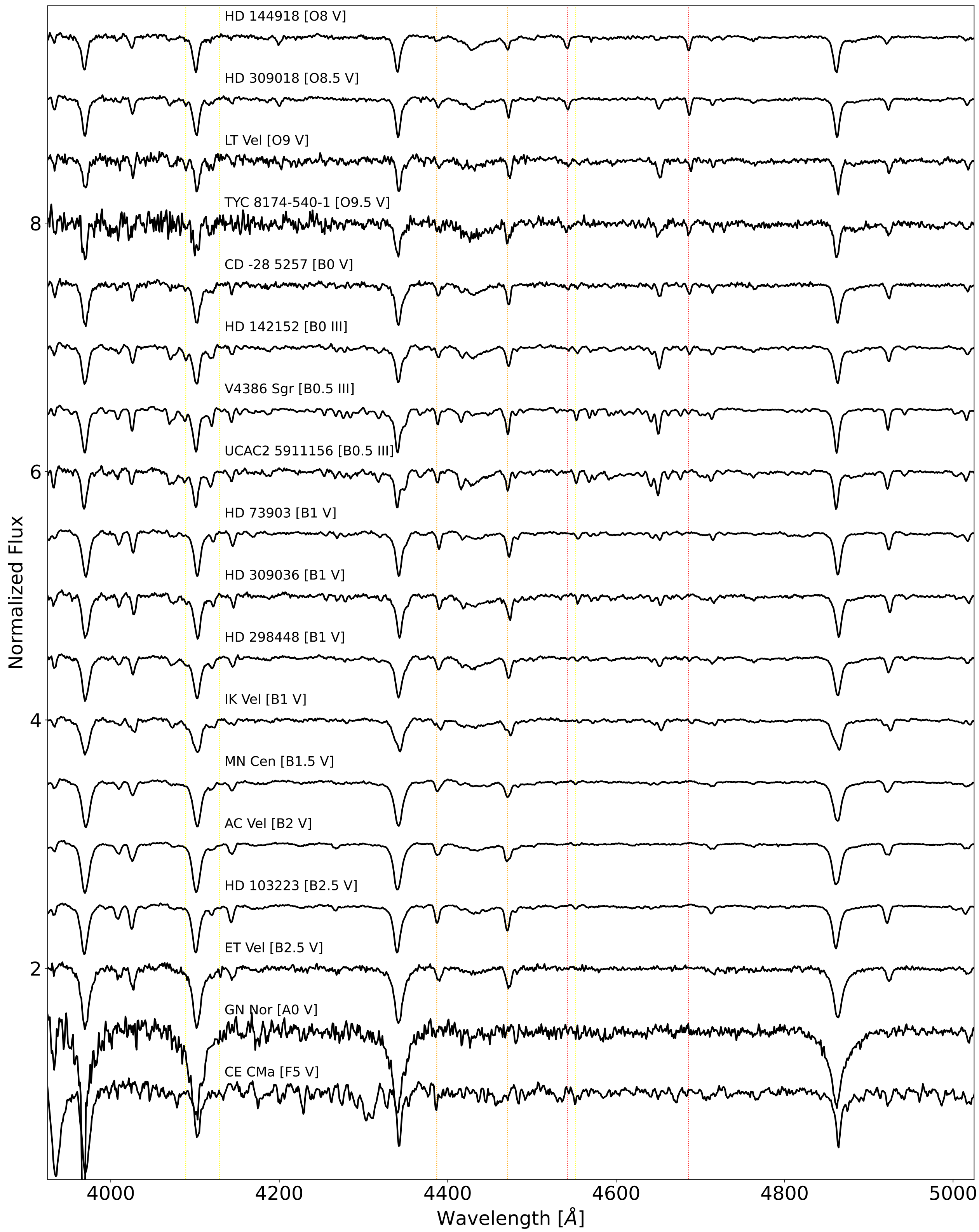

Figure 3.3.1: CASLEO spectra classified in Martín-Ravelo et al. (2024). Vertical lines indicate the most significant spectral lines used for classification: He II (red), He I (orange), and Si II–III–IV (yellow).

this thesis, PHOEBE was successfully applied to the analysis of WR21a (Barbá et al., 2022, detailed in Appendix B.1) and KU Car (Martín-Ravelo et al., 2021). However, these applications had certain limitations: in WR21a, the secondary eclipse was not observed, preventing an accurate radius determination, while in KU Car, no radial velocity constraints were incorporated.

In a standard modelling approach, absolute parameters are derived by combining orbital parameters from the RV solution with a temperature estimate based on spectral type. By incorporating these constraints into PHOEBE, the models can be further refined, leading to a more precise determination of the binary components' physical properties. This methodology is particularly important in the study of massive binary systems, where uncertainties in fundamental parameters can propagate into discrepancies in stellar evolutionary models.

3.4.1 Initial parameters and Assumptions

The modelling of binary systems begins with defining an initial set of parameters that describe the orbital and stellar properties. The most fundamental inputs are obtained through spectroscopic and photometric observations, which provide constraints on the mass ratio, orbital inclination, temperatures, and radii of the stellar components. These observational constraints serve as the starting point for light curve modelling and are refined through iterative fitting processes.

The orbital parameters, including the semi-major axis, eccentricity, and systemic velocity, are adopted from RV measurements. This ensures consistency between the spectroscopic and photometric solutions, reducing degeneracies in the modelling process. As discussed in Section A, these parameters are derived from fitting observed radial velocity curves using spectroscopic measurements. Given that PHOEBE requires both photometric and spectroscopic constraints for accurate modelling, the RV solution provides critical boundary conditions for the LC fitting, allowing us to fix or limit parameters such as orbital period, eccentricity, and argument of periastron while solving for inclination and stellar radii.

Effective Temperatures are estimated based on spectral classification, following standard calibrations from the literature. The reference Table 3.4.1 for O/B stars summarizes the typical temperature ranges for different spectral types (Pecaut & Mamajek, 2013; Martins et al., 2005). Additionally, bolometric corrections and limb-darkening coefficients are derived from theoretical stellar atmosphere models. PHOEBE2 by default adopts the Castelli & Kurucz (2004) ATLAS9 model atmospheres, which provide precomputed limb-darkening coefficients for a range of effective temperatures (3,500 K – 50,000 K), surface gravities, and metallicities. For hotter stars, PHOEBE also supports coefficients from the Claret (2000, 2004); Claret & Bloemen (2011) limb-darkening tables, extending applicability up to at least 50,000 K, making them suitable for massive stars. If available, additional constraints from evolutionary models or previous studies are incorporated to refine estimates of stellar radii and surface gravity.

The inclination is initially estimated based on eclipse depths in the light curve. However, it also has a minimum theoretical value determined by the system's semi-major axis and stellar radii—below this threshold, no eclipses would be observed. While the radii are not precisely known at the outset, they can be constrained using estimates from spectral classification and evolutionary models, allowing us to define a reasonable lower bound for the inclination. This helps optimize computational resources by avoiding

Table 3.4.1: Spectral Type – Temperature Calibration

Spectral Type	Effective Temperature [kK]
O3 – O5 V	42.0 – 48.5
O6 – O8 V	37.0 – 42.0
O9 – B0 V	30.0 – 37.0
B1 – B3 V	19.0 – 30.0
B4 – B7 V	12.5 – 19.0
B8 – A0 V	9.7 – 12.5

Note: O-type star temperatures are taken from (Martins et al., 2005), while B-type star temperatures are from (Pecaut & Mamajek, 2013).

the simulation of non-eclipsing configurations. Third-light contamination, if present, can be treated as a free parameter and can be constrained using Gaia cross-matching to identify nearby stars contributing to the flux observed by TESS.

Orbital period, eccentricity, and argument of periastron are well-constrained from RV measurements and therefore are held fixed to maintain consistency with spectroscopic solutions. The stellar masses, radii, and temperatures remain adjustable within reasonable physical bounds, allowing PHOEBE to determine the best-fit solution based on the observed light curves. To illustrate this process, Table 3.4.2 presents the initial conditions for WR21a (final solution shown in Table B.1.1), which were used as a starting point for PHOEBE modelling (Barbá et al., 2022). These parameters were derived from spectroscopic studies and evolutionary models, ensuring that the initial setup aligns with observational constraints.

These initial conditions serve as the foundation for the first-order modelling process, which aims to fit observed light curves with synthetic models while iteratively refining parameter estimates.

3.4.2 Solving the Inverse Problem

The modelling of eclipsing binary systems falls within the class of inverse problems, where the goal is to infer the physical properties of a system from indirect observational data. In this case, LCs and RV measurements provide constraints on key stellar parameters such as masses, radii, temperatures, and orbital elements. PHOEBE is specifically designed to address this inverse problem by employing numerical techniques that iteratively adjust model parameters to minimize discrepancies between observed and synthetic data. By leveraging optimization and sampling algorithms, PHOEBE enables precise determination of parameters that cannot be directly measured, such as limb-darkening coefficients, gravitational distortions, and third-light contamination.

Solving an eclipsing binary system is inherently a computationally expensive task that requires a careful balance between precision and efficiency. PHOEBE provides multiple built-in solvers, each designed to

Table 3.4.2: Initial conditions adopted for WR21a modelling.

Parameter	Value	Constrained by	Status
Orbital Period (P)	0.2	RV, LC	Fixed
Time of Superior Conjunction (T_0)	1.2	RV	Fixed
Time of Eclipse (T_0)	2.2	LC	Fixed
Eccentricity (e)	3.2	RV	Fixed
Argument of Periastron (ω)	4.2	RV	Fixed
Primary Mass (M_1)	10–20 $M_\odot$	SC	Free
Secondary Mass (M_2)	15–30 $M_\odot$	SC	Free
Primary Temperature (T_1)	10–20 kK	SC	Free
Secondary Temperature (T_2)	15–30 kK	SC	Free
Primary Relative Radius (r_1)	1.0	RV	Free
Secondary Relative Radius (r_2)	1.0	RV	Free

Note: "SC" refers to Spectral Classification constraints, while "RV" refers to Radial Velocity solutions. The parameters left free were adjusted through PHOEBE optimization.

address different stages of the modelling process. These solvers fall into three main categories: estimators, optimizers, and samplers, each progressively refining the model parameters.

3.4.2.1 Estimators: Initial Parameter Guessing

Estimators provide a first approximation of key system parameters directly from the available observational data without requiring a full model computation. These serve as a starting point for more refined optimization techniques. PHOEBE includes three key estimators:

- **EBAI (Eclipsing Binary Artificial Intelligence):** A machine learning-based method introduced by Prša et al. (2008), which employs k-Nearest Neighbors or a trained neural network to estimate parameters such as the time of superior conjunction, inclination, sum of equivalent radii, and temperature ratio. However, it has limitations, particularly for eccentric or contact binaries.
- **LC Geometry Estimator:** A two-Gaussian or polynomial fit approach that estimates similar parameters to EBAI but is often more reliable for well-sampled data.
- **RV Geometry Estimator:** Provides quick estimates of orbital parameters such as mass ratio, semi-major axis, and systemic velocity when RV curves are available.

These estimators are useful for efficiently narrowing down initial conditions before proceeding to full optimizations. However, other estimation methods outside PHOEBE can also be utilized to provide independent constraints. For example, the GBART software (Bareilles, 2017) offers an alternative approach for solving orbital parameters from RV curves and can serve as a benchmark for initial RV solutions (see Section A.3). Similarly, empirical calibrations, evolutionary models, and prior spectral classifications can impose additional constraints, refining initial estimates before full LC and RV modelling is performed. When possible, combining multiple estimation techniques ensures a more robust approach.

3.4.2.2 Optimizers: Refining the Best-Fit Solution

Once a reasonable estimate is obtained, PHOEBE employs optimizers to iteratively refine the model parameters by minimizing the residuals between synthetic and observed light curves or RV curves. The most commonly used optimizers include:

- **Nelder-Mead:** A gradient-free optimization algorithm that efficiently explores local parameter space.
- **Differential Evolution**: A more robust global optimizer capable of handling multi-parameter correlations.

PHOEBE allows for selective optimization of specific parameters. For example, one can optimize only RV parameters first (mass ratio, systemic velocity) before tackling light curve parameters such as inclination and stellar radii. Constraints (Bayesian Priors) can be imposed to keep parameters within physically plausible ranges.

While optimizers like Nelder-Mead and Differential Evolution are effective at refining model parameters, they can struggle with real observational data, where systematics, noise, and deviations from idealized models introduce complexities. In cases where direct optimization fails to converge or leads to local minima, a more efficient approach involves first performing a broad, low-resolution sampling of the parameter space. By computing a large-scale grid of models—varying parameters such as masses and radii in coarse steps—and comparing each model to the observed LC using a root-mean-square error (RMSE) metric, it is possible to identify regions of parameter space that best approximate the observed system (Figure B.0.1). This preliminary coarse search provides a well-constrained starting point for the optimizer, reducing the risk of convergence issues and improving computational efficiency. A more refined grid, with higher accuracy in key parameters, can then be used to further improve the solution before employing traditional optimizers. This approach, detailed in Section B, has been successfully applied in the modelling of WR21a and KU Car, demonstrating its effectiveness in recovering physically consistent solutions for different binary systems (Barbá et al., 2022; Martín-Ravelo et al., 2021).

3.4.2.3 Samplers: Exploring Parameter Space

For a comprehensive parameter study, samplers provide posterior probability distributions, allowing for uncertainty estimation and parameter correlation analysis. PHOEBE includes:

- **MCMC with EMCEE:** A Bayesian approach that explores the parameter space by drawing samples from a posterior distribution.
- **Nested Sampling:** Used when multiple parameter sets can fit the data, providing a probabilistic framework for selecting the most likely solution.

MCMC is particularly useful when parameters such as third-light contamination, stellar temperatures, or orbital eccentricities introduce degeneracies.

Chapter 4

Results

In this chapter, the YMDB catalog is presented in detail, including its construction based on the analysis of TESS light curves and spectroscopic data, complemented by a review of existing literature.

Eclipsing binaries offer a unique opportunity to determine stellar parameters with high precision, especially when combining LC information with RV data. Detached binaries are particularly valuable due to the minimal interaction between their stellar components, allowing for accurate determinations of stellar parameters.

Although systems within the O8–B3 spectral-type range are common, few have had their absolute parameters precisely measured. The YMDB catalog addresses this knowledge gap by providing a curated database of young massive detached binaries, facilitating high-precision stellar parameter determinations.

Through the analysis of TESS LCs for 87 systems with suspected spectral types in the range O9-B1, this study identified 20 new eclipsing binaries (Table 4.1.1), including 13 previously unknown variable systems. Additionally, new LC classifications were reported for 30 systems, and novel features such as eccentricity and heartbeat (LCs of systems displaying heartbeat phenomena are shown in Fig. C.1.1)

The YMDB catalog offers a reliable resource of high-quality LCs, serving as a valuable asset for the astronomical community. The primary results of this study are documented in Table 4.1.2, which lists the 30 confirmed members of the YMDB. These systems feature detached LCs and have at least one component with a spectral classification within the specified range. For the 25 systems that show potential yet require further spectroscopic verification, details can be found in Table 4.1.3. The 32 systems that do not qualify for the catalog due to nondetached configurations or incompatible spectral types are included in Table 4.1.4

4.1 The YMDB catalog

Among the 87 systems, this study reveals 20 new eclipsing binaries (Table 4.1.1), including 13 whose variable nature was previously unknown, 5 targets that were previously identified as photometric variables or spectroscopic binaries but not as DEB, and 2 systems classified as nonthermal contact binaries due to the absence of sharp transitions from the continuum before and after the eclipses, distinguishing them from Algol-type detached systems. Moreover, we introduce new LC classifications for 30 systems and report novel findings such as eccentricity in 13 systems, heartbeat features in 17, new types of variability in 11, and debut TESS LC presentations for the majority of the sample.

The study's results are presented in three distinct tables: confirmed members of the catalog (Table 4.1.2), candidates pending spectral classification (Table 4.1.3), and unqualified candidates (Table 4.1.4). Confirmed members are detached eclipsing binaries (DEBs) whose spectral types fall within a range centered around B0.5V. The YMDB catalog is designed to focus on B0.5V stars, but a controlled dispersion around this target spectral type was permitted. Systems with slightly earlier or later spectral types (O9–B1) or small deviations in luminosity class (IV–V) were considered acceptable, provided that the deviations did not extend in both axes simultaneously. On the other hand, Candidates are DEB that show potential signs of meeting the spectral type criteria but lack definitive confirmation due to incomplete or inconclusive spectral classification.

Unqualified systems are those whose LCs do not appear detached (EB or EW), have primary spectral classifications clearly out of range, or both. The secondary component's classification might either be out of range or impossible to detect due to limitations in current spectroscopic data and analysis. While unqualified detached systems with indeterminate secondary classifications are currently unsuitable for the catalog, future higher-resolution or more sensitive spectra could reveal additional stellar features, prompting their reconsideration as candidates.

For each group, we detail findings from our photometric analysis, including delta magnitude (Δmag), period (P), time of minima (T_0), observed apsidal motion (Apsidal), additional system variability (MultiP), heartbeat phenomena (HB), and eccentricity (e). Additionally, we provide our spectral classifications for certain stars, either to fill gaps where classifications were absent or to verify existing classifications.

We compared the periods obtained from our analysis of the TESS data with those previously published. Some of the periods we derived were found to be twice as long as the previously reported ones, namely for HD 99630 and CD-28 5257, while V*KU Car derived period was found to be half the reported one. This discrepancy is likely due to the improved depth and resolution of the eclipses identified in the TESS data, enabling a clearer distinction between primary and secondary eclipses.

Regarding new spectral types, we confirmed HD 298448, CD-28 5257, HD 309036, V* IK Vel as entries to the YMDB (Table 4.1.2), and emphasize that certain eclipsing binary systems were excluded from the YMDB catalog because their spectral types fall outside the range studied here. An intriguing example is CE CMa (=Gaia DR3 2928505622380096256), which lacks a documented spectral type in the eight publications indexed in the Simbad database. Our April 2023 night spectrum reveals absorptions consistent with an F5 V type, characterized by similar H and K Calcium lines and the presence of the G-band.

Table 4.1.1: Newly identified eclipsing binaries.

Simbad	RA	Dec	V
New variables discovered (DEB)			
BD+66 1674	00 02 10.2414	+67 25 45.186	9.6
BD+66 1675	00 02 10.2887	+67 24 32.228	9.08
HD 278236	05 26 55.2050	+40 32 53.088	10.86
RAFGL 5223	07 08 38.7906	-04 19 04.847	12.06
TYC 8174-540-1	09 20 18.7707	-49 50 25.869	11.63
HD 102475	11 47 18.1823	-62 26 10.246	9.09
HD 114026	13 08 44.0123	-60 20 18.400	9.36
CPD-63 3284	14 31 58.7177	-63 36 17.783	11.2
UCAC2 5911156	15 15 25.1420	-59 09 48.929	12.17
HD 142152	15 55 33.8521	-54 46 35.833	9.82
CD-54 6456	15 55 39.6014	-54 38 36.636	10.41
HD 144918	16 10 29.1581	-49 02 47.091	9.96
BD+55 2722	22 18 58.6254	+56 07 23.482	10.15
New eclipsing binaries discovered (DEB)			
HD 277878	05 18 22.7563	+41 56 06.000	10.27
* psi02 Ori	05 26 50.2293	+03 05 44.422	4.61
LS VI +00 25	06 48 50.4782	+00 22 37.694	10.86
CD-53 6352	16 00 26.8255	-53 54 39.860	10.4
HD 338961	19 50 24.4190	+27 27 55.913	10.86
New eclipsing binaries discovered (not DEB)			
LS V +38 12	05 20 00.6489	+38 54 43.505	10.4
HD 305850	11 01 52.2783	-60 00 46.795	8.8

Note: List of 20 eclipsing binaries identified in this study. This includes 13 binaries previously unrecognized as variables, five known either as photometric variables or spectroscopic binaries but not as DEBs, and two identified as nonthermal contact binaries.

Another case is GN Nor (=Gaia DR3 5884730512723833984), which similarly lacks spectroscopical references in Simbad. Our CASLEO spectrum is classified as A0 V, primarily due to the dominance of Balmer lines. Similar cases are V* GN Nor and * f Vel, whose spectral classifications resulted out of the range for this catalog. These spectra are shown in Fig. 3.3.1.

In certain LCs, we observed additional variability beyond the typical eclipsing patterns. These variations, unless identified as heartbeat phenomena, are denoted with 1 in the tables. Therefore, we detected such oscillations in 37 systems, 11 of which are unprecedented. Finally, the visual inspection of TESS LCs allowed us to detect apsidal motion. This phenomena is indicated in the tables (with 1) when the times of the secondary eclipses seem to vary among different sectors.

We identified a diverse set of interesting systems, each presenting unique photometric characteristics that merit special mention. Firstly, several systems in our sample displayed Tidally Excited Oscillations (TEOs), which are oscillations within a star or system driven by tidal forces due to a close stellar companion. Notable examples include UCAC2 5911156 (detailed in 4.1.3, Fig. 4.1.11) along with V* V4386 Sgr, 2MASS J16542949-4139149, * 23 Ori, and V* V1216 Sco.

Additionally, we have successfully disentangled LCs of systems where the combined photometric data initially obscured individual components. Systems such as CD-59 3165 (detailed in 4.1.2, Fig. 4.1.8), as well as BD+66 1674 and eta Ori (both in 4.1.1, Figs. 4.1.2 and 4.1.3, respectively).

We also observed systems whose eclipse characteristics vary significantly over time, adding another layer of complexity to their study. For instance, HD 278236 initially showed flat eclipses typical of total eclipses but over a span of 1500 days, the eclipse profile gradually transitioned to partial, with a smoothing and narrowing that indicates dynamic changes in the system. Additionally, the shifting of the secondary eclipse suggests apsidal motion, highlighting the system's evolving orbital dynamics. (Fig. 4.1.4). HD 93683 exhibited a decrease in eclipse depth over 1500 days, suggesting changes in the system's configuration or surrounding material (Fig. 4.1.5). And BD+66 1675 (detailed in 4.1.1, Fig. 4.1.7) presented a heartbeat-like feature post-primary eclipse, which shifted to prior the eclipse over 1150 days of observation.

4.1.1 Confirmed Members

The 30 confirmed members of the YMDB catalog meet the established criteria for inclusion: they display detached eclipsing binary (DEB) light curves and have spectral types centered around B0.5V, with a controlled dispersion. Systems with slightly earlier or later spectral types (O9–B1) or small deviations in luminosity class (IV–V) were considered acceptable, provided that the deviations did not extend in both axes simultaneously. These systems represent the most reliable targets for precise determinations of stellar masses and radii, as their minimal interaction ensures their evolutionary pathways remain largely unaltered by binary effects. Table 4.1.2 summarizes the properties of these systems, including their orbital parameters and photometric variability, while their corresponding TESS light curves are shown in Figure 4.1.1. Below, we provide detailed descriptions of each confirmed system, highlighting key features and any additional characteristics of interest.

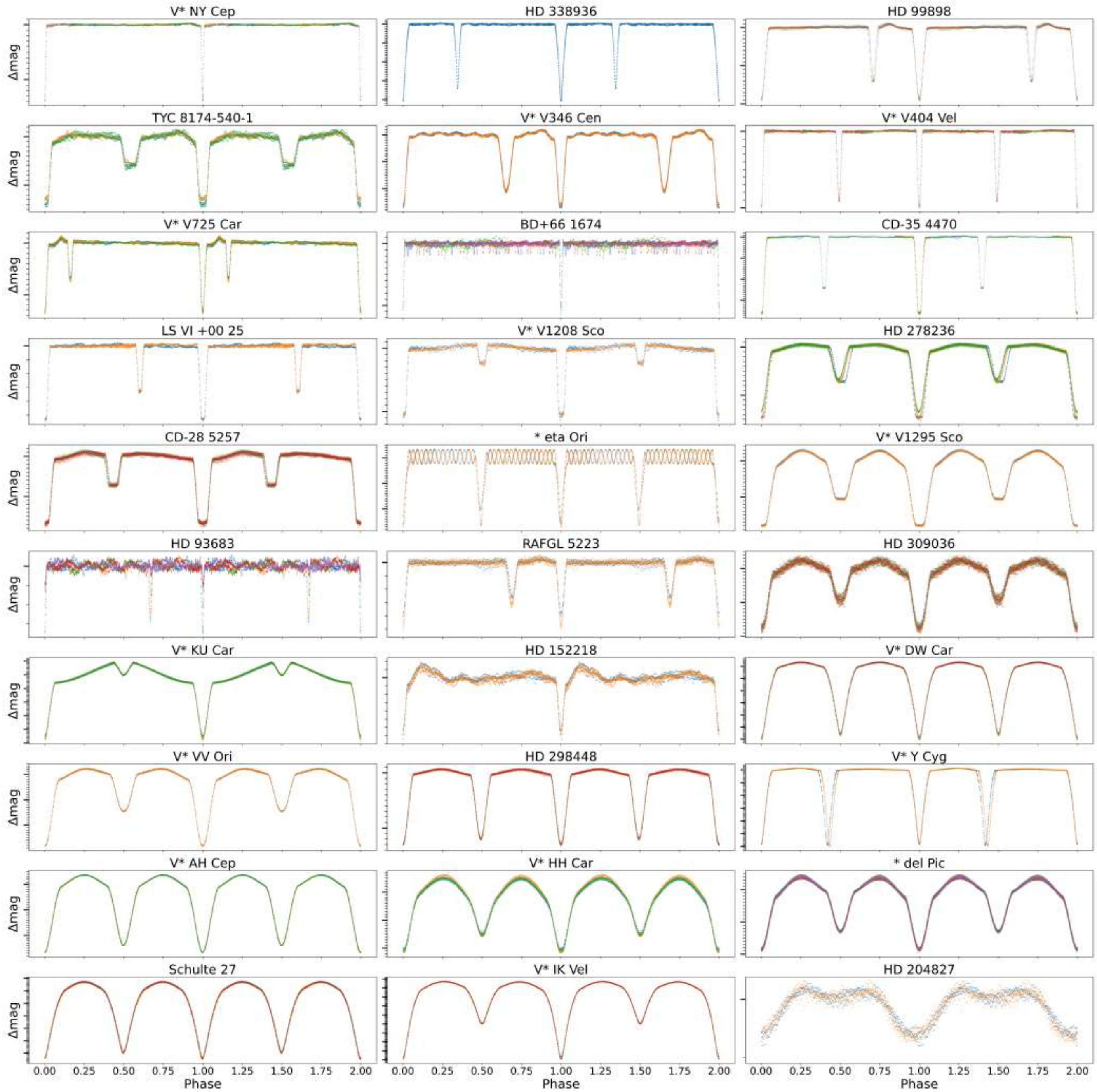

Figure 4.1.1: Light curves belonging to the confirmed category. In each subpanel, bold, long ticks on the Y-axis denote increments of $0.1\Delta mag$, and thin, short ticks indicate increments of $0.01\Delta mag$.

Table 4.1.2: Confirmed systems in the YMDB catalog.

SIMBAD	ΔMag	P	T0	Apsidal	Multi_P	HB	e	ET	ST1	ST2
V* NY Cep	0.140	15.2759	1768.17910		0	1	1	EA1	B0.5V	B2V
HD 99898	0.206	5.04950	2324.03500	1	0	1	1	EA2	B0V	
V* V404 Vel	0.103	11.4243	1518.04660		0	0	1	EA2	B0V	
HD 298448	0.142	2.31530	1545.16410		0	0	1	EA2	B1 V ^{tw}	
V* KU Car	0.574	2.96059	1571.58360		0	0	0	EA2	B0.5 V(n)	
BD+66 1674	0.123/0.017	18.8292 / 2.6395	1783.81040 / 2887.35633		0 / 1	0 / 1	- / 1	EA1 / EA2	B0 V ^{tw}	B0 V ^{tw}
V* V1208 Sco	0.124	5.21970	2387.49300		0	0	0	EA2	B0.5 V	*
V* AH Cep	0.308	1.77478	1792.24979		0	0	0	EA2	B0.2 V	B2 V
V* DW Car	0.647	1.32774	1597.83274		0	0	0	EA2	B1 V	B1 V
eta Ori	0.308 / 0.061	7.9886 / 0.4321	1472.43778 / 1469.94135		1	0	1 / 0	EA2 / EW	B0.7 V	B1.5: V
del Pic	0.243	1.67254	2389.11655		1:	0	0	EA2	B0.5 V	B0.5-3
V* VV Ori	0.310	1.48538	2199.25573		1	0	0	EA2	B1 V	B4.5 V
HD 338936	0.417	7.670	2771.85150		1	0	1	EA2	B0.5 V db	
TYC 8174-540-1	0.162	5.04690	1546.33040		1	1	1	EA2	O9.5 V ^{tw}	
LS VI +00 25	0.057	11.0287	2221.42860		0	0	1	EA2	O9.5 V	
HD 278236	0.157	1.99270	1816.47898	1	0	0	1	EA2	O9 V	
CD-28 5257	0.196	3.10894 / 3.38:	2253.54773 / 1498.46100	1	1	1	1	EA2	B0 V ^{tw}	
HD 93683	0.041:	17.7978	1574.31401	1	1	0	1	EA2	O9 V	B0 V
HD 152218	0.089	5.60410	1649.95040		1	1	1	EA1	O9 IV	O9.7 V
V* V346 Cen	0.293	6.322	1570.60040		1	1	1	EA2	B0.5 IV	B2 V
CD-35 4470	0.372	9.3535	1539.49440		0	0	1	EA2	B0 IV	
HD 309036	0.232	2.31525 / 0.12398	2356.19344		1	0	0	EA2	B1 V ^{tw}	
V* IK Vel	0.874	1.99232	1518.81743		0	0	0	EA2	B1 V ^{tw}	
RAFGL 5223	0.053	3.55907	1494.99690	1:	0	1	1	EA2	O9 V ^{tw}	*
Schulte 27	0.629	1.46920	1683.74890		0	0	0	EA2	O9.7V(n)	O9.7V(n)
V* HH Car	0.281	3.23146	1599.54000		0	0	0	EA2	O9 V	B0 III-IV
V* V1295 Sco	0.218	2.15764	1627.79500		0	0	0	EA2	O9.7 V	*
V* V725 Car	0.152	9.4106	1570.04690		0	1	1	EA2	O9.7 IV	*
V* Y Cyg	0.614	2.99625	1711.75278	1	0	1	1	EA2	O9.5 IV	O9.5 IV
HD 204827	0.011	3.0480	1743.64949		1	0	0	EA2	O9.5IV	*

Note: Summarized version of the YMDB catalog for confirmed systems. The table includes Delta magnitude (Δmag), orbital Period (P), and Time of minimum light (T0) from extracted TESS LCs. Identified features such as Apsidal motion, additional variability (Multi_P), Heartbeat-like features (HB), and Eccentricity (e) are presented with "1" indicating detection and "0" indicating nondetection. The Eclipsing Type (ET) is indicated as EA (Algol), EB (Beta Lyrae), or EW (W Ursa Majoris type), followed by "2" if both primary and secondary eclipses are visible, or "1" if only one is visible. A "/" between types indicates multiple discernible variations from the TESS LC. Spectral types for primary and secondary components are provided, with classifications performed in this work marked with "^{tw}". An asterisk "*" instead of a spectral type indicates significant dispersion among various reliable sources, without a clear consensus. Uncertainties across the table are indicated by ":". Full details, error margins, and sources for spectral types not classified in this work are available in the CDS extended version.

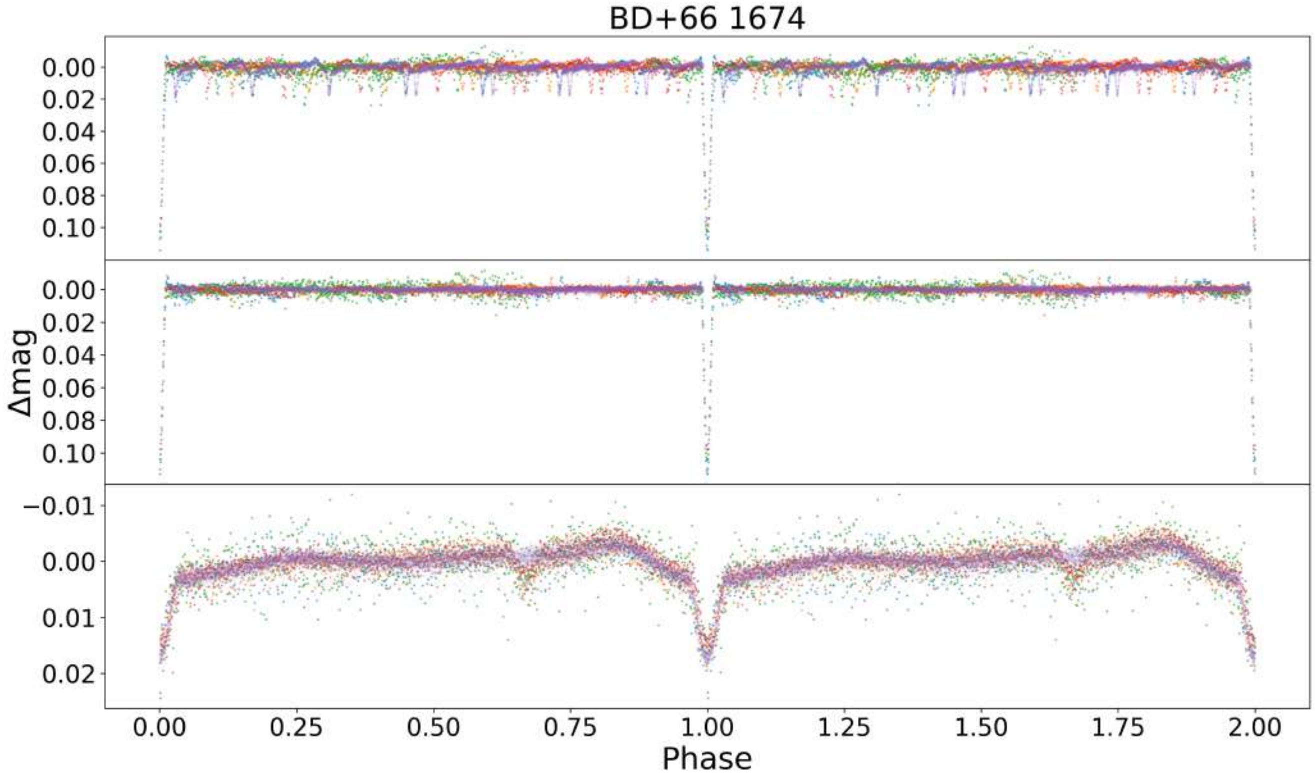

Figure 4.1.2: Light curves of BD+66 1674. The top panel displays the composite LC, while the middle panel shows the LC corresponding to the B0 V+ B0 V system. In the bottom panel, the LC of the newly discovered eccentric short-period DEB system is depicted, with its sources unidentified as of yet. Each color represents a different sector of TESS.

BD+66 1674: Initially noted as a probable RV variable (Crampton & Fisher, 1974), no additional references were found in the available literature. Although Maíz Apellániz et al. (2016) classified it as O9.7 IV, an analysis, incorporating high-resolution spectra from the Galactic O-Star Spectroscopic Survey (GOSSS; Maíz Apellániz et al., 2016) and the Library of Libraries of Massive-Star High-Resolution Spectra (LiLiMaRlin; Maíz Apellániz et al., 2019a), revealed it to be a B0 V + B0 V system (Maíz Apellániz, priv. comm.). Consequently, it has been included in the YMDB. Its LC displays additional variations beyond the 18-day eclipsing pattern, resembling those of highly eccentric detached double-eclipsing systems. Moreover, a notable bump between eclipses suggests the presence of a heartbeat-like feature (see Fig. 4.1.2). Considering the pixel size of TESS data, we conducted a search for other targets within a 40 arcsec radius and identified seven Gaia sources. These sources, at least four G-magnitudes fainter than BD+66 1674, complicate the determination of whether the short-period binary is one of these sources or an unresolved component of BD+66 1674.

*** eta Ori**: *Eta Ori is a visual binary and an ideal candidate for our catalog as it meets the criteria of a DEB with spectral types B0.7 V and B1.5: V. Southworth & Bowman (2022) analyzed TESS data and fitted the LC to obtain absolute parameters for the system, opting not to use data from sector 32 due to its low variability amplitude. In our study, we present LCs using both sectors (Fig. 4.1.3). We confirm

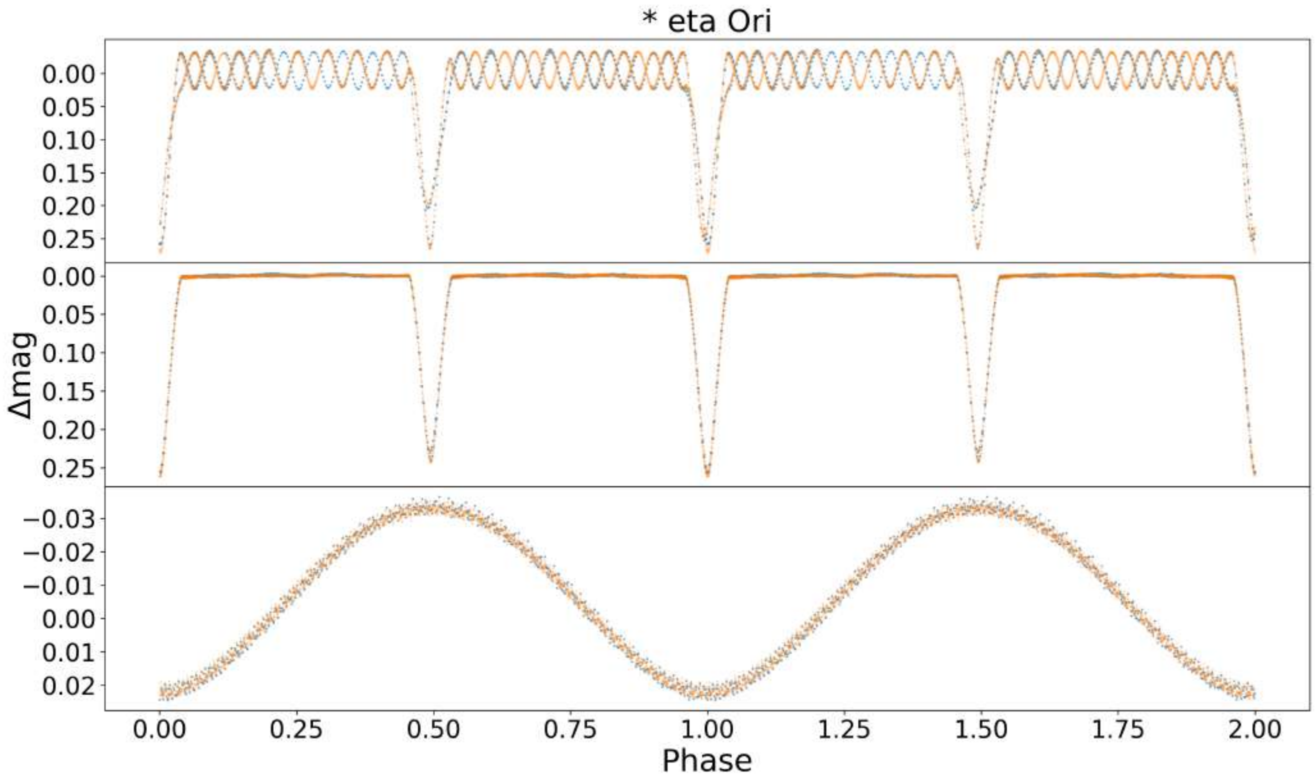

Figure 4.1.3: Light curves of * eta Ori. The top panel displays the composite LC. The middle panel illustrates the LC for the eclipsing system with a period of 7.989 days disentangled from the shorter period pulsations, while the bottom pannel shows such pulsations folded with period of 0.432 days. Each color represents a different sector of TESS

the periodic variations reported in the literature: the primary eclipse cycle at approximately 7.989 days, indicative of the detached eclipsing binary system, and a shorter sinusoidal cycle of about 0.432 days. Lee et al. (1993) initially suggested that the shorter period might indicate a contact binary with a period of 0.864 days. Southworth proposed the configuration as a detached EB with a period of 7.988 days, where one component exhibits g-mode pulsations, alongside a noneclipsing binary with a period of 0.8641 days, showing strong ellipsoidal variations.

HD 278236: Classified as O9 V by Georgelin et al. (1973), no publications reporting variability or binarity were found. It is noteworthy that the relative position of the secondary eclipse appears to vary in different sectors, indicating apsidal motion (Fig. 4.1.4). Moreover, apsidal motion is making the secondary eclipse narrow overtime (from sector 17-59 ∼1100 days and from 59-73 equivalent to ∼1400 days, for a total time span of ∼2500 days).

V* VV Ori: VV Ori is a well-studied eclipsing binary within the Orion OB1b association, consisting of a detached pair of B-type main-sequence stars with an orbital period of 1.485 days. The system is particularly notable for its β Cep-type pulsations, primarily attributed to the more massive B1 V primary. A recent study by Budding et al. (2024), combining TESS photometry with high-resolution spectroscopy,

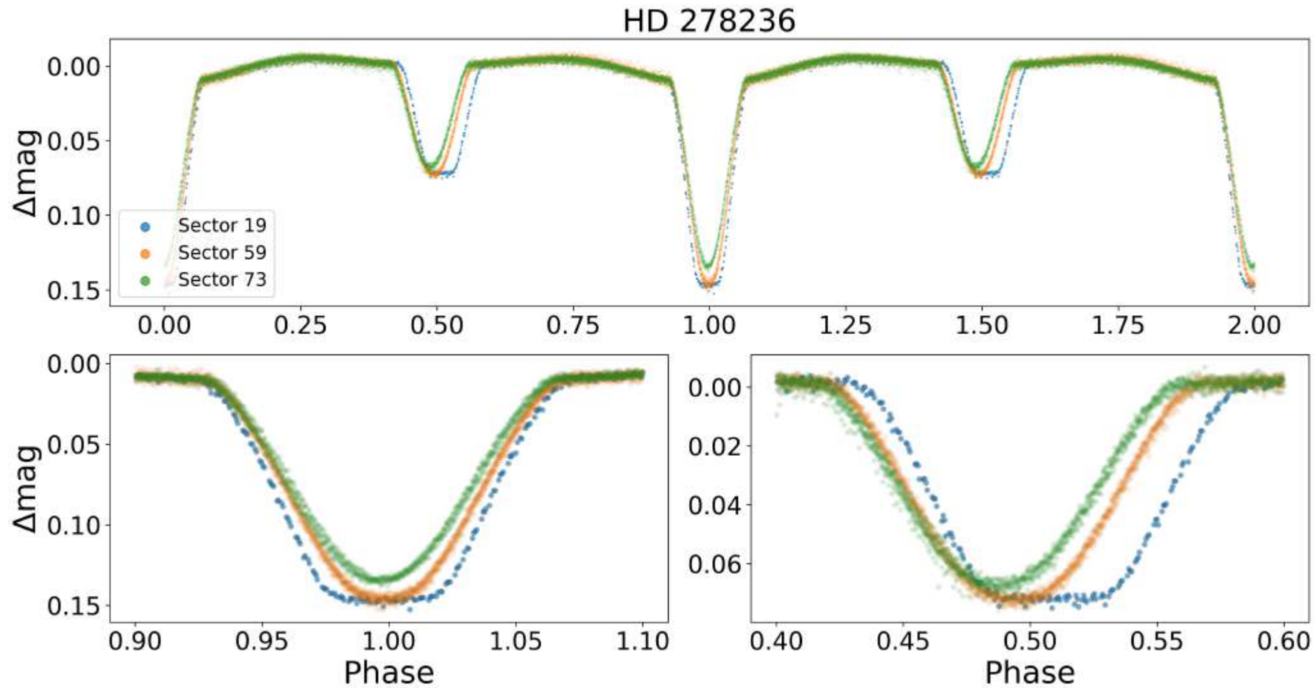

Figure 4.1.4: Light curves of HD 278236. The top panel displays the composite LC of the system. Bottom left and right panels provide zoomed views of the primary and secondary eclipses, respectively. Observations from Sectors 19 to 73 span 1500 days. In the earliest sector (17) the eclipse exhibits a flat profile, indicative of a total eclipse. Over time the eclipse profile gradually smoothens, completely losing its flatness by the latest observed sector (73), indicative of a shift to a partial eclipse. Apsidal motion is also evident in this system, as demonstrated by the phase shift of the secondary eclipse.

refined the system's absolute parameters, determining masses of $11.56 \pm 0.14\ M_{\odot}$ and $4.81 \pm 0.06\ M_{\odot}$ for the primary and secondary, respectively, along with radii of $5.11 \pm 0.03\ R_{\odot}$ and $2.51 \pm 0.02\ R_{\odot}$. The system follows a nearly circular orbit with a semi-major axis of $13.91 R_{\odot}$ and an estimated age of 8 ± 2 Myr. A third component, resolved via speckle interferometry, is located at ~ 87 AU, with an estimated mass of $2.0 \pm 0.3\ M_{\odot}$, suggesting an orbital period of approximately 200 years. Spectral disentangling revealed that the primary rotates at 80% of the expected synchronous value, likely due to precession of an unaligned spin axis. While previous studies suggested the presence of a close third body with a period of 120 days, recent RV analyses do not support this hypothesis. VV Ori remains a key system for studying the evolutionary properties of massive stars, pulsational behaviour, and spin-orbit interactions in young multiple systems, particularly given its variable inclination over time, which provides valuable constraints on stellar dynamics in hierarchical triples.

δ Pic: It is an early-type eclipsing binary composed of two main-sequence stars, with the primary component's spectral classification ranging from B0.5 III Thackeray (1966) to B1.5 V Eaton & Wu (1983). The system exhibits shallow, partial eclipses due to its low inclination ($i = 65.2^{\circ}$ in the detached model). Early studies suggested the presence of circumstellar material affecting the light curve, with phase-dependent absorption features possibly causing dips before and after eclipses Cousins (1966); Wu (1976), but later high-precision ultraviolet photometry from the Astronomical Netherlands Satellite (ANS) found no strong evidence supporting this hypothesis Eaton & Wu (1983). Residual scatter in the light curves, however, suggests possible intrinsic variability, potentially linked to mass loss from the hotter component Kondo et al. (1980). The system has been modeled under both detached and semidetached configurations, with the detached solution favored as it aligns with the spectroscopic mass ratio ($q = 0.53$), whereas the semidetached model, despite providing a better luminosity ratio fit, suggests an unrealistically high primary mass of $42 M_{\odot}$ and a mass ratio of $q = 0.36$, contradicting spectroscopic measurements. Ultraviolet observations confirm the system's relative stability, with minimal interstellar extinction and integrated colors consistent with a B1.5 V spectral type. Previous studies report an orbital period of $P = 1.67254$ days Eaton & Wu (1983).

LS VI +00 25: It was initially identified as an SB1 system by Munari & Tomasella (1999), although no photometric variations have been reported to our knowledge based on available literature. With a spectral type of O9.5 V (Li, 2021), we have included it in the YMDB.

RAFGL 5223: Recognized as a Herbig Ae/Be star candidate, its entire bibliography is centered around this characteristic. However, no indications of variability, either spectroscopic or photometric, were identified. To scrutinize the indicated spectral classification in the Simbad database, we downloaded a X-Shooter spectrum (program ID 084.C-0952(A)) from the ESO portal. By evaluating the ratios between He II and He I pairs, we determined it to be of O9.2 type, with He II λ4686/He I λ4713 and Si IV λ4089/He I λ4026 ratios indicative of a V luminosity class. Consequently, it has been included in YMDB as an eccentric short-period binary. We note a potential heartbeat feature, manifested as a bump in the orbital phases where the periastron passage is expected. We also remark a probable apsidal motion, as separation between eclipses seems to vary among Sectors 7 and 33 (∼700 d).

CD-28 5257: It is a recognized eclipsing binary (see e.g., Pozo Nuñez et al., 2019), although the reported periodicity is incorrect. Our analysis reveals it to be an eccentric double-eclipsing system, with eclipses corresponding to both transits and occultations. Furthermore, a marginal bump is observed in the orbital phases where the expected periastron occurs, which we identify as a heartbeat effect, made possible by the precision of the TESS data. This star is marked for exhibiting apsidal motion in Table 4.1.2, as the orbital phases of the secondary transits appear to vary across available Sectors 7, 8, 34, and 61.

CD-35 4470: First identified in OB association studies by Westerlund (1963) and later included in the Luminous Stars in the Southern Milky Way catalog (Stephenson & Sanduleak, 1971). It was classified as a B0 IV star by Moffat et al. (1979) and subsequently listed in multiple OB star catalogs without additional spectroscopic updates (Reed & Beatty, 1995; Reed, 1998, 2003). The system's eclipsing binary nature was first confirmed by Shivvers et al. (2014), who identified it as an Algol-type binary with a well-defined photometric period. This classification was later supported by Kim et al. (2018), who provided additional constraints on its orbital parameters and eccentricity.

V* V404 Vel: Initially cataloged among luminous stars in the southern Milky Way (Stephenson & Sanduleak, 1971), its first spectral classification was provided by Garrison et al. (1977) and later updated to B0 V by Bassino et al. (1982). The system was first noted as an eclipsing binary by Otero & Dubovsky (2004), who also suggested an eccentric orbit. Its detached Algol-type (EA) nature and an accurate period determination were later confirmed by Avvakumova et al. (2013). More recent compilations have included V* V404 Vel in catalogs of eccentric eclipsing binaries, reinforcing its classification as an eccentric system (Kim et al., 2018).

V* IK Vel: First cataloged in the Henry Draper Catalogue (Cannon & Pickering, 1993), its spectral classification was systematically re-evaluated by Houk (1978), who assigned it a B5 type but noted that the spectrum appeared washed out with shallow lines, possibly due to subtle overlap, and suggested that it should be reclassified. In (Martín-Ravelo et al., 2024) we conducted a new spectral classification and determined it to be a B1 V system, placing it within the YMDB criteria. The system was initially recognized as a variable star (Kholopov et al., 1981), later identified as an eclipsing binary by Reed (2005), and its detached nature, along with its period and light curve, was reported by Alfonso-Garzón et al. (2012). Given its confirmed spectral type and detached eclipsing nature, V* IK Vel is included in the YMDB.

TYC 8174-540-1: Initially identified as an OB star by Muzzio & Orsatti (1977) and subsequently classified as O9.5 Vn by Bassino et al. (1982), TYC 8174-540-1's spectral type was verified through our own CASLEO spectrum (see Fig. 3.3.1). Despite an absence of reports regarding its binary nature, the TESS LC unmistakably depicts both eclipses, which, in fact, are transit and occultation events. This characteristic increases its significance as a benchmark for determining stellar parameters. Notably, the system exhibits eccentricity and appears to manifest a heartbeat phenomenon before entering the primary eclipse.

HD 298448: Originally classified as B1 V by Garrison et al. (1977), this spectral type was independently confirmed in this work (Martín-Ravelo et al., 2024). The system was first identified as an eclipsing binary in the variable star catalog by Pojmanski (2002), who also classified it as detached (EA) and provided its period and light curve data. Given its confirmed spectral type and detached nature, HD 298448 is included in the YMDB.

V* KU Car: KU Car, reported as B8 in SIMBAD from Avvakumova et al. (2013) and initially observed with a period of 5.92 days by O'Connell (1951), is reexamined in the author's Master's dissertation

Martín-Ravelo et al. (2021). The dissertation utilized ASAS-3 data, which revealed a secondary eclipse previously unnoticed, effectively revising the reported period to 2.96 (half the previously reported) days. Detailed spectral analysis was performed using data from the Galactic O Star Spectroscopic Survey Sota et al. (GOSSS; 2011, 2014); Maíz Apellániz et al. (GOSSS; 2016), which led to a revised spectral classification of B0.5 V(n). While O'Connell previously suggested an eccentric orbit based on the LC's shape outside the eclipses, this hypothesis was biased by an incomplete understanding of the LC's true nature. Our observations do not indicate eccentricity from the LC; only a comprehensive RV study could resolve this ambiguity. Ongoing spectroscopic analysis aims to refine the temperature and absolute parameters of KU Car.

V* DW Car: Originally discovered as an eclipsing binary by Hertzsprung (1924) with a good period determination. The system is a member of the open cluster Collinder 228 (Levato & Malaroda, 1981), and its first spectroscopic orbit was determined by Ferrer et al. (1985), confirming it as an SB2 system with spectroscopic classification of B1V+B1V. A comprehensive spectrophotometric analysis by Southworth & Clausen (2007) provided absolute dimensions, further characterizing its binary nature. Alfonso-Garzón et al. (2012) included it in their catalog of optically variable sources, refining its classification and period. More recently, IJspeert et al. (2021) observed the system with TESS.

V* V725 Car: It is a DEB in a highly eccentric orbit, with an RV curve determined for its primary component (Kiminki & Smith, 2018). The new LC presented here reveals a distinct heartbeat effect between the closer eclipses. An integrated analysis of both datasets, spectroscopic and photometric, will enable the determination of stellar parameters for both components.

HD 93683: It is recognized as an SB2 system with a Be-type third component (Alexander et al., 2016; Bodensteiner et al., 2020). Our analysis of the TESS data unveiled intriguing behavior in this system, characterized by an attenuation of its eclipses (Fig. 4.1.5). This phenomenon could arise from variations in the brightness of the variable Be-star (either the star itself or its surrounding disk), which may dilute the eclipses. Alternatively, it could result from a rare effect known as Zeipel-Lidov-Kozai cycles, induced by the third component in a noncoplanar orbit, leading to changes in the orbital plane relative to our line of sight (Borkovits et al., 2022). Another possible explanation is a change in the system's inclination, as observed in HS Hydrae, where the eclipses disappeared due to precession caused by a third companion (Davenport et al., 2021). However, PHOEBE can also simulate this effect by diminishing the stellar radii, which presents an alternative scenario to explain the observed eclipse attenuation. This multiple system also exhibits several short-period variations, interpreted as pulsations. Shi et al. (2022) reported one such variation with a period of 2.4 days. Further analysis is needed to determine additional periodicities in the TESS data.

V* HH Car: Initially discovered and reported by O'Connell (1968), who provided its orbital elements and identified apsidal motion, estimating an apsidal period of approximately 660 years. The system was further analyzed by Bakış et al. (2021), who conducted a spectroscopic study using high-resolution spectra ($R \sim 48,000$), determining precise absolute parameters. The primary component was classified as an O9 V star, while the secondary was identified as a B0 III-IV star, with masses of $17.2 \pm 1.2 M_{\odot}$ and $10.3 \pm 0.9 M_{\odot}$, respectively. The light curve solution revealed that the system is semidetached, with the secondary component filling its Roche lobe and undergoing mass transfer to the primary. This interaction generates a circumstellar structure, evident in the strong Hα emission. Additionally, Bakış et al. (2021)

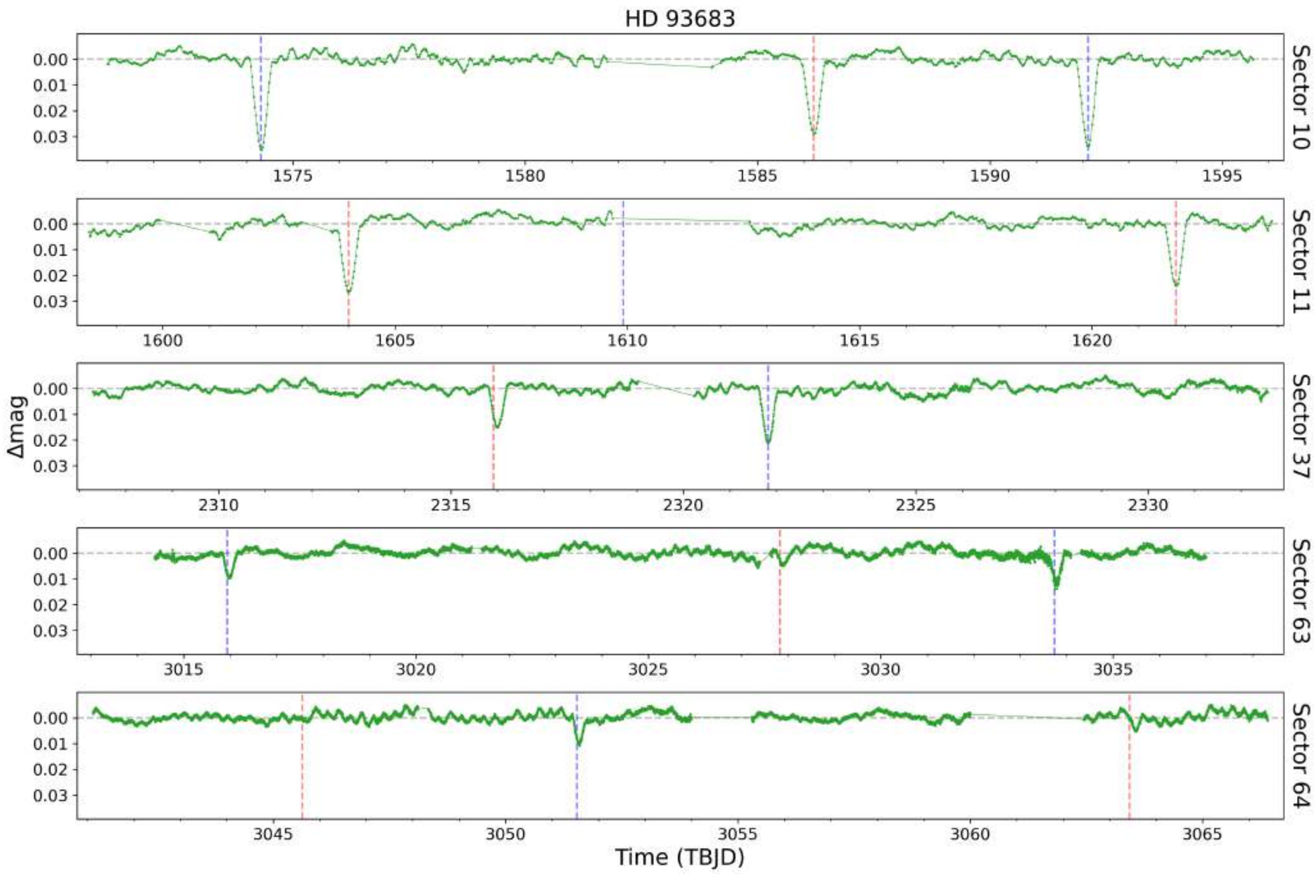

Figure 4.1.5: Light curves of HD 93683. Each panel represents a different TESS sector, arranged chronologically from top to bottom. Predicted timings for the primary and secondary eclipses are marked with blue and red dashed vertical lines, respectively. All panels maintain equal Y and X axis scales. Over 1500 days, both primary and secondary eclipses consistently decrease in depth from approximately 0.3Δmag to around 0.1Δmag, with the secondary eclipses being shallower overall. By the latest sector (64), the depth of the eclipses approaches the level of the system's intrinsic variability, rendering the first secondary eclipse undetectable. Apsidal motion is evident as early as Sector 37 when compared to Sector 10, although data from later sectors are not reliable for further apsidal motion analysis.

modeled the circumstellar material using SHELLSPEC, revealing an expanding shell with a temperature of $\sim 22,000$ K and a high-temperature impact region ($\sim 100,000$ K) at the site of wind-wind interaction and mass transfer. The system is located at a distance of 4.6 ± 0.8 kpc, consistent with Gaia DR3 estimates.

HD 99898: This star is a previously identified variable, classified as Algol type (Pojmanski, 1998), and subsequently analyzed as a detached eclipsing binary (DEB) displaying apsidal motion (Khaliullin et al., 2006). However, no heartbeat phenomenon was reported prior to this study.

V* V346 Cen: First recognized as a variable star by Guthnick & Prager (1936), V346 Cen was subsequently analyzed by Russell (1939) in the context of ellipticity in eclipsing binaries. Savedoff (1951) examined its apsidal motion parameter, while Feast et al. (1961) provided early spectral classification, identifying it as a B-type star. Popper (1966) included it in a spectroscopic survey of southern eclipsing binaries, and Landolt (1967) reported photometric observations. Moffat & Vogt (1975) performed UBV photometry in the region of Stock 14, confirming V346 Cen as a member of this cluster. The first spectroscopic orbit was determined by Hernandez & Sahade (1978). Gimenez et al. (1986b,a) conducted detailed photometric studies, deriving apsidal motion parameters and light curve solutions. The system was later included in catalogs of apsidal motion binaries (Hagedus, 1988; Petrova & Orlov, 1999). Mayer et al. (2016) revisited the system, refining orbital and stellar parameters and confirming a significant eccentricity ($e = 0.289$). The latest comprehensive study, Pavlovski et al. (2023), provided precise fundamental parameters, confirming the primary as a B0.5 IV star (Fitzgerald & Miller, 1983) and the secondary as B2 V, along with detailed chemical abundance analysis. Their study also identified tidally excited pulsations in the system. V346 Cen remains a benchmark high-mass binary for testing stellar interior models.

HD 309036: Initially cataloged as a luminous star in the Southern Milky Way by Stephenson & Sanduleak (1971), HD 309036 was later classified photometrically as a b2 ii star by Klare & Neckel (1977), while a spectroscopic analysis by Loden et al. (1976) refined its classification to B2-B3. In Martín-Ravelo et al. (2024), we performed a spectral reclassification and determined HD 309036 to be a B1 V star, confirming its membership in the YMDB. Pojmanski (1998) first reported the system's periodic variability, identifying it as an eclipsing binary. Later, Alfonso-Garzón et al. (2012) classified it as a detached (EA) system and provided light curves, supporting its inclusion in the catalog. The system's placement within its stellar environment was further studied using Gaia DR3 data (Gaia Collaboration, 2022), contributing to a refined understanding of its position within the local spiral structure (Xu et al., 2021).

HD 152218: This system was first identified as an SB2 binary by Struve (1944), but its orbital elements were not determined until Hill et al. (1974), who reported a period of 5.4 days. The first published light curve was provided by Otero & Wils (2005) using ASAS data. Sana et al. (2008) conducted a comprehensive analysis, confirming the system as an O9 IV + O9.7 V binary with an orbital period of 5.604 days and an eccentricity of 0.259, slightly lower than previously accepted values. They also identified a rapid apsidal motion of approximately 3° per year. More recent studies (Rauw et al., 2016; Rosu et al., 2022) have refined these measurements, reporting an apsidal motion rate of $\dot{\omega} = (2.04^{+0.23}_{-0.24})^{\circ}\ \mathrm{yr}^{-1}$ and an eccentricity of $e = (0.280^{+0.010}_{-0.008})$. The photometric variability observed in the TESS light curve by IJspeert et al. (2021) reveals that only one eclipse is detected, suggesting a grazing geometry or partial eclipse. Additionally, Kołaczek-Szymański et al. (2021) identified a heartbeat-like variation in the system (see Fig. C.1.1). The presence of colliding winds was established through X-ray monitoring (Sana et al., 2008), showing increased emission near apastron due to wind-wind interaction within the wind acceleration region.

V* V1208 Sco: Initially suspected to be a long-period variable (Balona, 1983), this system was later identified as a spectroscopic binary of type SB1 by Levato & Morrell (1983), who also classified it as B0.5 V under its NGC 6231 232 designation. Shortly after, Balona & Engelbrecht (1985) recognized it as an eclipsing binary. Banyard et al. (2022) later confirmed its SB1 nature but did not report significant deviations from the previous spectral classification. However, more recent work by Banyard et al. (2023) identified it as a double-lined spectroscopic binary (SB2), refining the system's orbital properties. The light curve exhibits well-defined eclipses, confirming its detached nature.

V* V1295 Sco: The system was first classified spectroscopically as B1/2 Ib/II Houk (1978), but a later study refined its classification to O9.7 V Mathys (1988). It was identified as a spectroscopic binary (SB1) with a period of 2.1579 days by Gieseking (1982). Further studies confirmed variability in both radial velocity and photometry Perry et al. (1991). The system was first reported as an eclipsing binary (EA/KE) with a period of 2.15767 days by Otero & Dubovsky (2004), and subsequent observations corroborated this period Mellon et al. (2019). Its detached nature is supported by its well-defined light curve.

HD 338936: The system was first classified as B0.5 V Georgelin et al. (1973). It was identified as an eclipsing binary with an eccentric orbit by Otero et al. (2006), who also determined a reliable period for the system. Further studies confirmed its detached (EA) nature and revealed pulsations Shi et al. (2022). These pulsations, detected using TESS data, indicate additional variability beyond the eclipses, making this system particularly interesting for further analysis.

Schulte 27: The photometric variability of Schulte 27 was first reported by Rios & DeGioia-Eastwood (2004), who determined a period of 1.46 days. Its spectral classification was refined in the Galactic O-Star Spectroscopic Survey (GOSSS), identifying the system as O9.7V(n) + O9.7V(n) Maíz Apellániz et al. (2016). A more detailed study combining radial velocity data from Laur et al. (2015) with new photometric observations led to a PHOEBE model of the system. Further photometric monitoring, including differential photometry Laur et al. (2017), and recent observations from the KISOGP survey Ren et al. (2021), have provided additional insights into the system's variability and binary nature.

V* Y Cyg: It is a well-established SB2 eclipsing binary (Sawyer, 1887) with reported values of $M_1 = 17.72 \pm 0.35\, M_\odot$, $M_2 = 17.73 \pm 0.30\, M_\odot$, $R_1 = 5.785 \pm 0.091\, R_\odot$, and $R_2 = 5.816 \pm 0.063\, R_\odot$ (Harmanec et al., 2014). It has historically been used as a benchmark for apsidal motion studies in massive stars, with an eccentricity of $e = 0.1451$ and apsidal period of (47.805 ± 0.030) yr (Harmanec et al., 2014). The system consists of two nearly identical early-type stars, classified as O9 V + O9.5 V (Burkholder et al., 1997) and later reclassified as O9.5 IV + O9.5 IV in the GOSSS survey (Maíz Apellániz et al., 2019b). TESS data show a marginal flux increase at orbital phases corresponding to the periastron passage, which can be interpreted as a heartbeat effect, although it could also be attributed to ellipsoidal variations. Known apsidal motion is also evident from the variation in secondary eclipse times (and possibly their depths) between sectors 15 and 41 (~ 700 d). It is also identified as a runaway star (Maíz Apellániz et al., 2018).

HD 204827: Initially reported as a variable star in Bidelman (1984), HD 204827 was later identified as a spectroscopic binary (SB1) by Gies (1987), referencing earlier work by Petrie and Pearce (1961).

However, no published orbital solution is available for this system. Its spectral classification was refined to O9.5 IV in the Galactic O-Star Spectroscopic Survey (GOSSS) Sota et al. (2014). The system was included in the INTEGRAL-OMC catalog as a variable star, but no period was provided Alfonso-Garzón et al. (2012). More recently, Prša et al. (2022) analyzed TESS data, confirming its eclipsing nature and publishing a light curve with the same period previously suggested.

V* AH Cep: First identified as a variable star by Guthnick & Prager (1934), who attributed its discovery to Stebbins (1929). It was initially identified as a spectroscopic binary by Plaskett and later investigated by Pearce, AH Cephei was confirmed as an eclipsing variable through observations conducted at Madison in 1928 using a Kunz potassium cell and a Lindemann electrometer Huffer & Eggen (1947). The light variation period was established as 1.77473 days, with shallow eclipses making a unique determination of the geometric elements challenging. The photometric solution, combined with spectroscopic measurements from Petrie, allowed for an estimate of the mass ratio and absolute parameters, with component masses of $17.1 M_{\odot}$ and $14.7 M_{\odot}$, and spectral types refined to B0 V and B0.5 V, respectively Huffer & Eggen (1947). More recent classifications confirm the primary as B0.2 V and the secondary as B2 V Burkholder et al. (1997). TESS observations provided additional insights into the system's variability and precise ephemeris Prša et al. (2022).

V* NY Cep: It is a well-known DEB (see e.g., Albrecht et al., 2011), characterized by a single eclipse resulting from its high eccentricity and periastron longitude. Notably, a bump is observed in its LC just before entering the eclipse, which we interpret as a probable heartbeat, although other proximity effects could not be discarded.

4.1.2 Candidates

The 25 candidate systems included in Table 4.1.3 display DEB LCs and are potential members of the YMDB catalog but lack definitive spectral classifications or exhibit some level of uncertainty in their current spectral type assignment. While these systems are strong candidates for future confirmation, additional spectroscopic observations are necessary to verify whether they meet the spectral type criteria established for confirmed members. Some candidates exhibit properties suggesting their likely inclusion, while others remain ambiguous due to the limitations of existing data. Figure 4.1.6 presents their TESS light curves. Below, we highlight particularly interesting candidates, including those with unusual variability or strong indications of being massive binaries.

BD +66 1675: Classified as O7.5 Vz (Maíz Apellániz et al., 2016), high-resolution spectra obtained within the context of LiLiMaRlin (Maíz Apellániz et al., 2019a) revealed BD +66 1675 to be a triple system comprised of O7.5Vz+O8V +B components. A preliminary analysis of 20 spectra indicated that the RV of the spectral lines belonging to the O7.5 Vz star do not vary within errors. However, the O8V + B pair exhibits RV motion in accordance with the photometric period. Moreover, preliminary orbital elements suggest an eccentric orbit, explaining why only one eclipse is observed. This eclipse occurs when the massive star passes in front of the system, making it a secondary eclipse. Also, we detect a heartbeat-like behavior immediately after the eclipses, but only in the Sector 58 (Fig. 4.1.7), and short-period variability identified as pulsations.

Table 4.1.3: Unconfirmed systems (candidates) for the YMDB catalog.

SIMBAD	ΔMag	P	T0	Apsidal	Multi_P	HB	e	ET	ST1	ST2
2MASS J16542949-4139149	0.182	6.34877	1633.56460		1	0	0	EA2	*	
HD 114026	0.230	2.1620	2334.09192		0	0	0	EA2	B0.5 V:n	
CPD-58 2608A	0.052	2.23284	2331.83340	1:	1:	0	1	EA2	*	*
V* V1153 Cen	0.557	5.979	2335.72810		0	0	1	EA2	*	
V* V1765 Cyg	0.164	13.3724	2794.57244		1	1	1	EA2	B0.5Ib	B2:V:
CD-27 4726	0.120	7.9587	1498.98070		0	1:	1:	EA1	*	
HD 306096	0.304	5.38300	1574.47920		0	1	1	EA2	B0	
V* GN Nor	0.559	5.703	1626.08130		0	1	1	EA2	A0 V: [tw]	
V* V1103 Cas	0.566	6.178	1790.53260		0	0	1	EA2	B0	
CD-59 3165	0.240 / 0.015:	7.59370 / 3.18206	1573.18250 / 1616.16205		0 / 0	0 / 0	1 / 0	EA2 / EA2	*	
V* CE CMa	0.638	27.0729	2247.82650		0	0	1	EA2	*	
HD 52504	0.381	1.42147	2225.87947		0	0	0	EA2	B1: V:	-
V* V646 Cas	0.471	6.16200	2006.30329		0	0	0	EA2	B0 IV:nn	
CPD-42 2880	0.095	1.8988	1566.58619		0	0	0	EA2	O9.5-B2	
CPD-63 3284	0.167	2.872	2359.61038		1	0	0	EA2	OB	
HD 111825	0.227	2.00669	1596.80501		0	0	0	EA2	*	
CD-54 6456	0.097	16.9742	1634.97340		0	0	1	EA2	*	*
HD 102475	0.012	9.0411	2324.78323		1	0	-	EA1	*	*
HD 152219	0.192	4.24024	2364.88748		1	1	1	EA2	O9.5 III	B1-2 V-III
V* EV Vul	0.863	2.82212	2421.09141		1	0	0	EA2	*	*
V* V499 Sco	0.501	2.33329	2389.56663		0	0	0	EA2	*	*
f Vel	0.086	26.3060	2302.27932		0	1	1	EA1	O9.7 II [tw]	B0 V: [tw]
V* XZ Cep	0.863	5.0973	1982.06212		0	0	0	EA2	B1.5 II-III	B1.1 III-V
BD+66 1675	0.029	2.71564	1768.18230		1	1:	1:	EA1	O8 V	B
BD+55 2722	0.036	2.00453	2881.12965		1	0	0	EA2	O7 Vz(n)	B

Note: Summarized version of the YMDB catalog for unconfirmed systems (candidates). Presented in the same format as Table 4.1.2

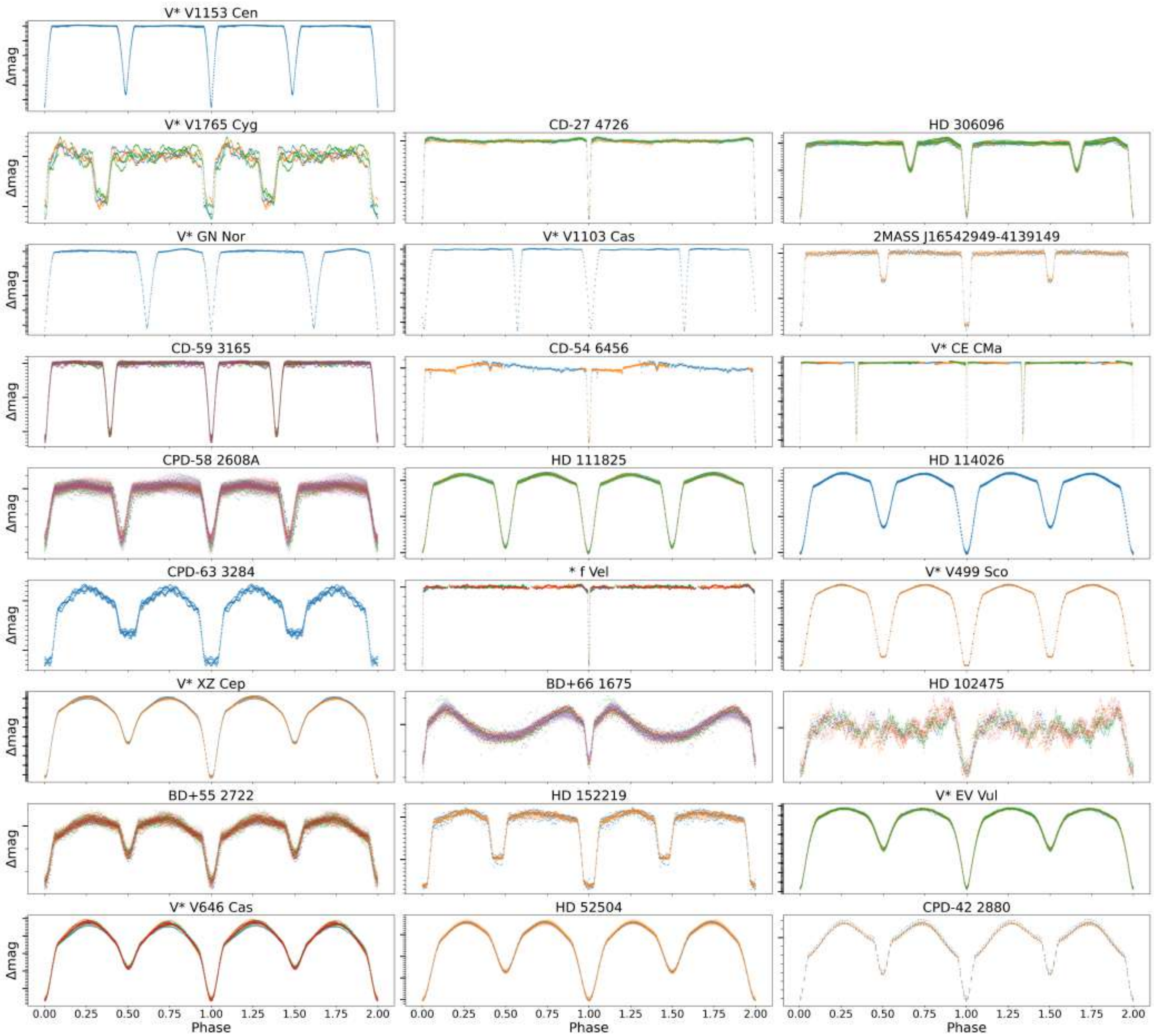

Figure 4.1.6: Light curves belonging to the candidate category. In each subpanel, bold, long ticks on the Y-axis denote increments of 0.1Δmag, and thin, short ticks indicate increments of 0.01Δmag.

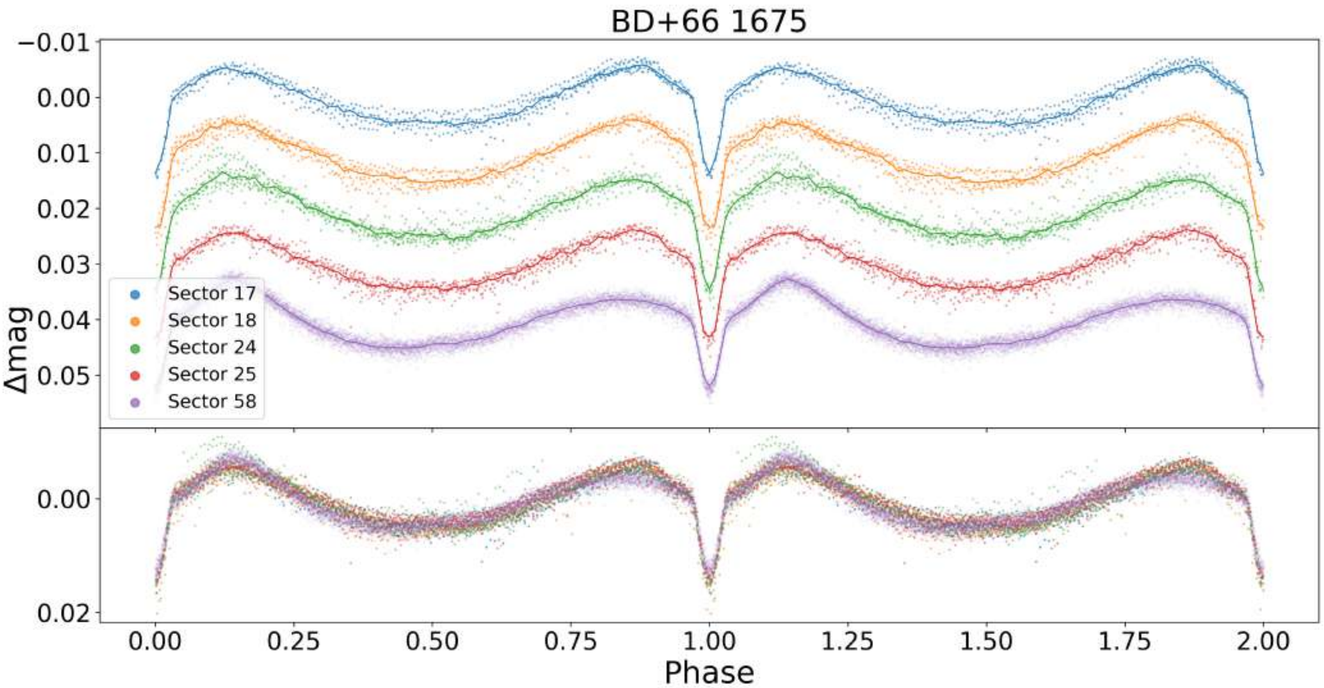

Figure 4.1.7: Light curves of BD+66 1675. The top panel displays each reduced TESS sector separated by an artificial 0.01 Δ Mag for visibility. The composite LC is shown in the bottom panel. Sectors from 17 to 58 span 1150 days of observation. A heartbeat-like feature is present before the eclipse in the earliest sector (17), while the same feature is visible after the eclipse by the latest sector (58).

CD-27 4726: This system is a well-known detached eclipsing binary (DEB). TESS data reveal an asymmetric increase in brightness just before and after the primary eclipse, reminiscent of the heartbeat signal observed in the very massive binary system WR 21a (Barbá et al., 2022). Unluckily, the spectral type of this DEB is not completely reliable thus, we add CD −27 4726 to the candidates list.

***f Vel**: It is a studied DEB system; however, as far as we are aware, its heartbeat phenomenon has not been documented.

CD-59 3165: It is recognized as a highly eccentric DEB (Kim et al., 2018). In the TESS data, in addition to exhibiting double-eclipsing behavior, it also displays other eclipses with a periodicity of 3.18205 d (see Fig. 4.1.8). Given that this star is identified as a double in the WDS catalog (WDS J10348-6013AB), with both stars separated by only 2.3 arcseconds (Mason et al., 2001), we can not definitively confirm the origin of these additional eclipses. However, our analysis of two spectra obtained during opposite quadratures of the main DEB system as part of the OWN Survey program reveals distinct spectral features for each component. One component exhibits narrow lines, while the other shows broader lines. The ratio of Si III λ4552 to Si IV λ4089 is nearly unity in the narrow component, suggesting a spectral type of B0.5. Conversely, this ratio is smaller in the broader component, and considering the absence of He II λ4542, yield a spectral type of B0-0.2. In terms of luminosity class, the narrow component appears to belong to classes III-I, as He II λ4686 is markedly fainter than He I λ4713. Conversely, both lines are comparable in the broad component, indicative of a class V classification. In Fig. 4.1.9 we show some spectral regions to illustrate these classifications. In the future, we plan to conduct a more targeted spectral analysis to identify the spectral signatures of both components of the other DEB system. This analysis will also aim to elucidate the source of the additional eclipses observed.

HD 306096: It is also a very studied DEB, but we note a clear heartbeat feature on the orbital phases where the periastron passage is expected.

HD 102475: We found no evidence in the existing literature suggesting that it is a binary or variable star. It is only mentioned in general works on spectral types (Feast et al., 1961; Houk & Cowley, 1975), where it is classified as B0.5 II and B1 III, respectively. Therefore, we include this target as a candidate until its spectral type is confirmed with modern spectroscopic analysis. It also exhibits short-period variability, interpreted as pulsations.

HD 114026: While we found no evidence suggesting variability, Garrison et al. (1983) identified it as a probable SB2 system. Despite its spectral classification exhibiting significant dispersion, ranging from OB to B2, with Garrison et al. (1983) designating it as a B0.5 V:n type, we prefer to be cautious and include HD 114026 as a candidate for the YMDB.

CPD −63 3284: This star lacks a reliable spectral classification, and unfortunately, we were unable to observe it during our run at CASLEO. Initially identified as an OB star by Lynga (1964), no additional classification information was found. Nevertheless, its LC unmistakably displays double eclipses, which indeed correspond to occultation and transit events. It also exhibits short-period variability, interpreted as pulsations. We include it as a candidate in the YMDB.

V* GN Nor: This is another well-known system; however, its heartbeat has not been reported to the best of our knowledge.

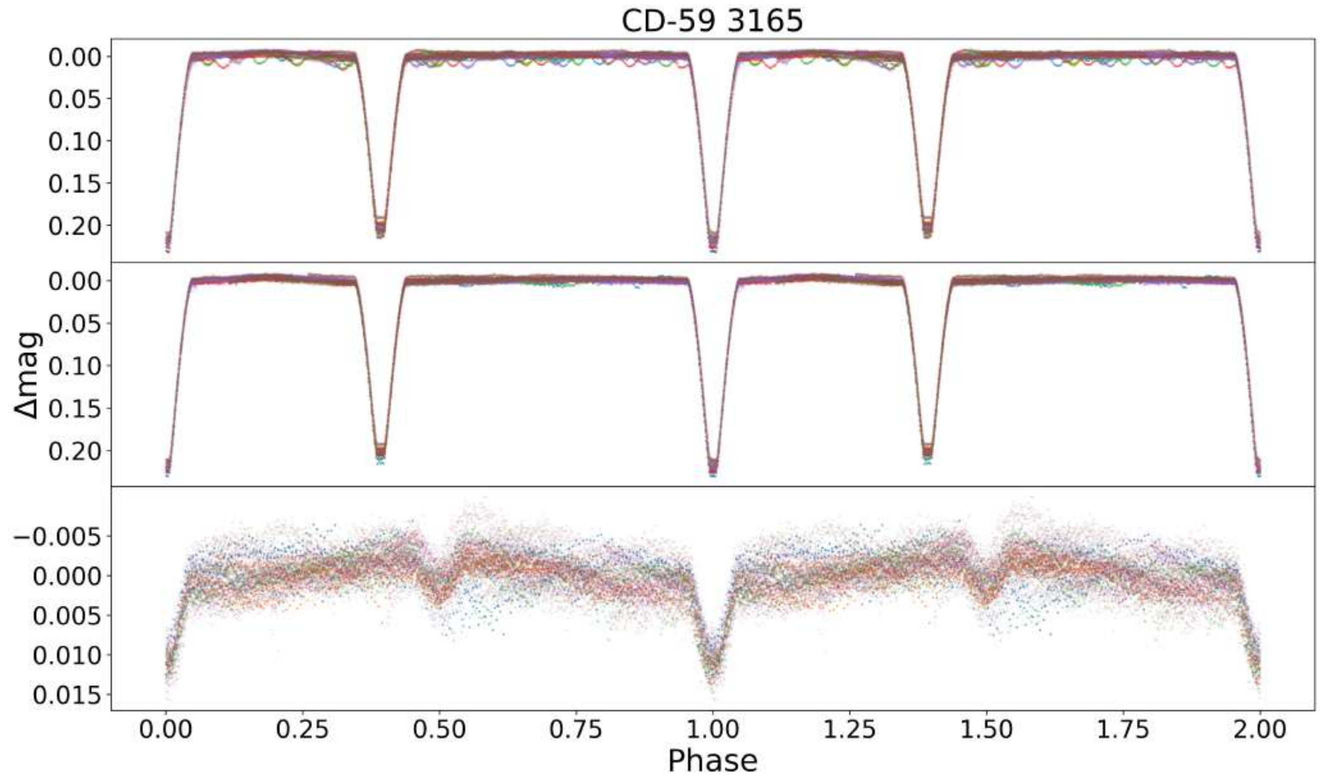

Figure 4.1.8: Light curves of CD-59 3165. The top panel displays the composite LC. The middle panel illustrates the LC for the system with a period of 7.59 days, while the bottom pannel shows the system with a period of 3.18 days. Each color represents a different sector of TESS

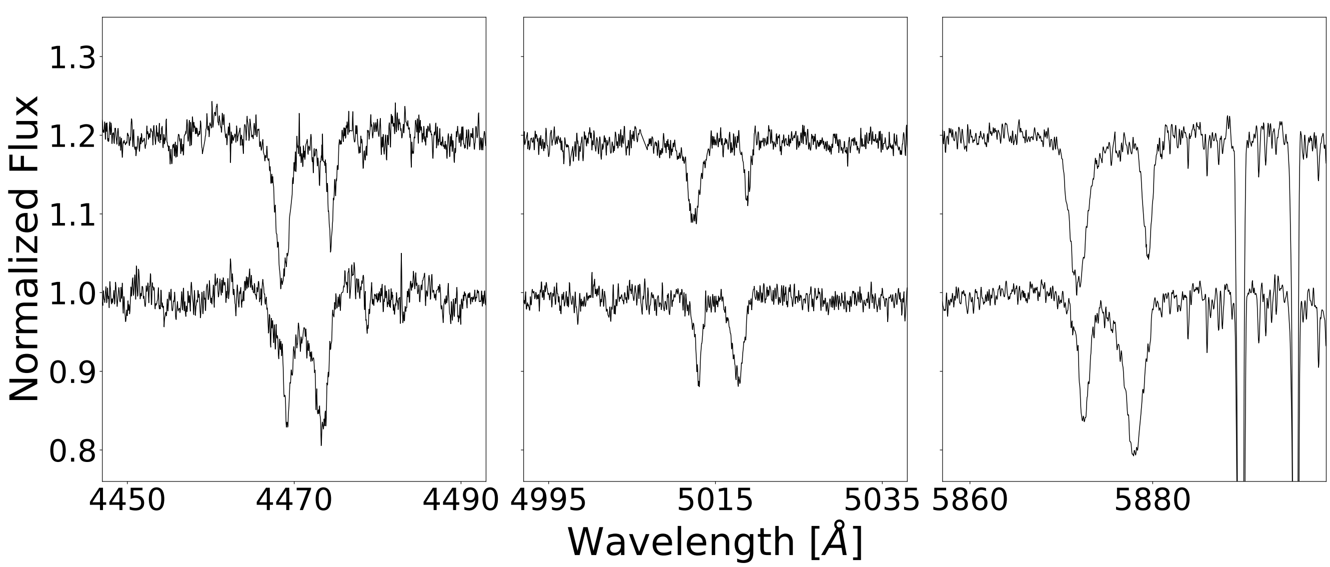

Figure 4.1.9: Three wavelength regions, around selected He I absorption lines of two spectra of CD -59 3165 obtained during quadratures.

CD −54 6456: Prior to this study, there were no records indicating variability or binarity for this system. Classified as O9.5 V (Sota et al., 2014), our analysis involved six high-resolution spectra, which revealed no RV variations in the features of the O-type star. Consequently, this suggests that the eclipsing binary likely involves another stellar pair within the TESS pixel or is indistinguishable from CD −54 6456. For this reason, we have included it as a candidate in the YMDB.

BD +55 2722: This system is, indeed, a Trapezium-like configuration with components named A (O8 Vz), B (O9.5 V), and C (O7 V(n)z+B), according to the GOSSS (Maíz Apellániz et al., 2016). Given that the three sources are indistinguishable in TESS data, we attribute the DEB discovery to the C component, thereby designating BD +55 2722 C as a candidate in the YMDB. This classification stands until the spectral type of the secondary component is more precisely determined.

4.1.3 Unqualified

A total of 32 systems were deemed unqualified for inclusion in the YMDB catalog due to one or both of the following reasons: (1) their light curves exhibit nondetached behavior (i.e., EB or EW-type variability), indicating significant interaction between their components, or (2) their spectral classifications fall outside the O9–B1 range or exceed the permitted dispersion in luminosity class (IV–V), making them unsuitable for this catalog. While these systems are excluded from the final YMDB selection, some may still be of interest for separate studies, particularly those displaying unique variability or evolutionary signatures. Table 4.1.4 lists these systems along with their defining characteristics, and Figure 4.1.10 shows their corresponding TESS light curves. Below, we describe notable cases where either new spectral classifications were determined, or specific rejection criteria provide further insight into their stellar nature.

HD 277878: Despite extensive literature search, no evidence of photometric variability was found for this target. Originally identified as an OB or B0-type star, it was recently reclassified as O7 V((f))z based on LAMOST spectra (Li, 2021), and indicated as SB1. Consequently, we have excluded it from consideration in the YMDB.

LS V +38 12: This star was identified as a binary system, based on spectroscopic observations, by Maíz Apellániz et al. (2016), who classified the pair as O7 V((f))+ B0 III-V. Initially considered for inclusion in the YMDB. However, subsequent analysis of the TESS data revealed that they are contact binaries, leading to their rejection.

*** psi02 Ori**: It is a widely recognized spectroscopic binary (Plaskett, 1908; Lu, 1985), and also known to exhibit ellipsoidal variations (Avvakumova et al., 2013). In the TESS data, its double-eclipsing nature is clearly evident, alongside the ellipsoidal variations. However, due to its spectral type being identified as B1 III + B2 V (Lu, 1985), we have excluded it from consideration in the YMDB.

HD 305850: It is listed as a pulsating star in Simbad, yet we found no references to its periodicity or LC. Moreover, its spectral type is actually uncertain, requiring an accurate determination. Initially considered for inclusion in the YMDB. However, subsequent analysis of the TESS data revealed that they are contact binaries, leading to their rejection.

Table 4.1.4: Unqualified systems for the YMDB catalog.

SIMBAD	ΔMag	P	T0	Apsidal	Multi_P	HB	e	ET	ST1	ST2
V* AC Vel	0.442	4.562	2284.25847		0	0	0	EA2	B2 V ^{tw}	
HD 52533	0.447	21.9648	1501.65900		0	0	1	EA2	O8.5IVn	
23 Ori	0.039	4.55520	1470.80658		1	0	0	EA2	B2 IV/V	*
HD 309018	0.052:	0.89216	2358.72842		0	0	1	EA2	O8.5 V ^{tw}	
HD 144918	0.059	1.27913	1625.75646		0	0	0	EA2	O8 V ^{tw}	*
V* V340 Mus	0.076	3.42725	1597.38243		1	0	0	EA2	O9 IV	*
V* FM CMa	0.239	2.78940	1509.69900	1	0	0	0	EA2	B2 IV ^{tw}	B3 V: ^{tw}
V* ET Vel	0.657	3.08090	1519.76470		0	0	1	EA2	B2.5 V ^{tw}	
HD 305850	0.086	2.3810	1620.65763		0	0	0	EB2	*	
V* V1082 Sco	0.402	23.4465	1637.81050		1	0	1	EA2	B0.5Ib	O9.5 III
HD 99630	0.214	21.1220	1602.84699		0	0	1	EA2	B4-B5	
UCAC2 5911156	0.189	8.6715	2379.81580		1	0	-	EA1	B0.5 III ^{tw}	
CD-53 6352	0.034	2.48610	1630.08061		1	0	0	EA2	O7III (for component A)	
CPD-64 1885	0.292	5.13930	1600.42950		0	0	0	EA2	B4-B6	
HD 277878	0.019	0.82253	2934.44773		1:	0	0	EA2	O7 V((f))z	
CD-59 5583	0.149	8.7060	2387.67312		1	1	1	EA2	B0II	
HD 338961	0.186	1.70970	2793.63189		0	0	0	EA2	B0.5 Illnn	
V* V1216 Sco	0.499	3.92060	2389.62316		1	0	0	EA:2	B0.5III	
V* V421 Pup	0.137	5.41650	1500.20265		1	0	0	EA2	B1II	
HD 103223	0.332	2.54155	2358.08085		0	0	0	EA2	B2.5 V ^{tw}	
V* V1290 Sco	0.116	4.49260	1627.90670		1	0	0	EA2	O9.7 III	*
V* V4386 Sgr	0.231	10.802	1664.15850		1	0	0	EA2	B0.5 III ^{tw}	*
HD 142152	0.139	5.68640	1626.34840	1	1	1	1	EA2	B0 III ^{tw}	*
HD 37737	0.119	7.85199 / 1/10P / 3P	1821.42367		1	1	1	EA2	O9.5II-III(n)	*
V* V399 Pup	0.204	3.91019	2276.30939	1	0	1	1	EA2	B2 II	*
V* CC Cas	0.145	3.3670	1818.57209		1	0	0	EA2	O8.5III(n)((f))	*
V* MN Cen	0.587	3.48915	2359.82698		0	0	0	EA2	B1.5 V ^{tw}	*
V* V877 Cen	0.636	5.35857	2355.76939		0	0	0	EA2	B1III(n)	*
psi02 Ori	0.037	2.52596	2199.90592		1	0	1	EA2	B1 III	B2 V
u Her	0.663	2.05102	2767.92462		0	0	0	EA2	B2 IV	B8 III
LS V +38 12	0.053	1.42287	1837.24509		0	0	0	EB2	O7 V ((f))	B0III- V
HD 185780	0.024	3.51160	2822.28161		1	0	0	EA2	B0 III	*

Note: Summarized version of the YMDB catalog for unqualified systems. Presented in the same format as Table 4.1.2

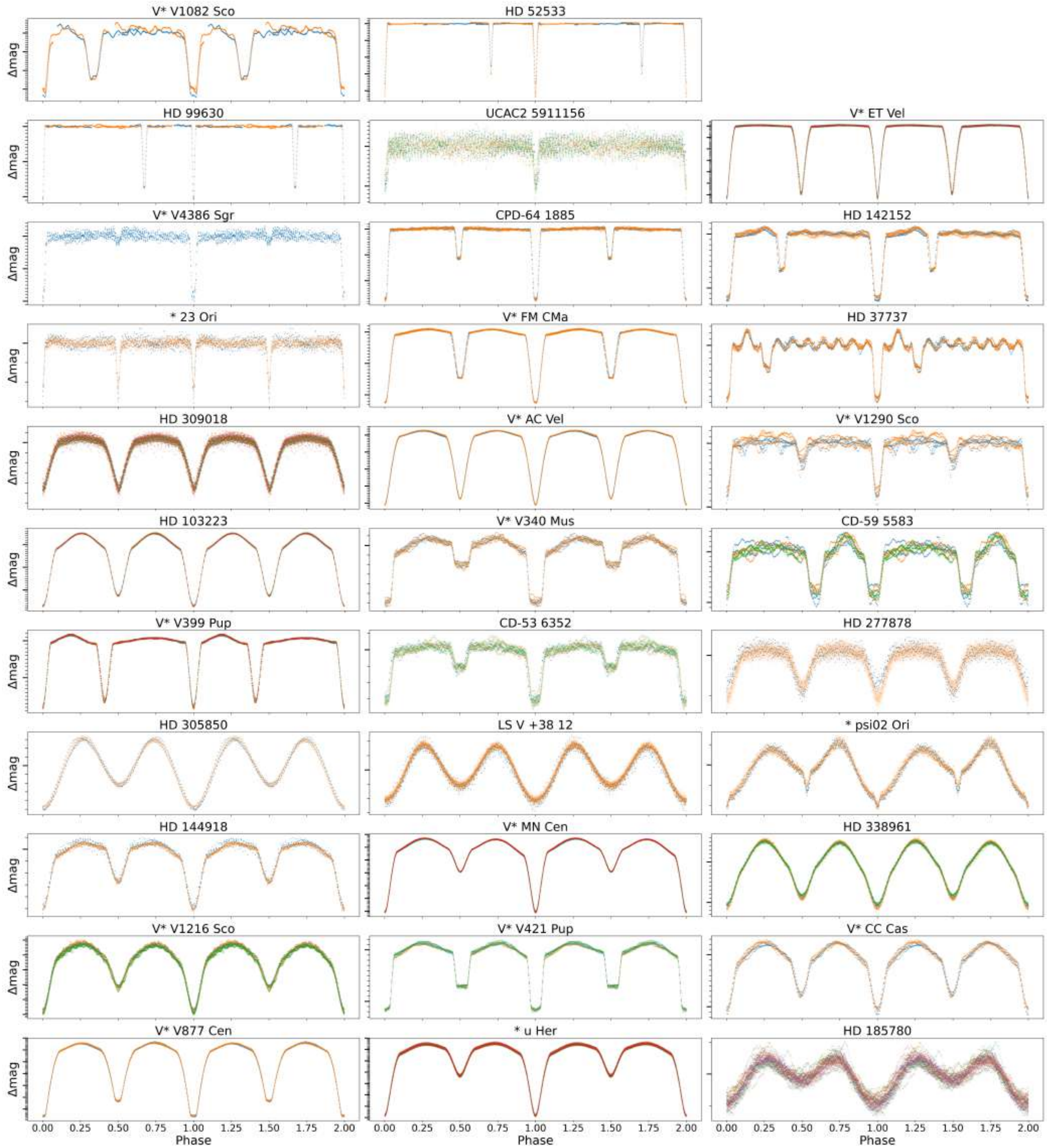

Figure 4.1.10: Light curves belonging to the unqualified category. In each subpanel, bold, long ticks on the Y-axis denote increments of $0.1\Delta mag$, and thin, short ticks indicate increments of $0.01\Delta mag$.

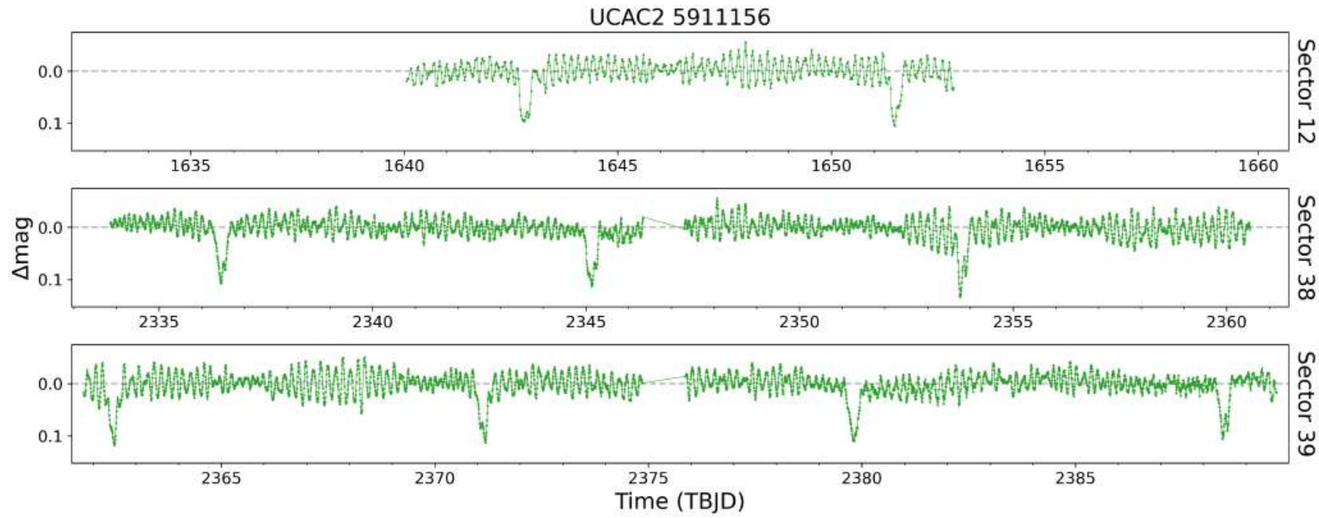

Figure 4.1.11: Light curves of UCAC2 5911156. Panels top to bottom show the unfolded LCs of Sectors 12, 38, and 39 respectively. All panels maintain equal Y and X axis scales. This system exhibits pronounced Tidally Excited Oscillations (TEOs) in each sector, reflecting oscillations in the star or system caused by tidal interactions with a nearby stellar companion.

HD 99630: This star is known as DEB, but its periodicity is badly reported in the literature (Pojmanski, 1998; Alfonso-Garzón et al., 2012). Our analysis of the TESS LC reveals that its period is nearly double the previously reported value. Additionally, it shows double eclipses and high eccentricity. Our high-resolution spectra, obtained during the OWN Survey campaigns, indicate its spectral type is earlier than the B4-B5 determined by Loden et al. (1976). The ratio between He I λ4471 and Mg II λ4481 lines is greater than three, and C II λ4267 is identified, thus a B3-type is more suitable. The weakness of the metal lines confirms its dwarf class, B3 V.

UCAC2 5911156: Initially recognized as an early-type star by Muzzio & Orsatti (1977) and subsequently classified as B0.5 V (Bassino et al., 1982), we acquired a new spectrum leading to a reclassification of its luminosity class to III. This adjustment is based on the almost similar intensities of the absorption lines He I λ4387 and Si III λ4552. The giant nature of UCAC2 5911156 naturally explains the pulsations noted in the LC shown in Fig.4.1.11. The LC exhibits eclipses with a superimposed set of oscillations forming a beating pattern, akin to those initially discovered in HD187091 (Welsh et al., 2011; Thompson et al., 2012, and references therein). Notably, these damped oscillations do not align with the orbital period, as the maximum amplitudes do not occur at the same phase. To the best of our knowledge, this is the first identification of the system as a DEB and pulsating. However, a detailed analysis of this intriguing system is beyond the scope of this work.

HD 142152: Initially classified as a B0 III massive star by Crampton (1971) and subsequently confirmed by Houk & Cowley (1975), HD 142152 lacked published spectra. To address this absence, we observed this target using CASLEO and confirmed its spectral classification (see Fig. 3.3.1). The identification as a probable binary arises from two discrepant radial velocities reported by Crampton (1972). The TESS LC distinctly illustrates a highly eccentric detached double-eclipsing behavior. Additionally, pulsation-like variations, occurring with 1/8 of the orbital periodicity, and a discernible heartbeat feature are detected. This renders the target exceptionally interesting, despite its exclusion from YMDB due to its luminosity class.

CD-53 6352: This star is recognized as double or multiple according to the Washington Double Star Catalog (WDS J16001-5355AB), but no photometric or RV variability has been identified. Analysis of TESS data has not conclusively determined whether star A or B is the DEB. While component A is classified as O7 III (Vijapurkar & Drilling, 1993), the spectral classification for component B is unavailable. As such, we have included it as a candidate in the YMDB. Additionally, its LC exhibits short-period variations compatible with pulsations.

HD 144918: This target exhibits one of the most widely scattered spectral type assignments in the literature, ranging from O5/7 (Houk, 1978) to B0 (Cannon & Pickering, 1921), with none originating from a modern study. Consequently, we decided to acquire a new spectrum. The CASLEO spectrum is classified as O8 V, with this classification based on the observation that He II λ4542 is slightly fainter than He I λ4471. Concerning its binary nature, it is reported as SB2 by Feast & Thackeray (1963), yet no period is provided, and no dedicated work was found in the literature.

HD 338961: No evidence of variability or binary nature was found for this star in the literature consulted. Despite some dispersion in its spectral classification, we consider the determination B0.5 IIInn from (Turner, 1980) to be reliable. Therefore, we have excluded it from inclusion in the YMDB.

Chapter 5

Concluding Remarks and Future Perspectives

This thesis presents a detailed framework for understanding massive stars, their spectral classification, the mass discrepancy problem, and the determination of absolute parameters using detached spectroscopic binaries. Through a combination of theoretical analysis, observational data, and numerical modelling, we have aimed to refine our understanding of the fundamental properties of massive stars and address key uncertainties in their evolutionary paths.

One of the primary contributions of this research is addressing the long-standing mass discrepancy problem, which highlights the inconsistencies between observationally derived dynamical masses and theoretical predictions from stellar evolutionary models. By assessing the role of convective core overshooting, mass-loss rates, rotational mixing, and magnetic fields, we have shown the complexity of these discrepancies and the necessity of high-precision empirical data for model calibration. Detached spectroscopic binaries remain one of the most reliable tools for deriving accurate stellar parameters, offering critical constraints for theoretical models.

The development and application of spectroscopic and photometric modelling techniques, particularly through the use of PHOEBE, have further solidified our ability to determine absolute parameters with high precision. We have shown how different observational constraints—light curves and radial velocity measurements—interplay to yield robust determinations of mass, radius, effective temperature, and luminosity. The extensive discussion on parameter extraction based on different combinations of observational scenarios provides a valuable framework for future studies and observational campaigns.

Furthermore, this work reinforces the importance of spectral classification in understanding stellar evolution. The comprehensive analysis of O and B-type spectral features, along with their implications for stellar wind properties, ionization states, and mass-loss rates, contributes to the broader field of stellar astrophysics. Spectral classification remains a cornerstone for interpreting stellar populations, constraining theoretical models, and improving simulations of stellar atmospheres.

The results presented in this thesis have significant implications for multiple areas of astrophysics. The improved characterization of massive stars contributes to a better understanding of their role in galactic chemical evolution, feedback processes, and the formation of compact remnants such as neutron stars and black holes. Additionally, resolving the mass discrepancy problem has direct consequences for studies involving binary population synthesis, supernova progenitors, and the initial mass function.

Future work should continue expanding the sample of well-characterized detached spectroscopic binaries, particularly within the B0.5V spectral type, where empirical constraints remain scarce. Incorporating high-resolution spectroscopy, interferometric observations, and advancements in stellar atmosphere models will further refine our understanding of massive star evolution. Moreover, continued improvements in computational techniques and the integration of machine-learning approaches into binary modelling frameworks may provide new pathways for tackling unresolved questions in stellar astrophysics.

In conclusion, this thesis highlights the power of empirical studies in validating and improving theoretical models of stellar evolution. By leveraging the precision of detached spectroscopic binaries and integrating observational data with advanced modelling techniques, we take a step forward in resolving longstanding uncertainties in massive star astrophysics. These advancements not only enhance our understanding of individual stellar objects but also contribute to broader astrophysical questions, from the chemical enrichment of galaxies to the progenitors of compact remnants and gravitational wave sources.

5.1 Future work

5.1.1 Public Release of the TESS Light Curve Pipeline

The semi-automatic pipeline developed during this doctoral thesis for extracting and analyzing TESS light curves is intended to be enhanced, calibrated, and published, making it publicly available to the community. Written in Python, this pipeline automates several key steps in light curve construction, including the creation of quality masks to exclude contamination, the generation of target masks tailored to specific stars, and the careful selection and normalization of data to ensure reliability. Innovative methods for detrending systematics, such as Phase-Synchronized Polynomial Fitting (PSPF), which leverages orbital periods to isolate and correct for instrumental noise while preserving astrophysical signals, are also incorporated. By making this tool accessible, researchers will be empowered to efficiently extract and analyze TESS data, facilitating discoveries across a broad range of astrophysical studies.

5.1.2 Expanding the YMDB Catalogue

The next phase of this project focuses on determining the absolute parameters of the confirmed systems in the YMDB Catalog. A thorough review of the 30 confirmed stars in the catalog has been completed. Currently, absolute parameter determination is underway for 8 systems (labelled as 1 in the 'Paper' column of Table 5.1.1), which already have existing radial velocity data available. For these systems, the only remaining step is performing PHOEBE-II iterations to derive the final stellar parameters. This methodology follows the same approach applied to KU Car (Martín-Ravelo et al., 2021) and WR21a (Barbá et al., 2022). For an additional 5 systems (labelled as 2 in Table 5.1.1), no published radial velocity orbit exists; however, sufficient public spectroscopic data is available to derive RV measurements (see

Appendix A). In particular, the high-resolution spectroscopic library LiLiMaRlin (Maíz Apellániz et al., 2019a) provides a valuable resource for extracting RVs, enabling precise orbital parameter determinations without requiring new observations.

The remaining 16 systems (labelled as 3 and 4) require additional spectroscopic data before orbital solutions can be determined. Notably, * eta Ori (labelled as 0) has already been extensively studied and does not require further analysis. Observational proposals will be submitted to obtain high-resolution spectra for these remaining systems, as well as for the 25 candidate systems listed in Table 4.1.3, which require spectroscopic confirmation to determine their membership in the YMDB Catalog.

The highest priority moving forward is the completion of the PHOEBE-II modelling for systems classified as 1 in Table 5.1.1, as these have sufficient RV and photometric data for immediate analysis. Figures 5.1.1 illustrate these systems, showing both our extracted LCs and the published RV curves, which will serve as the foundation for our PHOEBE-II modelling efforts. Once these models are finalized, RVs will be extracted from existing spectra for systems classified as 2, while new observational proposals will be pursued for systems requiring additional spectroscopic data, ensuring the progressive completion of the YMDB Catalog.

5.1.3 Spectroscopic Follow-Up of YMDB Understudied Systems

For the 16 YMDB systems requiring spectroscopic follow-up, proposals will be submitted to obtain high-resolution spectra and complete their orbital solutions. Nine of these systems will be included in a proposal for the 2025B Semester, while the remaining 7, visible only during Semester A, will be targeted in a proposal for 2026A. Based on target visibility, 9 systems will be observed from the South using Gemini/GHOST and SOAR/Goodman, while 3, visible only from the North, will be observed with NEID and GMOS-N. The remaining 4 systems, accessible from both hemispheres, offer scheduling flexibility and will be observed from either side. Once spectroscopic data are obtained and radial velocity solutions are derived, absolute parameters will be determined, with results expected to be published in two separate papers as data become available.

5.1.4 Expanding to Earlier Spectral Types

As an extension of this thesis, the YMDB methodology is envisioned to be expanded to systems with earlier spectral types (O7–O9) than those currently in the catalog. Although these stars have been more extensively studied than their massive siblings of later spectral types (explored in this thesis), the mass discrepancy problem remains highly relevant. Unique challenges, such as extreme mass loss through stellar winds, necessitate the calibration of specific evolutionary models. A proposal for this work was submitted in 2020 and was granted observing time through the OWN collaboration until the end of 2021. Although the project was put on hold, two years' worth of data remain unanalyzed, presenting a valuable opportunity. This project is intended to be revisited, either through direct involvement or by supervising a student to carry it forward.

Table 5.1.1: Summary of confirmed systems in YMDB, their observational status, and required data.

SIMBAD	Culminates	Dec	Visibility	Paper	Sp. Data	RV Data
* eta Ori	Dec 13	-2.40	Both	0	828	FALSE
V* VV Ori	Dec 15	-1.16	Both	1	106	TRUE
HD 152218	Jun 03	-41.71	South	1	69	TRUE
V* NY Cep	Sep 02	63.08	North	1	30	TRUE
V* Y Cyg	Aug 02	34.66	North	1	26	FALSE
V* AH Cep	Aug 30	65.06	North	1	15	TRUE
del Pic	Dec 24	-54.97	South	1	6	TRUE
LS VI +00 25	Jan 03	0.38	Both	1	2	TRUE
V* DW Car	Mar 02	-60.04	South	1	0	TRUE
BD+66 1674	Sep 23	67.43	North	2	27	
V* HH Car	Mar 05	-59.45	South	2	22	TRUE
HD 99898	Mar 14	-62.93	South	2	22	
V* KU Car	Mar 01	-58.67	South	2	19	
V* V1295 Sco	Jun 03	-41.42	South	2	11	TRUE
HD 204827	Aug 11	58.74	North	3	6	
HD 93683	Mar 03	-60.62	South	3	5	
Schulte 27	Jul 28	41.29	North	3	4	
V* V404 Vel	Feb 04	-48.83	South	3	4	
CD-35 4470	Jan 25	-36.21	Both	3	3	
V* V725 Car	Mar 02	-59.49	South	3	3	
RAFGL 5223	Jan 08	-4.32	Both	4	1	
HD 278236	Dec 13	40.55	North	4	0	
HD 298448	Feb 11	-52.98	South	4	0	
HD 309036	Mar 18	-63.38	South	4	0	
HD 338936	Jul 16	24.63	Both	4	0	
TYC 8174-540-1	Feb 10	-49.84	South	4	0	
V* IK Vel	Feb 06	-53.21	South	4	0	
V* V1208 Sco	Jun 03	-41.86	South	4	0	
V* V346 Cen	Mar 17	-62.43	South	4	0	
CD-28 5257	Jan 21	-28.84	Both	4	0	

Note: The Paper column classifies the systems as follows: 0 - well-studied, no further analysis needed; 1 - published RV orbital solution, requiring PHOEBE fitting; 2 - spectra available, RVs yet to be extracted; 3 - limited spectra; 4 - insufficient spectra. Sp. Data represents spectroscopic data availability from public archives (AAT, SnE, ESO, GOSC, LAMOST) or from the OWN survey and privately held collaboration data. RV Data indicates whether radial velocity data is available (TRUE) or missing (FALSE).

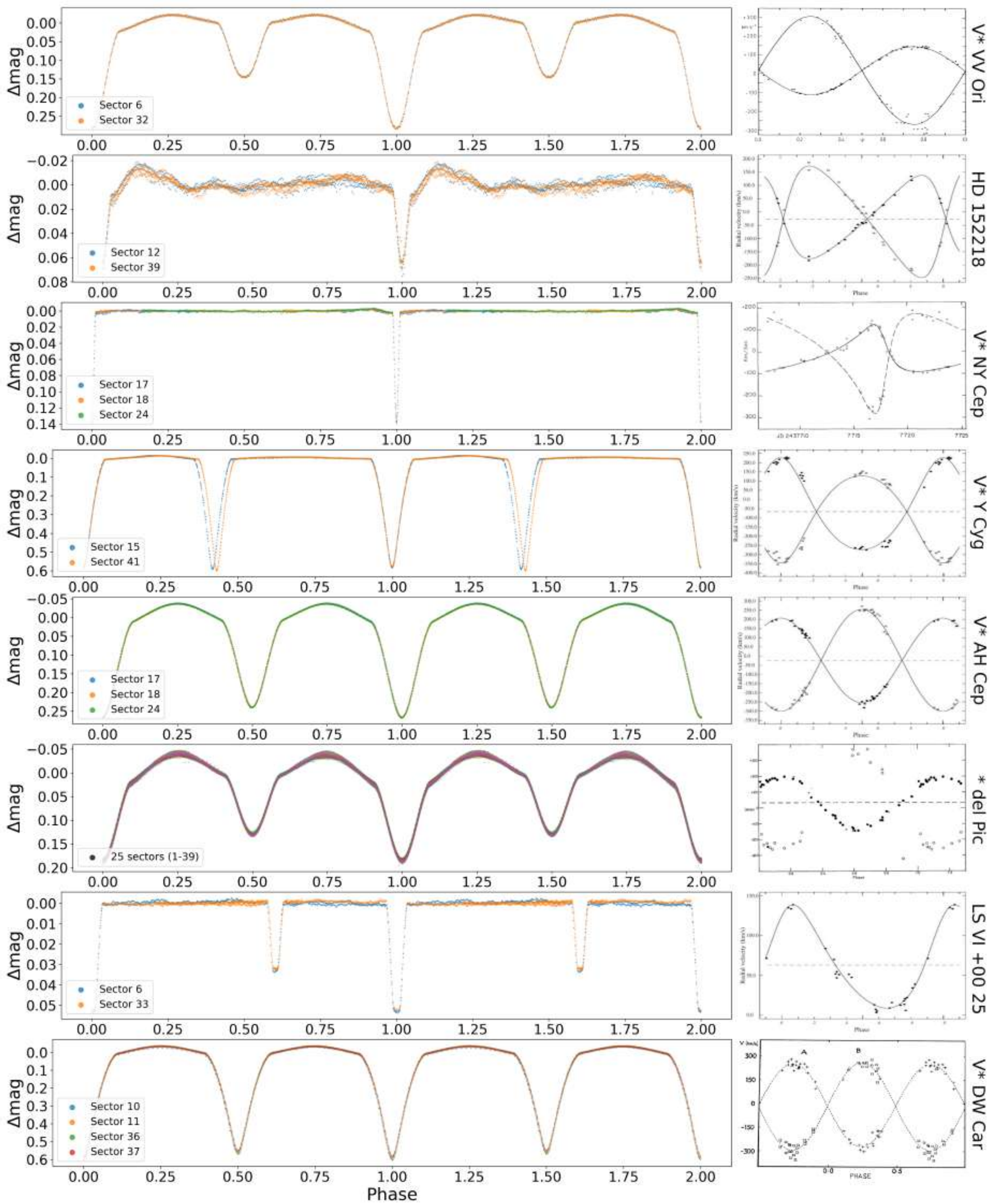

Figure 5.1.1: Light curves and radial velocity curves for the eight systems labelled as 1 in the "Paper" column of Table 5.1.1. Each row corresponds to one system, with the left panel displaying the phase-folded LC obtained from our analysis Martín-Ravelo et al. (2024) and the right panel showing the published RV curve from the literature. The RV sources are as follows: V* VV Ori from Duerbeck (1975); HD 152218 from Stickland et al. (1997); V* NY Cep from Heard & Fernie (1968); V* Y Cyg and V* AH Cep from Burkholder et al. (1997); * del Pic from Thackeray (1966); LS VI +00 25 from Munari & Tomasella (1999); and V* DW Car from Ferrer et al. (1985).

Bibliography

Albrecht S., Winn J. N., Carter J. A., Snellen I. A. G., de Mooij E. J. W., 2011, ApJ, 726, 68

Alexander M. J., Hanes R. J., Povich M. S., McSwain M. V., 2016, AJ, 152, 190

Alfonso-Garzón J., Domingo A., Mas-Hesse J. M., Giménez A., 2012, A&A, 548, A79

Avvakumova E. A., Malkov O. Y., Kniazev A. Y., 2013, Astronomische Nachrichten, 334, 860

Bakış H., Köseoglu D. T., Bakış V., Nitschelm C., Eker Z., 2021, MNRAS, 503, 2432

Balona L. A., 1983, MNRAS, 203, 1041

Balona L. A., Engelbrecht C. A., 1985, MNRAS, 212, 889

Banyard G., Sana H., Mahy L., Bodensteiner J., Villaseñor J. I., Evans C. J., 2022, A&A, 658, A69

Banyard G., et al., 2023, A&A, 674, A60

Barbá R. H., Gamen R., Arias J. I., Morrell N. I., 2017, in Eldridge J. J., Bray J. C., McClelland L. A. S., Xiao L., eds, Vol. 329, The Lives and Death-Throes of Massive Stars. pp 89–96, doi:10.1017/S1743921317003258

Barbá R. H., Gamen R. C., Martín-Ravelo P., Arias J. I., Morrell N. I., 2022, MNRAS, 516, 1149

Bareilles F., 2017, GBART: Determination of the orbital elements of spectroscopic binaries, Astrophysics Source Code Library, record ascl:1710.014

Bassino L. P., Dessaunet V. H., Muzzio J. C., Waldhausen S., 1982, MNRAS, 201, 885

Batten A. H., 1973, Binary and multiple systems of stars

Bertiau F. C., Grobben J., 1969, Ricerche Astronomiche, 8, 1

Bidelman W. P., 1984, Information Bulletin on Variable Stars, 2514, 1

Bodensteiner J., Shenar T., Sana H., 2020, A&A, 641, A42

Borkovits T., Rappaport S. A., Toonen S., Moe M., Mitnyan T., Csányi I., 2022, MNRAS, 515, 3773

Budding E., et al., 2024, MNRAS, 527, 6389

Burkholder V., Massey P., Morrell N., 1997, ApJ, 490, 328

Böhm-Vitense E., 1997, Introduction to Stellar Astrophysics: Volume 2: Stellar Atmospheres. Cambridge University Press, https://www.cambridge.org/us/universitypress/subjects/physics/astrophysics/introduction-stellar-astrophysics-volume-2?format=PB

Cannon A. J., Pickering E. C., 1921, Annals of Harvard College Observatory, 96, 1

Cannon A. J., Pickering E. C., 1993, VizieR Online Data Catalog: Henry Draper Catalogue and Extension (Cannon+ 1918-1924; ADC 1989), VizieR On-line Data Catalog: III/135A. Originally published in: Harv. Ann. 91-100 (1918-1924)

Cantiello M., et al., 2009, A&A, 499, 279

Castelli F., Kurucz R. L., 2004, A&A, 419, 725

Chen T. X., et al., 2022, ApJS, 260, 5

Chini R., Hoffmeister V. H., Nasseri A., Stahl O., Zinnecker H., 2012, MNRAS, 424, 1925

Claret A., 2000, A&A, 363, 1081

Claret A., 2004, A&A, 428, 1001

Claret A., Bloemen S., 2011, A&A, 529, A75

Conroy K. E., et al., 2020, ApJS, 250, 34

Corbelli E., Palla F., Zinnecker H., eds, 2005, The Initial Mass Function 50 years later Astrophysics and Space Science Library Vol. 327, doi:10.1007/978-1-4020-3407-7.

Cousins A. W. J., 1966, MNRAS, 131, 443

Crampton D., 1971, AJ, 76, 260

Crampton D., 1972, MNRAS, 158, 85

Crampton D., Fisher W. A., 1974, Publications of the Dominion Astrophysical Observatory Victoria, 14, 283

Crowther P. A., 2007, ARA&A, 45, 177

Cruz P., Aguilar J. F., Garrido H. E., Diaz M. P., Solano E., 2022, MNRAS, 515, 1416

Davenport J. R. A., Windemuth D., Warmbein K., Howard E. L., Klein C., Birky J., 2021, AJ, 162, 189

Duerbeck H. W., 1975, A&AS, 22, 19

Eaton J. A., Wu C. C., 1983, PASP, 95, 319

Ekström S., 2021, Frontiers in Astronomy and Space Sciences, 8, 53

Ekström S., et al., 2012, A&A, 537, A146

Farr W. M., Mandel I., 2018, Science, 361, aat6506

Feast M. W., Thackeray A. D., 1963, MmRAS, 68, 173

Feast M. W., Stoy R. H., Thackeray A. D., Wesselink A. J., 1961, MNRAS, 122, 239

Ferrer O. E., Niemela V. S., Méndez R. H., Levato H., Morrell N., 1985, , 10, 323

Fitzgerald M. P., Miller M. L., 1983, PASP, 95, 361

Fuller J., 2017, MNRAS, 472, 1538

Gaia Collaboration 2022, VizieR Online Data Catalog: Gaia DR3 Part 1. Main source (Gaia Collaboration, 2022), VizieR On-line Data Catalog: I/355. Originally published in: doi:10.1051/0004-63, doi:10.26093/cds/vizier.1355

Gamen R., Barbá R., Morrell N., Arias J., Maíz Apellániz J., Sota A., Walborn N., Alfaro E., 2007, Spectroscopic monitoring of Southern Galactic O and WN stars: State of the Art in 2007

Gamen R., Barbá R. H., Morrell N. I., Arias J., Maíz Apellániz J., 2008, in Revista Mexicana de Astronomia y Astrofisica Conference Series. pp 54–54

Garrison R. F., Hiltner W. A., Schild R. E., 1977, ApJS, 35, 111

Garrison R. F., Schild R. E., Hiltner W. A., 1983, ApJS, 52, 1

Georgelin Y. M., Georgelin Y. P., Roux S., 1973, A&A, 25, 337

Gies D. R., 1987, ApJS, 64, 545

Gieseking F., 1982, A&AS, 49, 673

Gimenez A., Clausen J. V., Helt B. E., Vaz L. P. R., 1986a, A&AS, 66, 45

Gimenez A., Clausen J. V., Andersen J., 1986b, A&A, 160, 310

Gray R. O., Corbally C. J., 2009, Stellar Spectral Classification. Princeton University Press, `https://press.princeton.edu/books/paperback/9780691125114/stellar-spectral-classification`

Guthnick P., Prager R., 1934, Astronomische Nachrichten, 251, 257

Guthnick P., Prager R., 1936, Astronomische Nachrichten, 260, 393

Hagedus T., 1988, Bulletin d'Information du Centre de Donnees Stellaires, 35, 15

Hansen C. J., Kawaler S. D., 1994, Stellar Interiors. Physical Principles, Structure, and Evolution.. Springer, doi:10.1007/978-1-4419-9110-2

Harmanec P., et al., 2014, A&A, 563, A120

Heard J. F., Fernie J. D., 1968, JRASC, 62, 99

Hernandez C. A., Sahade J., 1978, PASP, 90, 728

Herrero A., Kudritzki R. P., Vilchez J. M., Kunze D., Butler K., Haser S., 1992, A&A, 261, 209

Hertzsprung E., 1924, BAN, 2, 165

Hilditch R. W., 2001, An Introduction to Close Binary Stars

Hill G., Crawford D. L., Barnes J. V., 1974, AJ, 79, 1271

Houk N., 1978, Michigan catalogue of two-dimensional spectral types for the HD stars

Houk N., Cowley A. P., 1975, University of Michigan Catalogue of two-dimensional spectral types for the HD stars. Volume I. Declinations -90_ to -53_ƒ0.

Huang C. X., et al., 2020, Research Notes of the American Astronomical Society, 4, 204

Huffer C. M., Eggen O. J., 1947, ApJ, 106, 313

Hunter I., Lennon D. J., Dufton P. L., Trundle C., Simón-Díaz S., Smartt S. J., Ryans R. S. I., Evans C. J., 2008, A&A, 479, 541

IJspeert L. W., Tkachenko A., Johnston C., Garcia S., De Ridder J., Van Reeth T., Aerts C., 2021, A&A, 652, A120

Jenkins J. M., et al., 2016, in Chiozzi G., Guzman J. C., eds, Society of Photo-Optical Instrumentation Engineers (SPIE) Conference Series Vol. 9913, Software and Cyberinfrastructure for Astronomy IV. p. 99133E, doi:10.1117/12.2233418

Kallrath J., Milone E. F., 2009, Eclipsing Binary Stars: Modeling and Analysis. Springer, https://www.springer.com/gp/book/9781441906984

Khaliullin K. F., Antipin S. V., Khaliullina A. I., 2006, Astronomy Letters, 32, 772

Kholopov P. N., Samus' N. N., Kukarkina N. P., Medvedeva G. I., Perova N. B., 1981, Information Bulletin on Variable Stars, 1921, 1

Kim C. H., Kreiner J. M., Zakrzewski B., Ogłoza W., Kim H. W., Jeong M. J., 2018, ApJS, 235, 41

Kiminki M. M., Smith N., 2018, MNRAS, 477, 2068

Klare G., Neckel T., 1977, A&AS, 27, 215

Kogure T., Leung K.-C., 2007, The Astrophysics of Emission Line Stars. Springer, https://link.springer.com/book/10.1007/978-0-387-68995-1

Kołaczek-Szymański P. A., Pigulski A., Michalska G., Moździerski D., Różański T., 2021, A&A, 647, A12

Kondo Y., McCluskey G. E., Feibelman W. A., 1980, PASP, 92, 688

Kroupa P., Jerabkova T., 2021, arXiv e-prints, p. arXiv:2112.10788

Kroupa P., Gjergo E., Jerabkova T., Yan Z., 2024, arXiv e-prints, p. arXiv:2410.07311

Kumar P., Ao C. O., Quataert E. J., 1995, ApJ, 449, 294

Lamers H. J. G. L. M., Cassinelli J. P., 1999, Introduction to Stellar Winds. Cambridge University Press, https://www.cambridge.org/core/books/introduction-to-stellar-winds/6E24600EDAD99F2B7839BBA190C115C0

Landolt A. U., 1967, AJ, 72, 1094

Laur J., Tempel E., Tuvikene T., Eenmäe T., Kolka I., 2015, A&A, 581, A37

Laur J., Kolka I., Eenmäe T., Tuvikene T., Leedjärv L., 2017, A&A, 598, A108

Lee W. B., Sung E. C., Koch R. H., Hrivnak B. J., Bradstreet D. H., Corcoran M., Mitchell R. J., Blitzstein W., 1993, in Leung K.-C., Nha I.-S., eds, Astronomical Society of the Pacific Conference Series Vol. 38, New Frontiers in Binary Star Research. p. 239

Levato H., Malaroda S., 1981, PASP, 93, 714

Levato H., Morrell N., 1983, Astrophys. Lett., 23, 183

Li G.-W., 2021, ApJS, 253, 54

Lightkurve Collaboration et al., 2018, Lightkurve: Kepler and TESS time series analysis in Python, Astrophysics Source Code Library, record ascl:1812.013

Livio M., Villaver E., 2009, Massive Stars: From Pop III and GRBs to the Milky Way. Cambridge University Press, https://www.cambridge.org/us/universitypress/subjects/physics/astrophysics/massive-stars-pop-iii-and-grbs-milky-way?format=HB&isbn=9780521762632

Loden L. O., Loden K., Nordstrom B., Sundman A., 1976, A&AS, 23, 283

Lu W., 1985, PASP, 97, 428

Luger R., Agol E., Kruse E., Barnes R., Becker A., Foreman-Mackey D., Deming D., 2016, AJ, 152, 100

Luger R., Kruse E., Foreman-Mackey D., Agol E., Saunders N., 2018, AJ, 156, 99

Lynga G., 1964, Meddelanden fran Lunds Astronomiska Observatorium Serie II, 141, 1

Maíz Apellániz J., et al., 2016, ApJS, 224, 4

Maíz Apellániz J., Pantaleoni González M., Barbá R. H., Simón-Díaz S., Negueruela I., Lennon D. J., Sota A., Trigueros Páez E., 2018, A&A, 616, A149

Maíz Apellániz J., Trigueros Páez E., Jiménez Martínez I., Barbá R. H., Simón-Díaz S., Pellerin A., Negueruela I., Rodrigo Souza Leão J., 2019a, in Montesinos B., Asensio Ramos A., Buitrago F., Schödel R., Villaver E., Pérez-Hoyos S., Ordóñez-Etxeberria I., eds, Highlights on Spanish Astrophysics X. pp 420–420 (arXiv:1810.10943), doi:10.48550/arXiv.1810.10943

Maíz Apellániz J., et al., 2019b, A&A, 626, A20

Maíz Apellániz J., Negueruela I., Caballero J. A., 2024, arXiv e-prints, p. arXiv:2410.07301

Markova N., Puls J., Langer N., 2018, A&A, 613, A12

Martín-Ravelo P., Barbá H. R., Morrell N., Arias J., Gamen R., 2021, in MOBSTER-1 virtual conference: Stellar Variability as a Probe of Magnetic Fields in Massive Stars. p. 36, doi:10.5281/zenodo.5535110

Martín-Ravelo P., Gamen R., Arias J. I., Chené A.-N., Barbá R. H., 2024, A&A, 690, A306

Martins F., Palacios A., 2013, A&A, 560, A16

Martins F., Schaerer D., Hillier D. J., 2005, A&A, 436, 1049

Mason B. D., Wycoff G. L., Hartkopf W. I., Douglass G. G., Worley C. E., 2001, AJ, 122, 3466

Massey P., 2013, , 57, 14

Mathys G., 1988, A&AS, 76, 427

Mayer P., et al., 2016, A&A, 591, A129

Mellon S. N., et al., 2019, ApJS, 244, 15

Miller N. J., Maxted P. F. L., Graczyk D., Tan T. G., Southworth J., 2022, MNRAS, 517, 5129

Moffat A. F. J., Vogt N., 1975, A&AS, 20, 125

Moffat A. F. J., Fitzgerald M. P., Jackson P. D., 1979, A&AS, 38, 197

Morris S. L., 1985, ApJ, 295, 143

Munari U., Tomasella L., 1999, A&A, 343, 806

Muzzio J. C., Orsatti A. M., 1977, AJ, 82, 474

Niemela V. S., Gamen R. C., Barbá R. H., Fernández Lajús E., Benaglia P., Solivella G. R., Reig P., Coe M. J., 2008, MNRAS, 389, 1447

O'Connell D. J. K., 1951, Publications of the Riverview College Observatory, 2, 85

O'Connell D. J. K., 1968, Ricerche Astronomiche, 7, 399

Oswalt T. D., Barstow M. A., 2013, Planets, Stars and Stellar Systems: Volume 4: Stellar Structure and Evolution, doi:10.1007/978-94-007-5615-1.

Otero S. A., Dubovsky P. A., 2004, Information Bulletin on Variable Stars, 5557, 1

Otero S. A., Wils P., 2005, Information Bulletin on Variable Stars, 5630, 1

Otero S. A., Wils P., Hoogeveen G., Dubovsky P. A., 2006, Information Bulletin on Variable Stars, 5681, 1

Pavlovski K., Southworth J., Tkachenko A., Van Reeth T., Tamajo E., 2023, A&A, 671, A139

Pecaut M. J., Mamajek E. E., 2013, ApJS, 208, 9

Perry C. L., Hill G., Christodoulou D. M., 1991, A&AS, 90, 195

Petrova A. V., Orlov V. V., 1999, AJ, 117, 587

Pietrzyński G., et al., 2013, Nature, 495, 76

Plaskett J. S., 1908, ApJ, 28, 266

Pojmanski G., 1998, Acta Astron., 48, 35

Pojmanski G., 2002, Acta Astron., 52, 397

Popper D. M., 1966, AJ, 71, 175

Pourbaix D., et al., 2004, A&A, 424, 727

Pozo Nuñez F., Chini R., Barr Domínguez A., Fein C., Hackstein M., Pietrzyński G., Murphy M., 2019, MNRAS, 490, 5147

Prša A., Zwitter T., 2005, ApJ, 628, 426

Prša A., Guinan E. F., Devinney E. J., DeGeorge M., Bradstreet D. H., Giammarco J. M., Alcock C. R., Engle S. G., 2008, ApJ, 687, 542

Prša A., et al., 2016, ApJS, 227, 29

Prša A., et al., 2022, ApJS, 258, 16

Rauw G., Rosu S., Noels A., Mahy L., Schmitt J. H. M. M., Godart M., Dupret M. A., Gosset E., 2016, A&A, 594, A33

Reed B. C., 1998, ApJS, 115, 271

Reed B. C., 2003, AJ, 125, 2531

Reed B. C., 2005, AJ, 130, 1652

Reed B. C., Beatty A. E., 1995, ApJS, 97, 189

Ren F., et al., 2021, AJ, 161, 176

Ricker G. R., et al., 2015, Journal of Astronomical Telescopes, Instruments, and Systems, 1, 014003

Rios L. Y., DeGioia-Eastwood K., 2004, in American Astronomical Society Meeting Abstracts. p. 09.05

Rosu S., Rauw G., Nazé Y., Gosset E., Sterken C., 2022, A&A, 664, A98

Russell H. N., 1939, ApJ, 90, 641

Salaris M., Cassisi S., 2005, Evolution of Stars and Stellar Populations

Salpeter E. E., 1955, ApJ, 121, 161

Samus' N. N., Kazarovets E. V., Durlevich O. V., Kireeva N. N., Pastukhova E. N., 2017, Astronomy Reports, 61, 80

Sana H., 2017, in Eldridge J. J., Bray J. C., McClelland L. A. S., Xiao L., eds, IAU Symposium Vol. 329, The Lives and Death-Throes of Massive Stars. pp 110–117 (arXiv:1703.01608), doi:10.1017/S1743921317003209

Sana H., Nazé Y., O'Donnell B., Rauw G., Gosset E., 2008, NewA, 13, 202

Sana H., et al., 2012, Science, 337, 444

Savedoff M. P., 1951, AJ, 56, 1

Sawyer E. F., 1887, AJ, 7, 116

Schaerer D., Guibert J., Marques-Chaves R., Martins F., 2025, A&A, 693, A271

Schneider F. R. N., et al., 2018a, Science, 359, 69

Schneider F. R. N., et al., 2018b, Science, 361, aat7032

Shaviv G., 2009, The Life of Stars: The Controversial Inception and Emergence of the Theory of Stellar Structure. Springer, https://link.springer.com/book/10.1007/978-3-642-02088-9

Shi X.-d., Qian S.-b., Li L.-J., 2022, ApJS, 259, 50

Shivvers I., Bloom J. S., Richards J. W., 2014, MNRAS, 441, 343

Simón-Díaz S., Castro N., Garcia M., Herrero A., Markova N., 2011, Bulletin de la Societe Royale des Sciences de Liege, 80, 514

Sota A., Maíz Apellániz J., Walborn N. R., Alfaro E. J., Barbá R. H., Morrell N. I., Gamen R. C., Arias J. I., 2011, ApJS, 193, 24

Sota A., Maíz Apellániz J., Morrell N. I., Barbá R. H., Walborn N. R., Gamen R. C., Arias J. I., Alfaro E. J., 2014, ApJS, 211, 10

Southworth J., 2015, in Rucinski S. M., Torres G., Zejda M., eds, Astronomical Society of the Pacific Conference Series Vol. 496, Living Together: Planets, Host Stars and Binaries. p. 164 (arXiv:1411.1219), doi:10.48550/arXiv.1411.1219

Southworth J., 2020, in Neiner C., Weiss W. W., Baade D., Griffin R. E., Lovekin C. C., Moffat A. F. J., eds, Stars and their Variability Observed from Space. pp 329–334 (arXiv:1912.13400), doi:10.48550/arXiv.1912.13400

Southworth J., Bowman D. M., 2022, MNRAS, 513, 3191

Southworth J., Clausen J. V., 2007, A&A, 461, 1077

Stephenson C. B., Sanduleak N., 1971, Publications of the Warner & Swasey Observatory, 1, 1

Stickland D. J., Lloyd C., Penny L. R., 1997, The Observatory, 117, 213

Struve O., 1944, ApJ, 100, 189

TESS Science Processing Operations Center (SPOC) 2020, TESS Science Data Products Description Document, https://archive.stsci.edu/missions/tess/doc/EXP-TESS-ARC-ICD-TM-0014.pdf

Taormina M., et al., 2025, ApJ, 980, 178

Thackeray A. D., 1966, MNRAS, 131, 435

Thompson S. E., et al., 2012, ApJ, 753, 86

Tkachenko A., et al., 2020, A&A, 637, A60

Tramper F., Sana H., Fitzsimons N. E., de Koter A., Kaper L., Mahy L., Moffat A., 2016, MNRAS, 455, 1275

Trigueros Páez E., Barbá R. H., Negueruela I., Maíz Apellániz J., Simón-Díaz S., Holgado G., 2021, A&A, 655, A4

Trundle C., Dufton P. L., Hunter I., Evans C. J., Lennon D. J., Smartt S. J., Ryans R. S. I., 2007, The VLT-FLAMES survey of massive stars: evolution of surface N abundances and effective temperature scales in the Galaxy and Magellanic Clouds (arXiv:0706.1731), doi:10.1051/0004-6361:20077838

Turner D. G., 1980, ApJ, 235, 146

Vijapurkar J., Drilling J. S., 1993, ApJS, 89, 293

Walborn N. R., Fitzpatrick E. L., 1990, PASP, 102, 379

Walborn N. R., Nichols-Bohlin J., Panek R. J., 1985, NASA Reference Publication, 1155

Weidner C., Vink J. S., 2010, A&A, 524, A98

Welsh W. F., et al., 2011, ApJS, 197, 4

Westerlund B. E., 1963, MNRAS, 127, 71

Wilkinson M. D., et al., 2016, Scientific Data, 3, 160018

Wilson R. E., Devinney E. J., 1971, ApJ, 166, 605

Wu C. C., 1976, in Eggleton P., Mitton S., Whelan J., eds, IAU Symposium Vol. 73, Structure and Evolution of Close Binary Systems. p. 213

Xu Y., Hou L. G., Bian S. B., Hao C. J., Liu D. J., Li J. J., Li Y. J., 2021, A&A, 645, L8

de Mink S. E., Langer N., Izzard R. G., 2011, Bulletin de la Societe Royale des Sciences de Liege, 80, 543

Appendix A

Radial Velocity Analysis

Radial velocity analysis is a fundamental technique in the study of binary stars, allowing for the determination of key orbital parameters such as the semi-major axis, eccentricity, systemic velocity, and mass ratio. These parameters provide essential constraints for modelling stellar systems and deriving absolute properties such as individual masses and radii. The methodology for extracting these parameters from spectroscopic observations has been well established in classical works, such as Batten's comprehensive review on spectroscopic binaries (Batten, 1973), which remains a cornerstone in the field.

In the case of eclipsing binaries, where photometric LCs can provide additional geometric constraints, RV solutions serve as the foundation for obtaining a complete orbital characterization. The combination of spectroscopic and photometric data is crucial, as LCs alone cannot determine absolute masses without external constraints, and RV measurements alone cannot resolve inclination-dependent degeneracies.

This section describes the methodology for obtaining RV curves from spectroscopic data, including spectral data reduction, velocity measurement techniques, and orbital fitting strategies. The procedure was tested and refined using well-characterized systems such as AB Cru, and subsequently applied to WR36 and WR39, where a custom Python-based orbital solution solver was developed.

A.1 Spectral Data Reduction

The extraction of RVs begins with spectral data reduction, which involves processing raw spectroscopic observations into science-ready spectra. This process includes bias subtraction, flat-field correction, wavelength calibration, and optimal extraction of spectral orders in the case of echelle spectra. While standard observatory pipelines provide an initial reduction step, additional refinements are often necessary to achieve high-precision RV measurements.

A crucial aspect of spectral data processing is the normalization of the spectra to the continuum. In this work, a Python-based routine was developed to automate the normalization process. The routine was specifically trained on spectra obtained with FEROS (Fiber-fed Extended Range Optical Spectrograph), a high-resolution echelle spectrograph mounted on the MPG/ESO 2.2m telescope at La Silla Observatory, Chile, and the echelle spectrograph at Las Campanas Observatory (LCO), Chile. Designed with flexibility, the routine can accommodate other spectrographs, ensuring its applicability to a broader range of datasets.

The normalization process follows a multi-step approach:

1. First, a Legendre polynomial of order 9 is fitted to the selected spectral region, providing an initial continuum estimate. The spectrum is then divided by this fit, yielding a preliminary normalized spectrum.

2. The algorithm then identifies key spectral features, classifying different regions as continuum, spectral lines, multiplets, noise, cosmic ray artifacts, and CCD defects (Figure A.1.1). This identification is based on Gaussian fitting in the local environment of spectral features.

3. Once these elements are recognized, a second normalization is performed using only the continuum regions, refining the continuum fit and ensuring a more accurate spectral baseline (Figures A.1.3 and A.1.2).

4. Anomalies, such as cosmic rays and defects, are subsequently removed to prevent contamination in RV measurements.

5. The process can be iterated multiple times; however, in practice, two iterations were found to provide sufficient convergence without the risk of overfitting the automatic method.

This automated normalization method allows for a consistent and efficient approach to preparing spectra for RV analysis, reducing observer-dependent biases. Its adaptability ensures that it can be applied to future datasets beyond the training sample.

A.2 Measuring Radial Velocities

Once the spectra are reduced, RVs are extracted by measuring the Doppler shifts of spectral lines. This is done by fitting Gaussian and Voigt Profiles around the expected centroid of the emission or absorption lines to determine their centroid shifts, providing direct RV measurements. This technique is effective for isolated, well-defined spectral features.

Traditionally, radial velocity measurements are performed using IRAF routines, but a Python-based alternative was developed in this work to provide more automation and flexibility in the process. This tool was validated against IRAF-derived measurements and produced consistent results.

To test the effectiveness of this methodology, RVs were measured for AB Cru (A.2.1, a well-characterized binary system, and the results were compared to previously published values. The same approach was later applied to WR36 and WR39.

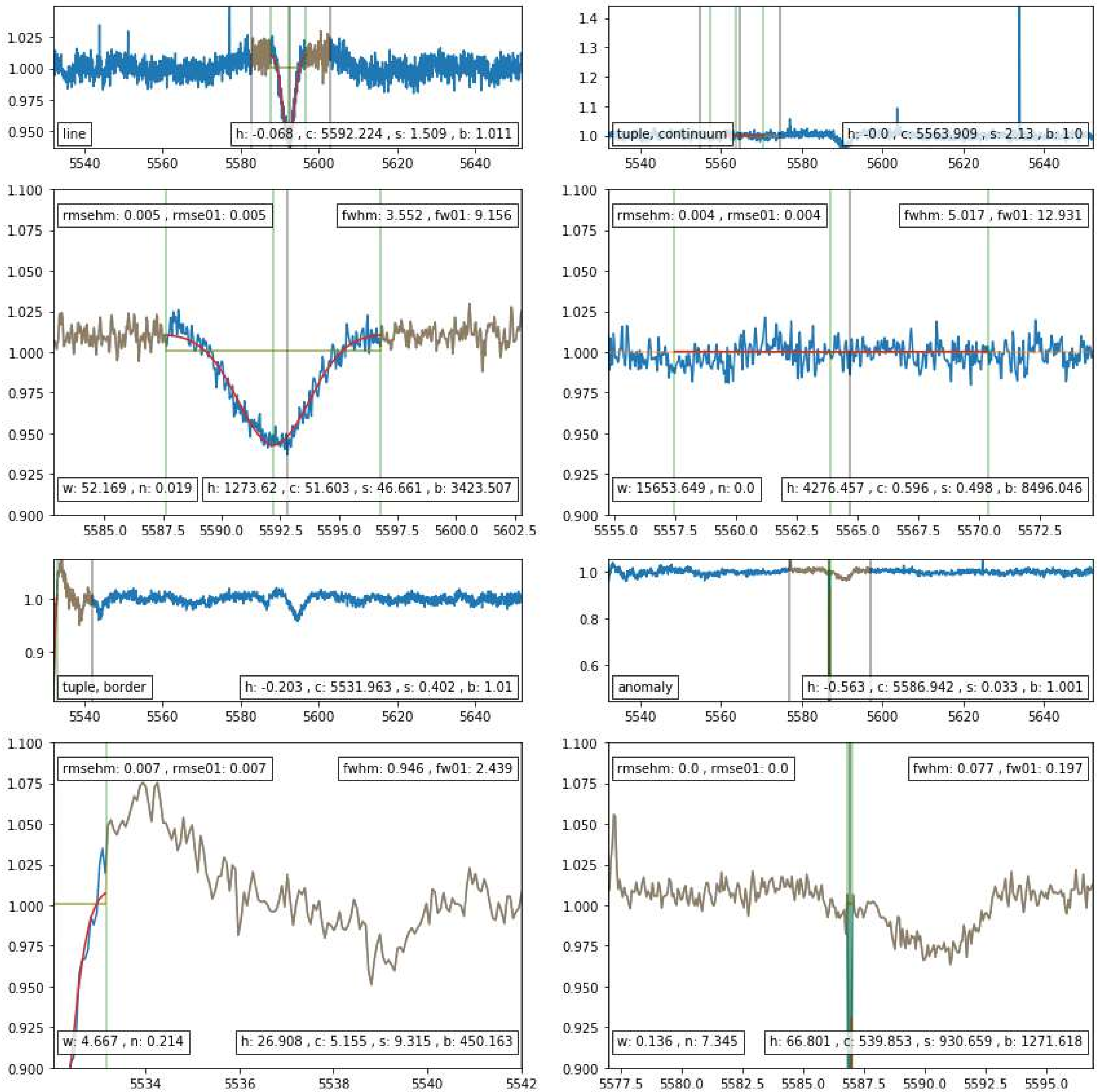

Figure A.1.1: Identification and classification of spectral regions during the automated normalization process. Each subfigure consists of two panels: the upper panel displays the raw spectrum (blue) with the region of interest (RoI) marked in green, along with the fitted profile (red) used for classification; the lower panel presents a zoomed-in view of the identified feature, where the RoI is highlighted in blue, and the remaining spectrum is shown in gray. The method classifies each region based on its shape, width, and fitted parameters, allowing for targeted normalization. The four cases shown are: (top-left) an absorption line, (top-right) continuum region, (bottom-left) spectral border, and (bottom-right) an anomaly (e.g., cosmic rays or CCD defects). These identifications are cases of Figure A.1.2.

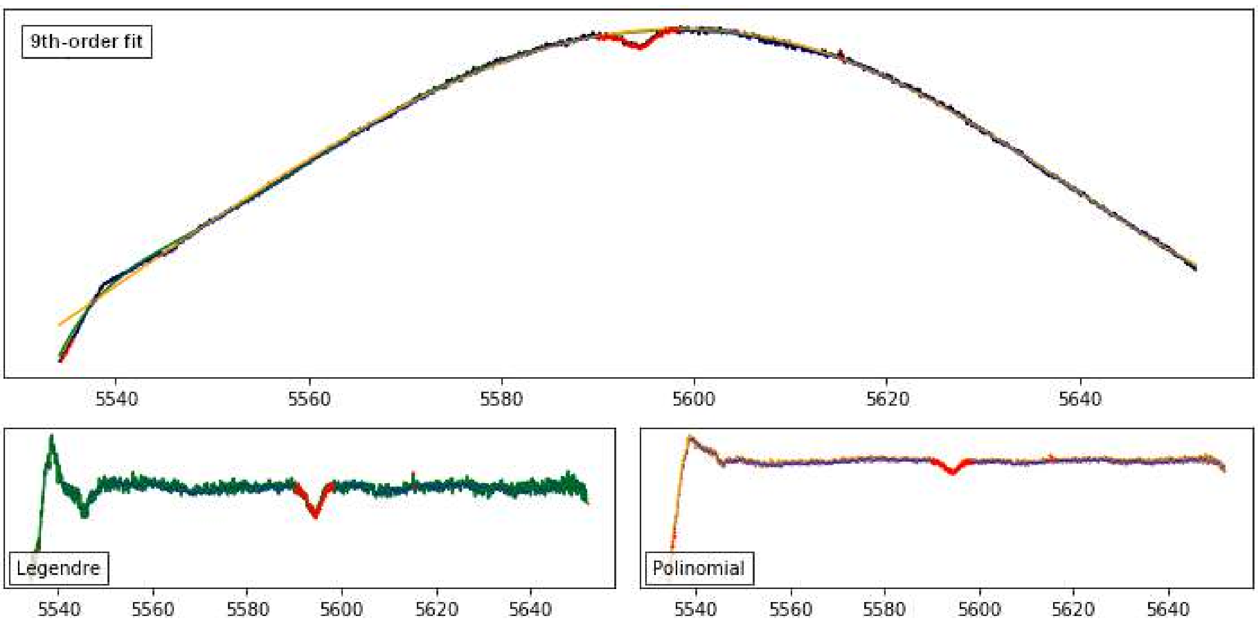

Figure A.1.2: Normalization process for LCO spectra for the O III 5592 Å line used to measure the radial velocities of the primary component. Top panel: The raw spectrum (blue) is fitted with a Legendre polynomial (green) and a 9th-order polynomial (yellow). Regions identified as artifacts (cosmic rays, CCD defects, or spectral features not part of the continuum) are highlighted in red and excluded from the continuum fit. Bottom left panel: Normalization using the Legendre fit. The identified continuum is shown in blue, cosmic rays are marked in green, and artifacts are displayed in red. Bottom right panel: Normalization using the polynomial fit. The continuum is now highlighted in purple, cosmic rays in yellow, and artifacts remain in red.

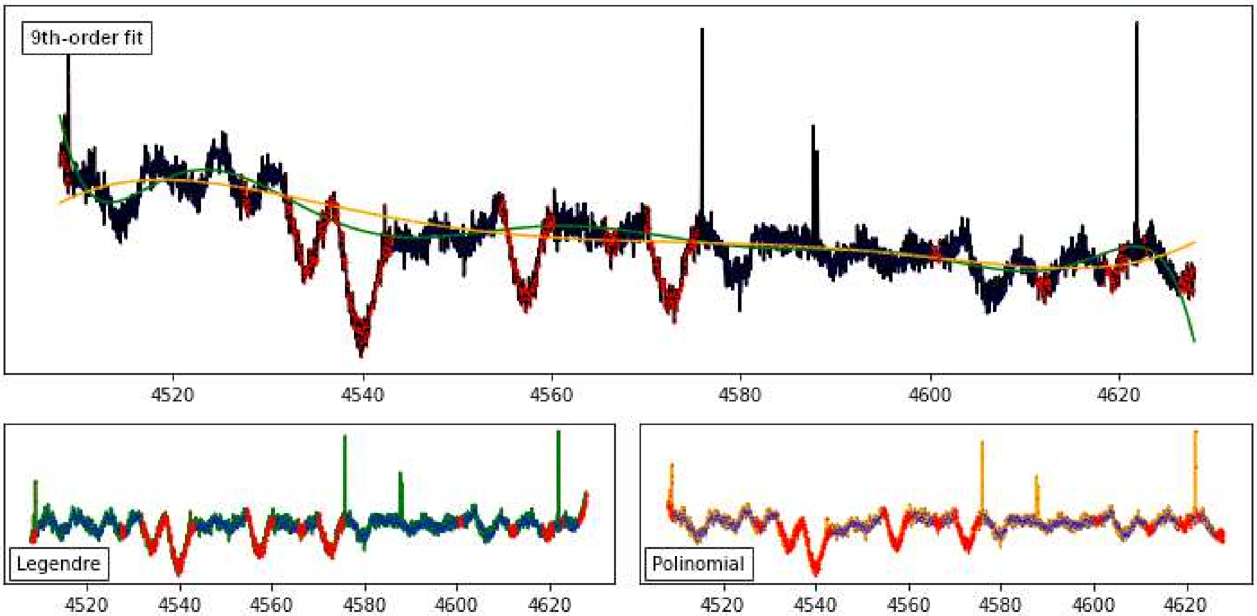

Figure A.1.3: Normalization process for FEROS spectra for the Si III 4552, 4568, and 4575 Å lines used to measure the radial velocities of the secondary component. The normalization method and color scheme are identical to Figure A.1.2

A.3 Orbital Solution Estimation

Once a set of radial velocities is obtained, the next step is to solve for the orbital parameters of the binary system by fitting the observed RV curves with a Keplerian model. This process constrains key parameters, including the orbital period (P), systemic velocity (γ), eccentricity (e), argument of periastron (ω), semi-amplitudes (K_1, K_2), and mass ratio ($q = M_2/M_1$) of the system.

If a light curve is available, the width and depth of eclipses provide indirect information about the system's eccentricity and argument of periastron, which can be used as additional constraints to the RV solution fitting. Figure A.3.1 illustrates this approach.

GBART[1] method can be used as a benchmark for RV fitting (Figure A.3.2). However, as an older program, GBART presents compatibility challenges, even with a portable version. While it remains functional, Python offers a more flexible and adaptable environment for handling large datasets and complex orbital configurations. Python-based implementations allow for direct modifications and enhancements to the code, enabling greater customization when dealing with intricate spectroscopic data. Additionally, Python's extensive ecosystem, including modules such as ASTROPY, facilitates seamless integration of plotting, data handling, and cross-compatibility with other astronomy-focused tools.

Given the above mentioned constraints of GBART, and that key astrophysical software like PHOEBE

[1] GBART is an improved version of the program for the determination of the orbital elements for spectroscopic binaries originally written by Bertiau & Grobben (1969), and updated in Bareilles (2017).

Figure A.2.1: Measurement of radial velocities from the O III 5592 Å line for the primary component (left column), followed by the Si III 4552, 4568, and 4575 Å for the secondary component. The top row displays all 16 spectra overlaid, with the red vertical line indicating the expected centroid position. The lower 16 rows correspond to individual spectra, arranged by orbital phase to illustrate the progressive shift of the spectral line. Each panel includes the measured centroid shift in the top left corner and the orbital phase in the top right corner.

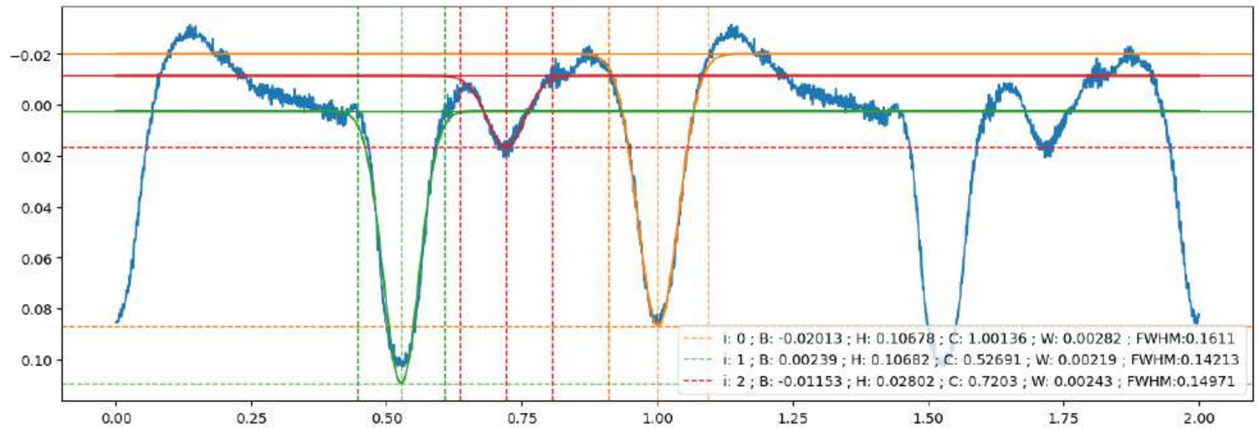

Figure A.3.1: Measurement of eclipse width and depth in a detached binary system. The relative width and depth of the eclipses provide indirect constraints on the system's eccentricity and argument of periastron. These measurements help refine the range of values considered in the radial velocity solution.

ELEMENTOS DE LA PRIMERA COMPONENTE				
A sin i	-.509411E+07	+-	0.176E+06	km
K	-108.539	+-	3.767	km/s
Exc	.0105	+-	.0189	
Omega	283.549	+-	62.514	grad
T. Periast	57114.6081	+-	0.5915	DJ
T. V.Max	57115.3218	+-	0.5915	DJ
Periodo	3.41329905	+-	0.00000000	Dias
V(1)	-6.972	+-	2.260	km/s
ELEMENTOS DE LA SEGUNDA COMPONENTE				
A sin i	-.146867E+08	+-	0.174E+06	km
K	-312.924	+-	3.713	km/s
M1 sin3 i	-19.6261	+-	1.1577	M. Sol
M2 sin3 i	-6.8073	+-	1.1756	M. Sol
Q(M1/M2)	0.3469	+-	-0.0162	

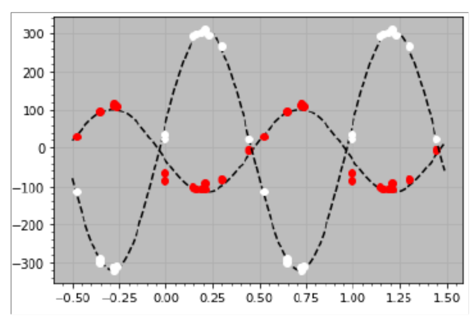

Figure A.3.2: Orbital Solution for AB Cru as Determined by GBART Analysis. The left panel details the orbital elements for the primary and secondary components of the system, including the semi-major axis, eccentricity, inclination, and masses. The right panel displays the radial velocity curve, with observed data points marked in red and the model fit shown in grey dashed lines, illustrating the periodicity and amplitude variations due to orbital motion.

and LIGHTKURVE are now exclusively Python-based, transitioning to a Python implementation ensures alignment with modern research workflows and long-term software sustainability. A dedicated Python implementation of RV curve fitting was developed.

A.3.1 Python-Based Orbital Solution Solver

In order to determine the orbital parameters, we implemented a Python-based radial velocity solver. This method follows the classical methodology described in Bertiau & Grobben (1969) and Hilditch (2001), implementing numerical methods for solving Kepler's equation and computing RV curves. The Python implementation ensures flexibility, cross-compatibility with modern tools, and allows direct integration with light curve modelling.

The foundation of the orbital solution relies on Kepler's equation:

$$M = E - e\sin E, \tag{A.3.1}$$

where M is the mean anomaly, E is the eccentric anomaly, and e is the orbital eccentricity. Solving for E requires an iterative numerical method, for which we employ Newton-Raphson iteration:

$$E_{n+1} = E_n - \frac{E_n - e\sin E_n - M}{1 - e\cos E_n}. \tag{A.3.2}$$

This iterative approach is used in both scalar and array-based computations to efficiently determine E values for a dataset of RV observations.

Once the eccentric anomaly is known, the true anomaly ν can be computed using:

$$\tan\frac{\nu}{2} = \sqrt{\frac{1+e}{1-e}}\tan\frac{E}{2}. \tag{A.3.3}$$

With this, the radial velocity of each component is determined via:

$$V = \gamma + cK(\cos(\omega+\nu) + e\cos\omega), \tag{A.3.4}$$

where K is the semi-amplitude of the velocity curve, γ is the systemic velocity, ω is the argument of periastron, and c is a scaling factor that accounts for the primary and secondary components.

To obtain the best-fitting parameters, a nonlinear least-squares fitting approach is used. The Python solver employs SCIPY's *curve_fit* function to minimize residuals between observed and modeled RVs. A two-step fitting procedure is used:

1. Primary star's velocity curve is fitted to estimate initial parameters (K_1, e, ω, γ).
2. Secondary star's velocity curve is fitted using the primary solution as a prior, constraining K_2 and refining q.

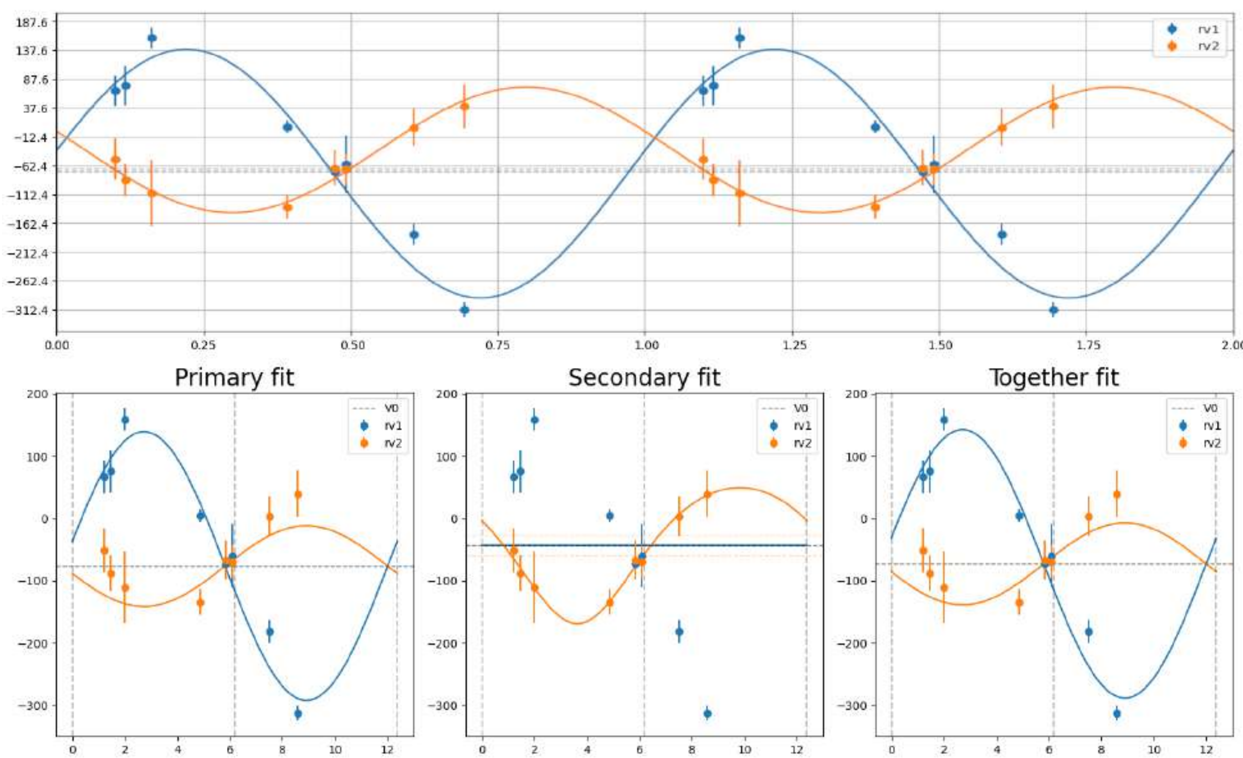

Figure A.3.3: Orbital Fitting of LS_VI_+00_25 using a Custom Python Implementation. The top panels show sinusoidal fits used to derive initial parameter estimates, serving as starting guesses for the radial velocity (RV) curve fitting depicted in the bottom panels. From left to right, the bottom panels illustrate fits for the primary component, the secondary component, and both components simultaneously. Data points for the primary and secondary components are represented by blue and orange markers, respectively, with the fitted curves shown in corresponding colors. Due to the limited data available in the quadratures and the considerable error margins of available data, these results are preliminary. Further analysis will be pursued with additional spectral data.

Once individual fits are obtained, a simultaneous fitting of both components is performed using a combined likelihood approach, minimizing residuals for both curves while enforcing constraints from photometric measurements.

From the fitted parameters, we can derive the mass function:

$$f(M) = \frac{(K_1 + K_2)^3 P}{2\pi G(1-e^2)^{3/2}}, \tag{A.3.5}$$

which provides constraints on the absolute masses when combined with inclination constraints from photometric modelling.

The methodology developed here is designed to be applicable to a broader sample of massive binary systems. As additional spectroscopic data becomes available, the same techniques will be employed to derive RV solutions for more systems in the YMDB catalog. The final radial velocity solutions derived from this methodology will then be used as input for light curve modelling with PHOEBE (see Section 3.4) to obtain absolute parameters for the desired systems.

Appendix B

Applications Beyond the YMDB Catalog

The methodologies developed for the YMDB catalog were also applied to additional massive binary systems, providing opportunities to refine and validate the techniques in different observational contexts. This section explores these applications, focusing on WR21a, WR36, and WR39—systems that posed unique modeling challenges and helped further improve the data analysis pipeline.

In controlled conditions, such as synthetic models, PHOEBE's solvers can reliably recover input parameters, demonstrating their robustness for binary system characterization. However, real observational data—such as those from TESS—introduce additional complexities, including systematics, third-light contamination, and sparse phase coverage, which can impact the accuracy of derived stellar parameters.

Addressing these challenges requires a systematic approach, beginning with RV analysis to constrain the orbital parameters, followed by LC modelling to refine the stellar properties. While PHOEBE provides solvers for these tasks, certain limitations—such as convergence issues and parameter degeneracies—persist in complex systems. To mitigate these challenges, an alternative methodology was developed, incorporating external estimators to derive initial orbital parameters before integrating them into PHOEBE.

For RV modelling, the GBART method (Bareilles, 2017) is a well-established tool for resolving spectroscopic binary orbits. To enhance flexibility and mitigate compatibility issues found in legacy software, a modern Python-based solver was developed following the methodologies outlined in Bertiau & Grobben (1969) and Hilditch (2001). This solver was validated against well-characterized systems such as AB Cru (Figure A.3.2) before being applied to WR36 and WR39 (B.2). Additionally, constraints on eccentricity (e) and argument of periastron (ω) were inferred from eclipse width and depth in the LCs (Figure A.3.1).

Once orbital parameters were determined, light curve modeling proceeded step by step. Key properties such as stellar temperatures, masses, and radii were inferred from spectral classification and evolutionary models rather than being directly solved by PHOEBE (see A.2). The LC geometry estimator and Nelder-Mead optimizer in PHOEBE were then employed to refine system parameters.

While PHOEBE's optimizers are powerful, they can struggle with convergence in systems with strong systematics or complex variability. To mitigate this, an alternative approach was implemented to efficiently explore parameter space. A computationally expensive "Cannon" method was deployed across 60 parallel computing clusters, generating a broad parameter space grid where key parameters such as stellar masses and radii were varied in coarse steps. A RMSE metric was then used to compare each model to the observed LC, allowing identification of parameter regions best matching the observations (Figure B.0.1). This technique helped circumvent optimizer convergence failures and local minima, particularly in cases with observational uncertainties. Once a promising region of parameter space was identified, a refined grid with higher accuracy was used before applying traditional optimizers.

Once an optimized solution was established, PHOEBE2's Monte Carlo Markov Chain (MCMC) simulations provided a statistically robust framework for estimating parameter uncertainties. The MCMC analysis explored the region of interest in parameter space for WR21a, focusing on the primary and secondary radii (R_1, R_2) and orbital inclination (i). The resulting posterior distributions (Figure B.0.2) illustrate parameter correlations and the confidence intervals derived from the sampled solutions.

A similar approach was applied to KU Car (Martín-Ravelo et al., 2021), where multi-filter photometric modelling provided additional constraints despite the absence of an RV analysis. Unlike WR21a, where the missing secondary eclipse limited precise radius determinations, the multi-filter fitting in KU Car allowed for a color-dependent analysis of the system. However, since robust determinations of absolute stellar parameters require simultaneous modelling of both RV and LC data, the lack of spectroscopic constraints limited the precision of the derived stellar masses. Despite this, the extracted light curves provided critical insights into the system's nature.

Beyond WR21a and KU Car, this methodology has been successfully applied to WR36 and WR39, where the refinement of the pipeline for third-light corrections and spectral normalization significantly improved RV precision (see Appendix B.2). These improvements are essential for the broader application of these methods to the YMDB catalog.

B.1 WR21a: A Massive Eclipsing Wolf-Rayet Binary

WR21a is a high-mass eclipsing binary consisting of a Wolf-Rayet primary (WN6ha) and an O3V((f*))z secondary.WR stars represent a crucial phase in the evolution of the most massive stars, characterized by strong stellar winds and significant mass loss. The evolutionary status of WR21a suggests that its primary component is still in a hydrogen-burning phase, making it an Of/WN transition object rather than a classical helium-burning WR star.

The system was first identified as a spectroscopic binary by Niemela et al. (2008), with subsequent refinements by Tramper et al. (2016). The discovery of eclipses in TESS photometry confirmed WR21a as a detached eclipsing binary, enabling a detailed analysis of its absolute parameters. This makes WR21a one of the rare WR binaries where direct dynamical mass measurements are possible, providing critical constraints for evolutionary models of massive stars.

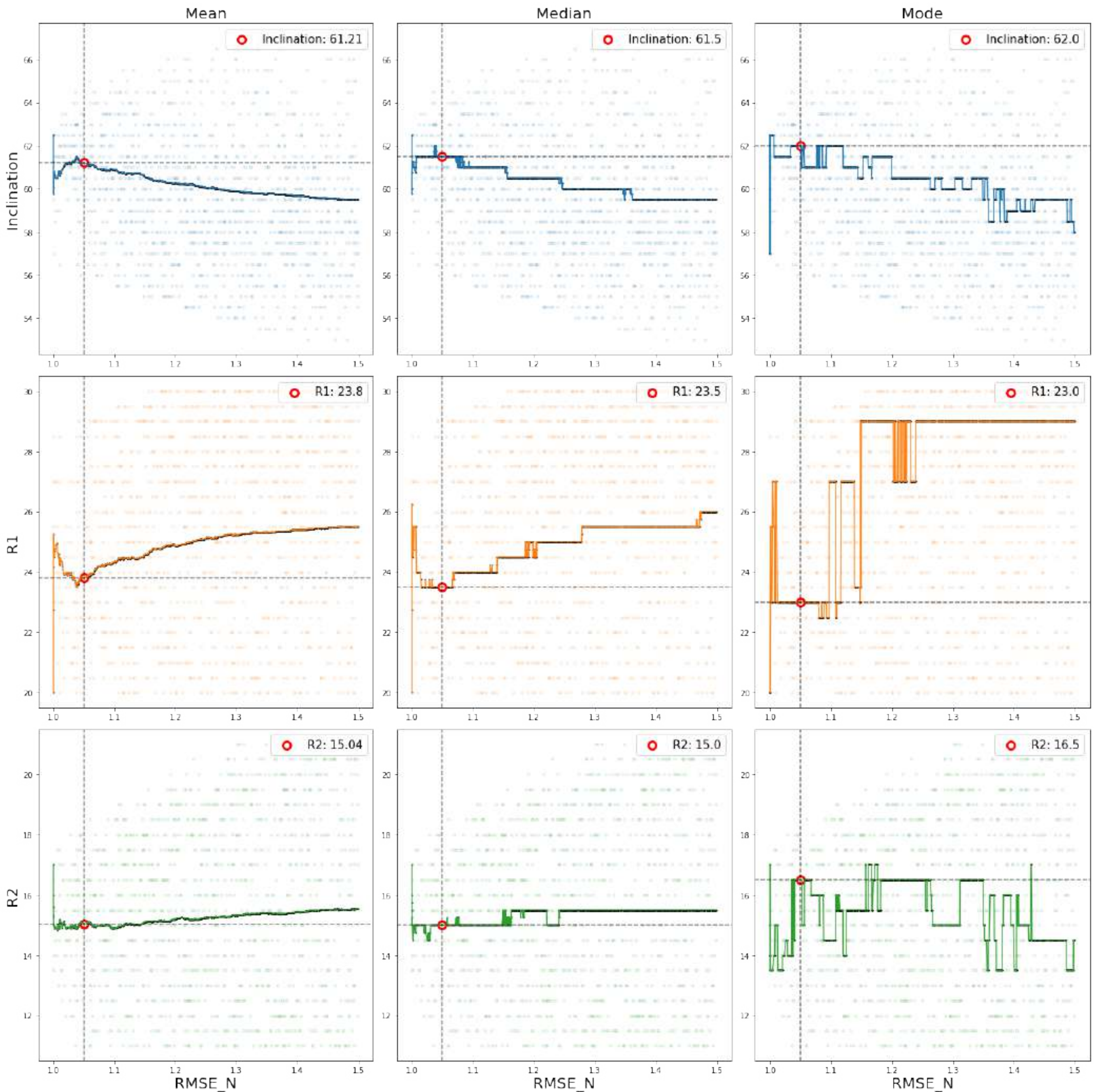

Figure B.0.1: RMSE analysis for the inclination (*top row*), primary radius R_1 (*middle row*), and secondary radius R_2 (*bottom row*) in the PHOEBE model grid for WR21a. Each column represents a different statistical approach: mean (*left*), median (*center*), and mode (*right*). For each RMSE threshold, we compute the mean, median, and mode of the parameter values for all models with RMSE $\leq$ threshold. A characteristic trend emerges where the parameter values initially shift in one direction before reversing, with the first turning point providing a robust first-order approximation of the best-fit value. The red circles indicate the selected first-order estimates used as priors in the MCMC refinement.

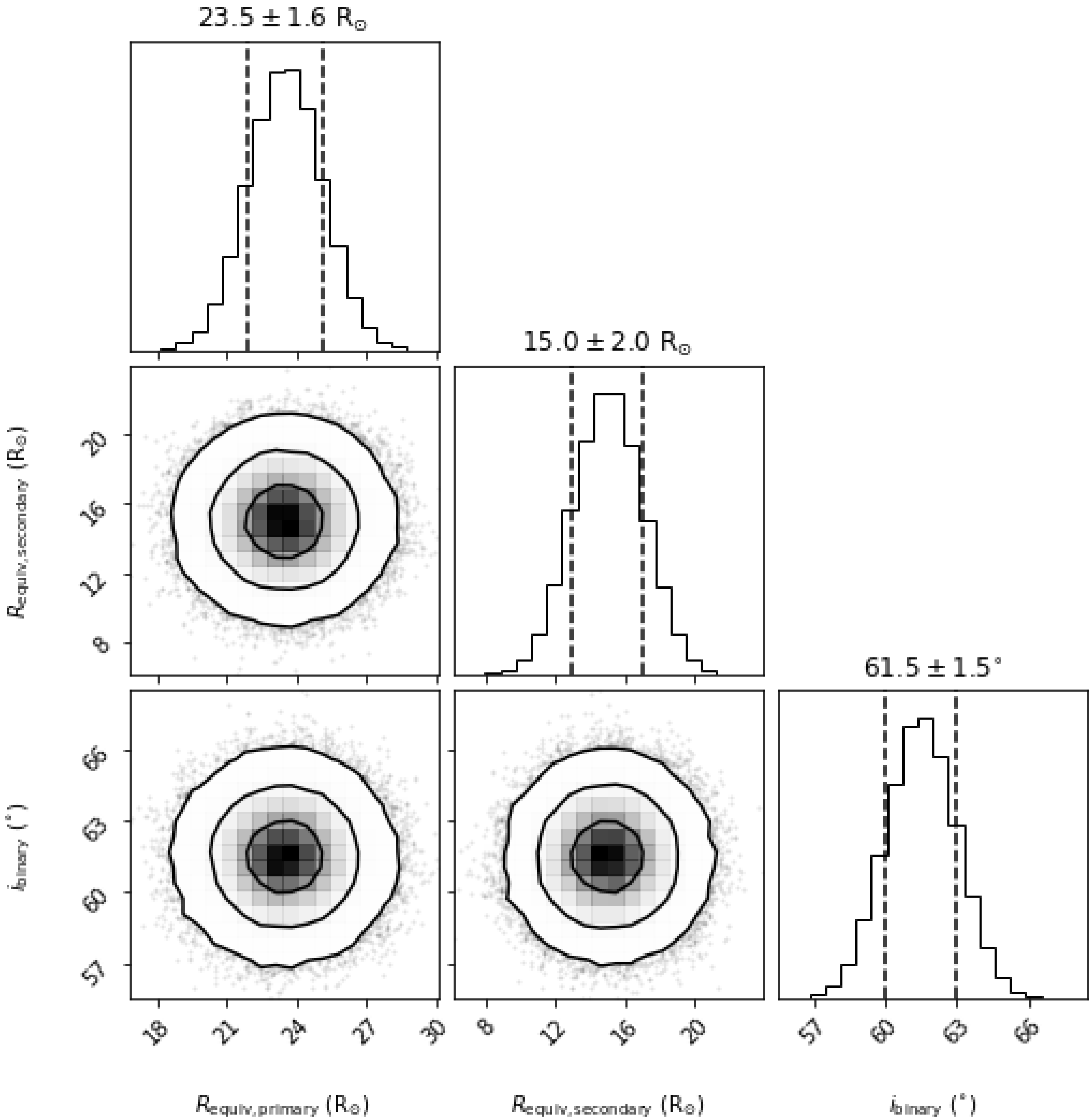

Figure B.0.2: Corner plot displaying the posterior distributions of the primary radius (R_1), secondary radius (R_2), and orbital inclination (i) for WR21a, as obtained from MCMC sampling. The histograms represent the marginalized distributions for each parameter, with dashed lines indicating the median and 1σ confidence intervals. Contour levels in the 2D density plots mark regions containing 68%, 95%, and 99.7% of the samples, highlighting the correlation structure between parameters.

B.1.1 Photometric Analysis

The TESS light curve for WR21a was extracted from FFIs across four observation sectors (9, 10, 36, and 37). Using the methodology described in Section 3.2.1, photometry was performed with `lightkurve`, applying customized masks to minimize contamination. The resulting light curve revealed a pronounced dimming event lasting approximately 20.5 hours, consistent with a partial eclipse of the O3V companion by the WN6ha primary. The detected minima allowed the derivation of a new photometric ephemeris, confirming an orbital period of 31.7 days.

To model the photometric data, we employed PHOEBE2, incorporating orbital parameters derived from RV solutions (see Section A). The effective temperatures for both components were constrained using spectral classification. Due to the absence of a secondary eclipse, direct radius determinations were not possible; instead, a grid-based approach was used to identify the best-fitting model parameters. The resulting orbital inclination of $i = 62.2^{\circ} \pm 0.9^{\circ}$ enabled the calculation of absolute masses, placing WR21a firmly in the very massive star (VMS) regime. The full comparison between the observed TESS light curve and the PHOEBE model, including residuals and best-fitting solutions, is presented in Figure B.1.1.

B.1.2 Light Curve modelling with PHOEBE

The PHOEBE modelling process followed an iterative approach. Initial parameter constraints were obtained from spectroscopic data, with refinements applied based on light curve morphology. The best-fit model was determined by exploring a broad parameter space, minimizing residuals between observed and synthetic light curves.

A significant challenge in modelling WR21a's light curve was the presence of TEOs, which introduced short-term variability. To mitigate their impact, we focused on fitting the eclipse region separately to prevent bias in the parameter estimation. The final PHOEBE solution provided radii of $R_1 = 23.4R_{\odot}$ and $R_2 = 14.3R_{\odot}$, with absolute masses of $M_1 = 93.2M_{\odot}$ and $M_2 = 52.9M_{\odot}$. Full orbital Solutions and stellar parameters are shown on Table B.1.1.

The robustness of the parameter determination was further evaluated through extensive modelling, including a grid search of the parameter space before employing the `emcee` sampler to refine uncertainties. The distribution of normalized residuals across a large number of PHOEBE models is shown in Figure B.1.2, highlighting the sensitivity of the best-fit solution to key parameters such as the inclination and radii.

Beyond the eclipses, WR21a's light curve exhibited quasi-periodic variability, indicative of TEOs. Frequency analysis revealed multiple harmonics of the orbital period, suggesting a strong tidal interaction. These oscillations provide valuable insights into the internal structure of massive stars, offering an indirect probe of their response to gravitational forces.

While WR21a is currently detached, the presence of a WR component suggests significant past or ongoing mass loss. The system is an important test case for binary evolution models, particularly regarding WR formation channels and the role of mass transfer in shaping the final evolutionary fate of very massive

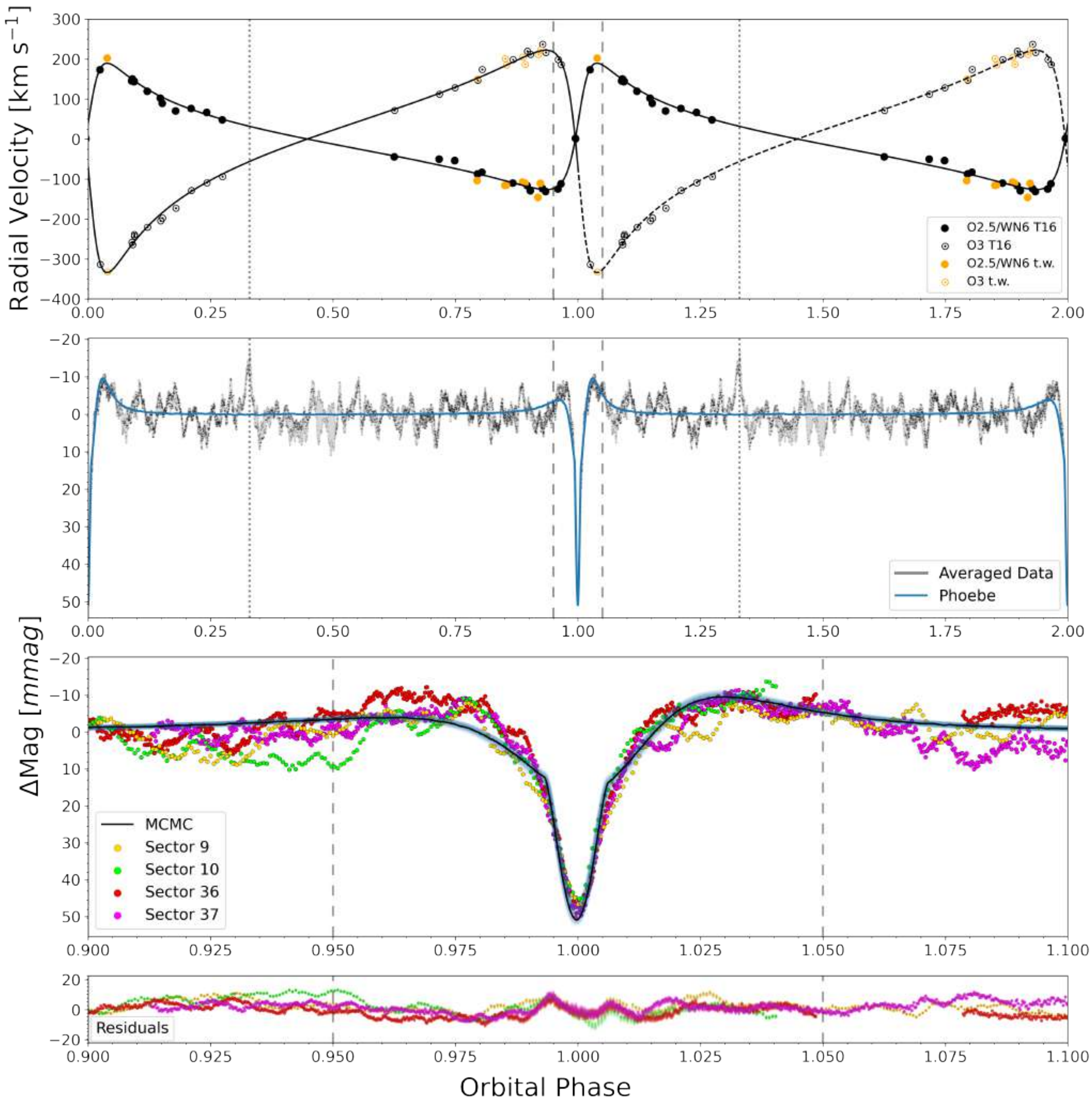

Figure B.1.1: Figure 2 from Barbá et al. (2022). Top: RV curves of the WN and O components using values from Tramper et al. (2016) and Table 2, corrected for their respective systemic velocities. Middle-top: Averaged TESS light curve and the adopted PHOEBE model. Middle-bottom: Comparison between the best 50 PHOEBE models (in light blue) with the photometric time series observed in the four TESS sectors. Black line represents the model for the `emcee` solution (Table 3). Bottom: Residuals derived from TESS photometric observations and PHOEBE models.

Table B.1.1: Orbital solution and stellar parameters.

Parameters obtained from the *TESS* light curve		
P [d]	31.67855 ± 0.00002	
T_{ecl} [HJD]	$2\,459\,322.989 \pm 0.001$	
Orbital parameters obtained through the FOTEL code		
Parameter	Primary	Secondary
$T_{\mathrm{periastron}}$ [HJD]	$2\,459\,323.144 \pm 0.001$	
e	0.695 ± 0.007	
ω [°]	286.8 ± 1.0	
K_i [km s^{-1}]	158.0 ± 2.7	278.1 ± 2.8
$a_i \sin i$ [$R_\odot$]	71.1	125.2
$M_i \sin^3 i$ [$M_\odot$]	64.6	36.7
q [M_2/M_1]	0.568 ± 0.011	
r.m.s$_{(O-C)}$ [km s^{-1}]	9.7	10.8
Stellar parameters obtained with the PHOEBE code		
i [°]	$62.19^{+0.77}_{-0.84}$	
T_{eff} [K]	42 000 (fixed)	48 000 (fixed)
M_i [$M_\odot$]	$93.2^{+2.2}_{-1.9}$	$52.9^{+1.2}_{-1.1}$
R_i [$R_\odot$]	$23.37^{+0.52}_{-0.64}$	$14.28^{+0.82}_{-0.81}$
$\log g_i$	$3.669^{+0.023}_{-0.017}$	$3.851^{+0.048}_{-0.037}$
$\log L$ [$L_\odot$]	6.18 ± 0.06	6.02 ± 0.09
M_{bol} [mag]	-10.71 ± 0.15	-10.30 ± 0.22

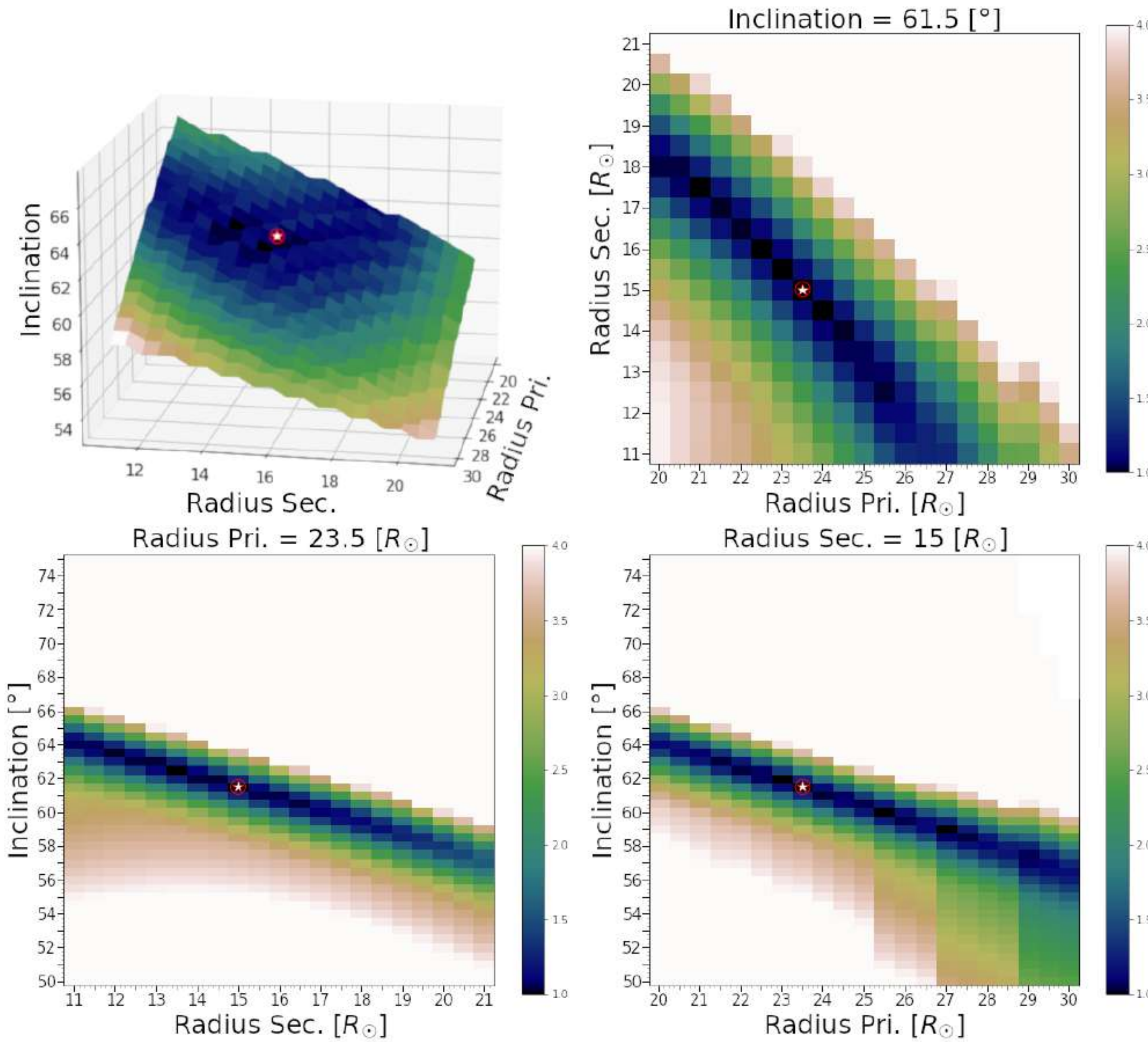

Figure B.1.2: Figure 5 from Barbá et al. (2022). 3-D map distribution of normalised RMS values for the set of parameters (i, R_1, R_2) used to calculate the PHOEBE models (upper -left). The other three panels show orthogonal cuts at the position of the adopted averaged values for R_1, R_2 and i: (R_1, R_2) at fixed i (upper -right), (R_2, i) at fixed R_1 (lower-left), and (R_1, i) at fixed R_2 (lower right). The colour bar represents normalised RMS values. A total of 22491 models were run for the estimation of these values, which then served as priors for the *emcee* PHOEBE solver, which provides a more precise value (Table B.1.1), and also estimates the errors on the desired local region.

binaries.

WR21a is one of the very few eclipsing WR+O binaries where direct dynamical masses can be determined. Compared to systems like WR20a and NGC 3603-A1, which are near-contact binaries undergoing active mass transfer, WR21a remains detached. This unique configuration allows for studying massive stars before Roche lobe overflow, placing WR21a in a crucial evolutionary stage that precedes the onset of strong binary interaction.

B.2 Application to WR36 and WR39

As part of the research led by Dr. André-Nicolas Chené, TESS light curves of two Wolf-Rayet stars, WR36 and WR39, were analyzed using a refined version of our TESS light curve extraction pipeline. Both systems are located in highly contaminated fields, requiring advanced data processing techniques to mitigate the effects of crowding and background flux. These challenges provided an opportunity to optimize the pipeline, improving its ability to extract precise light curves in complex environments. Additionally, WR36 and WR39 served as test cases for a Python-based radial velocity solver, originally developed and calibrated on these systems. This solver is now being adapted for broader application within the YMDB catalog project, while improvements made to the TESS extraction pipeline have enhanced light curve quality for similarly complex binary systems.

The extraction of TESS light curves for these systems presented unique challenges due to severe field contamination and sector-dependent systematics (Figure B.2.1). Despite these obstacles, the methodology successfully retrieved clean photometry, demonstrating its robustness for use in crowded fields. WR36 displayed a light curve typical of a close binary (EW-type) with additional oscillations (Figure B.2.2), which may indicate intrinsic variability beyond binarity. Meanwhile, WR39 exhibited a well-defined eclipsing binary (EA-type) light curve, making it an excellent candidate for absolute parameter determination.

In the case of WR39, the extraction process required fine-tuning to properly account for third-light contamination. Due to the star's varying pixel position across TESS observations, the third-light contribution differed between sectors. A correction procedure was implemented to ensure consistency in the final combined light curve (Figure B.2.3). This step is crucial when modelling the system with PHOEBE, as third-light contamination can significantly impact the derived stellar parameters.

WR39 also presents a particularly interesting case due to the presence of three distinct eclipses in the light curve, suggesting a non-trivial orbital configuration. Initial RV modelling, using a preliminary dataset, yielded an orbital solution with an eccentricity and argument of periastron that predicted a secondary eclipse coinciding with what was initially interpreted as a third eclipse (Figure B.2.4, left panel). This unexpected result was proof that additional spectra was required for a precise RV solution. Additional spectra were obtained through a Director's Discretionary (DD) program at Gemini South (GS-2024A-DD-105). The new RV dataset, particularly filling gaps around phase 0.75, immediately ruled out the initial orbital solution, demonstrating the importance of complete phase coverage in RV studies (Figure B.2.4).

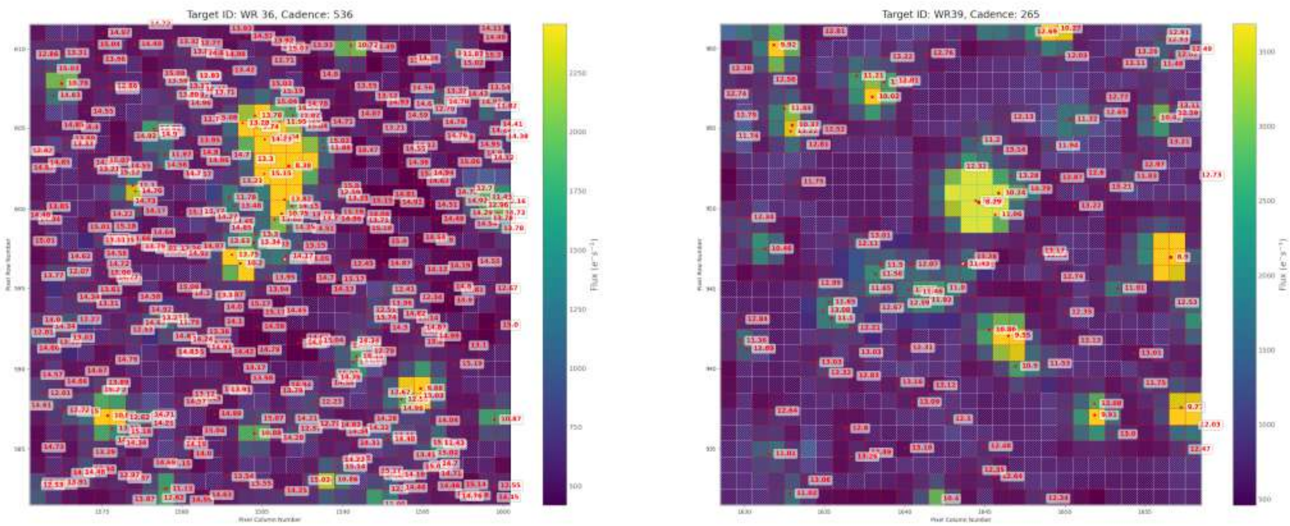

Figure B.2.1: Comparison of field contamination for WR36 (left) and WR39 (right) based on TESS full-frame images. Overlaid labels indicate nearby stars with their respective magnitudes from the Gaia catalog. The WR39 field required a recalculated third-light contribution due to the variability of background contamination across TESS sectors.

The Python-based RV solver developed for this work provided an opportunity to fine-tune the algorithm before its full implementation in the YMDB catalog analysis. The experience gained in handling complex systems will be directly applied to refining the methodology for detached massive binaries in crowded fields, where precise orbital parameters are crucial for understanding their evolutionary state.

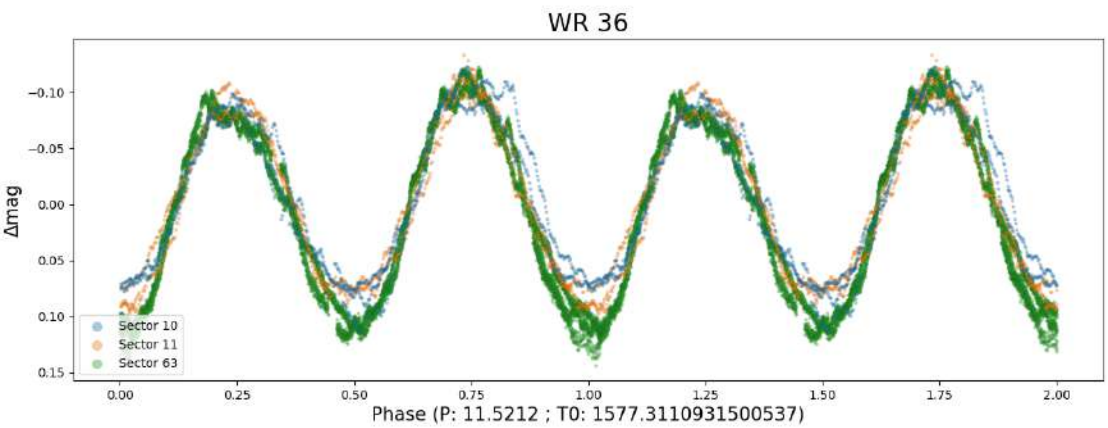

Figure B.2.2: Phase-folded TESS light curve of WR36. The system exhibits ellipsoidal variability with additional oscillations that may be related to pulsations or other mechanisms. The light curve was extracted using the pipeline developed for this work, demonstrating its adaptability to complex systems.

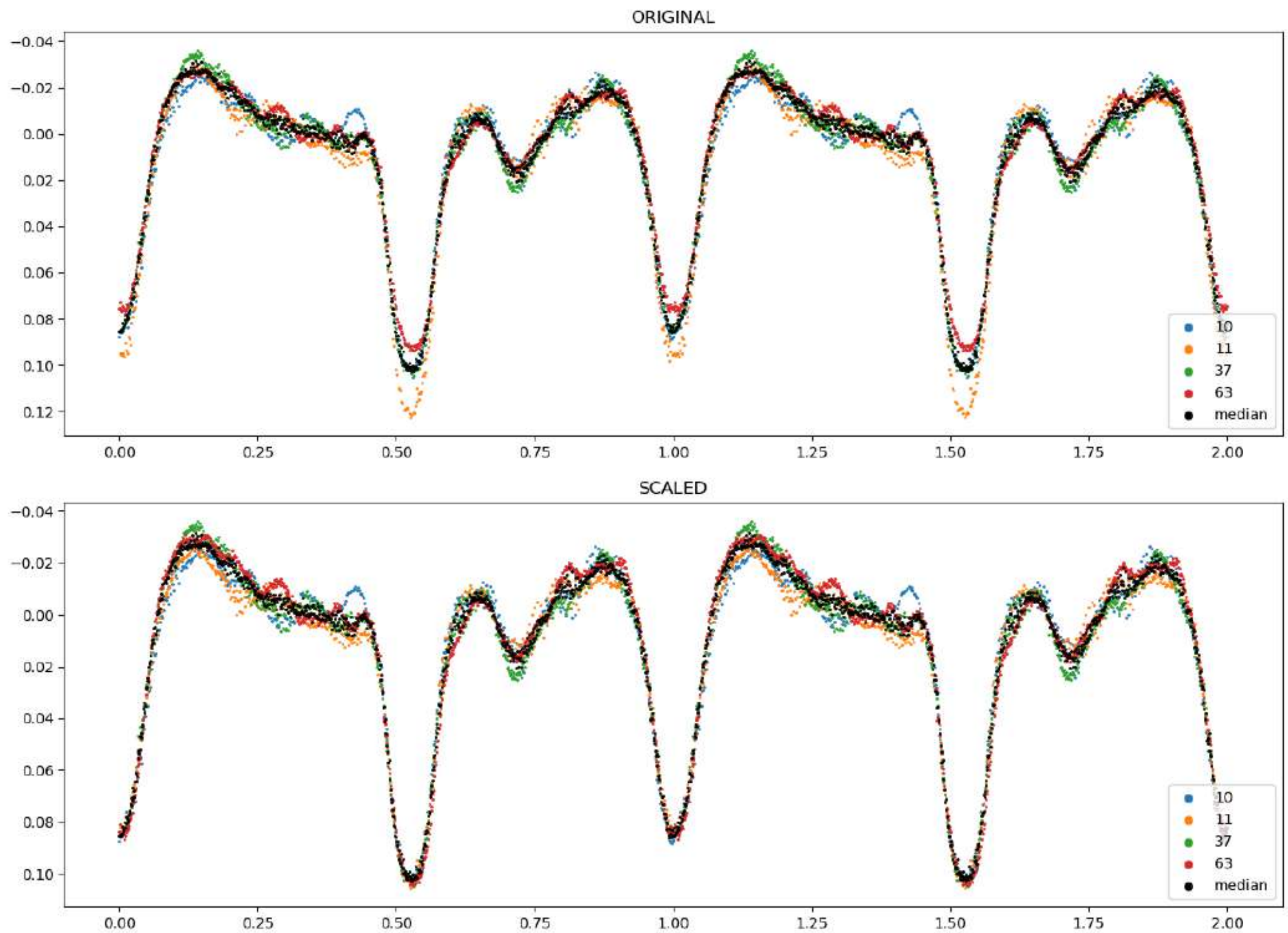

Figure B.2.3: Third-light correction for WR39. Due to significant variability in third-light contamination across different TESS sectors, corrections were applied to ensure consistency in the extracted light curve. The methodology used here informs similar corrections for YMDB objects observed in crowded fields.

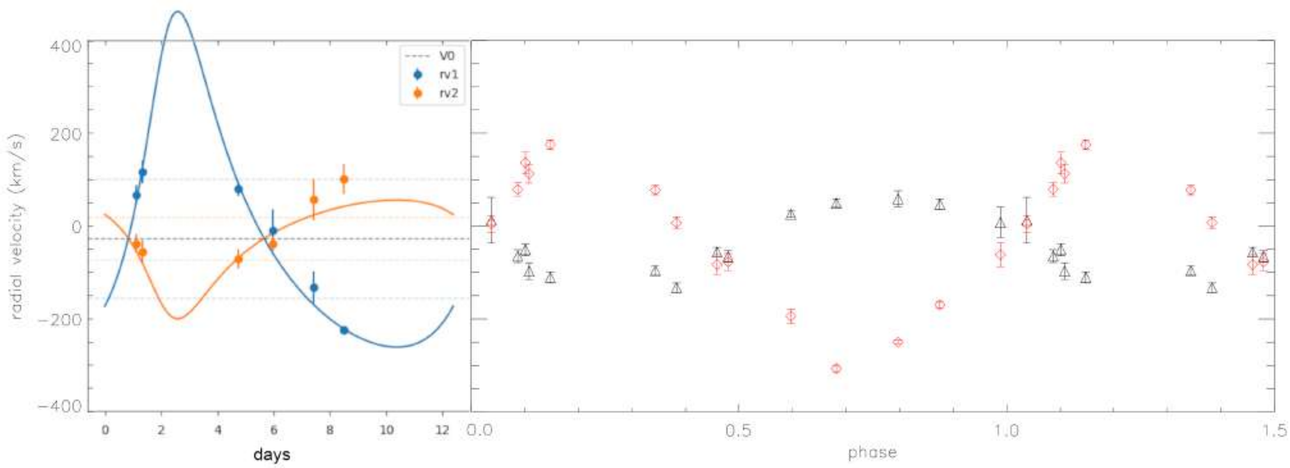

Figure B.2.4: Radial velocity solutions for WR39 before and after additional spectroscopic observations. Left: Initial orbital solution, which predicted a secondary eclipse coinciding with the suspected third eclipse in the light curve. Right: Updated RV solution incorporating new Gemini South spectra, ruling out the previous model and requiring a revised orbital configuration. This refinement process parallels the methodology being implemented for YMDB binaries.

Appendix C

Additional figures

C.1 YMDB systems showing heartbeat phenomena

Heartbeat variations are a distinctive feature of eccentric binary systems, caused by tidal interactions as the stars approach periastron. These variations appear as characteristic flux changes in the light curve, typically occurring just before or after the primary eclipse. While eccentricity is often identified when the secondary eclipse deviates from phase 0.5, some systems only exhibit a primary eclipse, making it difficult to determine their orbital shape. In such cases, the presence of a heartbeat signal serves as a clear indicator of orbital eccentricity. The following figure presents the light curves of all systems in the YMDB catalog where heartbeat features have been identified.

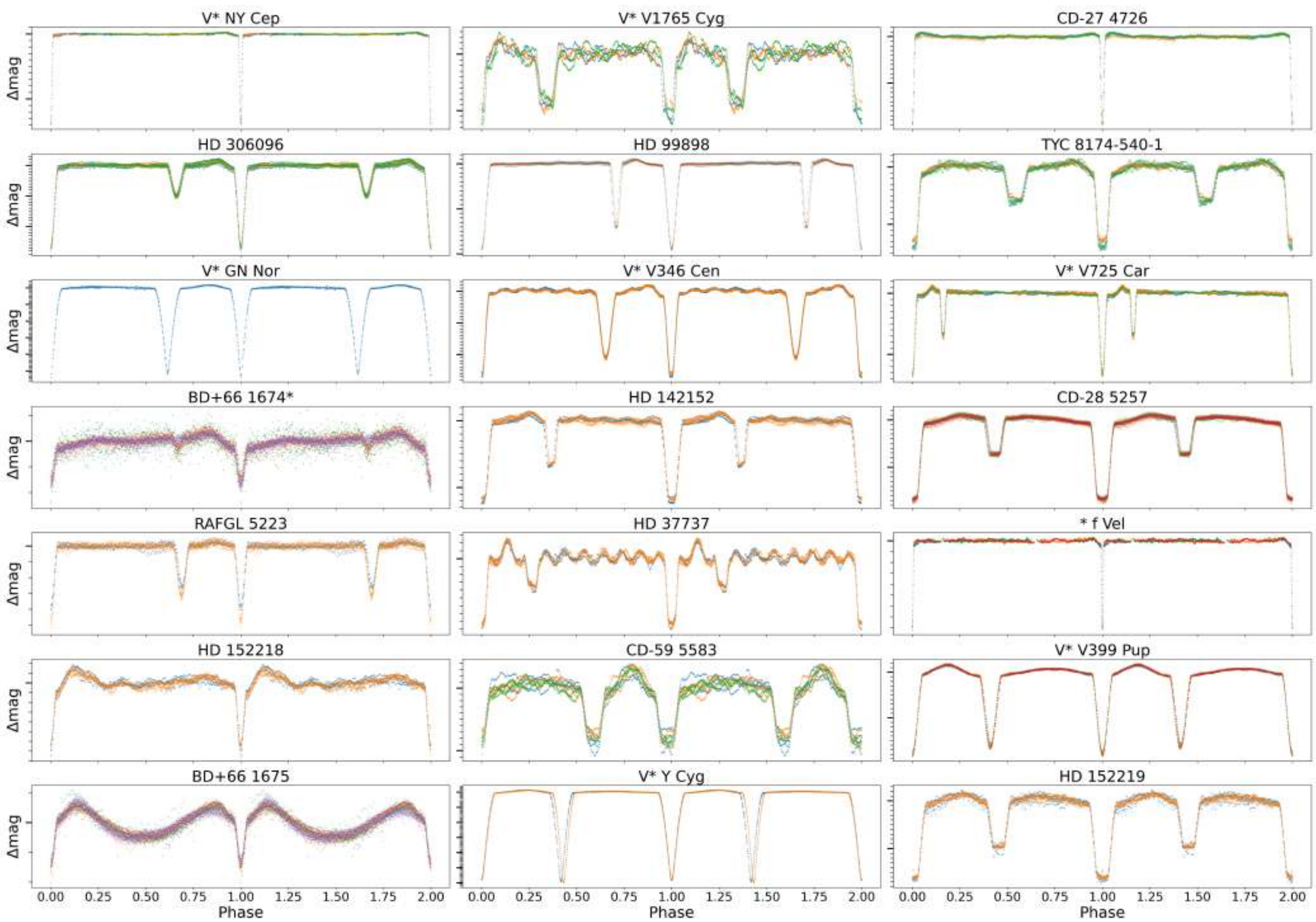

Figure C.1.1: Light curves of systems displaying heartbeat-like features. In each subpanel, bold, long ticks on the Y-axis denote increments of $0.1\Delta mag$, and thin, short ticks indicate increments of $0.01\Delta mag$.